UNIVERSITÉ DE MONTRÉAL

ADVANCES IN COMPOSITE RIGHT/LEFT-HANDED TRANSMISSION LINE COMPONENTS, ANTENNAS AND SYSTEMS

VAN HOANG NGUYEN
DÉPARTEMENT DE GÉNIE ELECTRIQUE
ÉCOLE POLYTECHNIQUE DE MONTRÉAL

THÈSE PRÉSENTÉE EN VUE DE L'OBTENTION DU DIPLÔME DE
PHILOSOPHIÆ DOCTOR
(GÉNIE ELECTRIQUE)
JANVIER 2010

UNIVERSITÉ DE MONTRÉAL

ÉCOLE POLYTECHNIQUE DE MONTRÉAL

Cette thèse intitulée :

ADVANCES IN COMPOSITE RIGHT/LEFT-HANDED TRANSMISSION LINE COMPONENTS, ANTENNAS AND SYSTEMS

présentée par : M. NGUYEN Van Hoang.
en vue de l'obtention du diplôme de : Philosophiæ Doctor
a été dûment acceptée par le jury constitué de :

M. LAURIN Jean-Jacques, Ph.D., président.
M. CALOZ Christophe, Ph.D., membre et directeur de recherche.
M. AKYEL Cevdet, D.Sc.A., membre.
M. DESLANDES Dominic, Ph.D., membre externe.

In memory of my father.

Acknowledgments

First and foremost, I would like to truly thank my advisor, Dr. Christophe Caloz, for his guidance, advice and encouragement throughout this work. Thanks to his visionary leadership and consistency that create an excellent research environment.

I would like to thank my colleagues of the Caloz's EM Theory and Applications Research Group for their help and scientific contributions. A special thank goes to Mr. Samer Abielmona, my lifelong friend and colleague, for always being available, for all the endless technical discussions, and for proofreading of this thesis and most of the papers I have written in this work. I also thank all of the group's international collaborators who have contributed in a number of ways to my work.

I would also like to acknowledge the members of my thesis jury, Prof. Jean-Jacques Laurin, Prof. Cevdet Akyel, and Prof. Dominic Deslandes from UQÀM, for having accepted to examine this work and for their valuable comments.

Many components and systems which I designed would not have been realized without the assistance of all technical staffs at the Poly-Grames Research Centre. I want to thank Mr. Jules Gauthier, Mr. Steve Dubé, Mr. Traian Antonescu and Mr. Roch Brassard who is no longer at our centre but had helped in realizing many of the first devices. I am grateful to Mr. Jean-Sébastien Décarie for troubleshooting of all computer problems and to Mrs. Louise Clément, Mrs. Nathalie Lévesque, and Mrs. Ginette Desparois for all of the administrative matters. I also appreciate the help of many friends and colleagues at our research centre.

I take a line here to thank the Fonds de recherche sur la nature et les technologies du Quebec for the Doctoral research scholarship and the Natural Sciences and Engineering Research Council of Canada for the financial assistance of various projects performed in this work.

And last but not least, I own my deepest gratitude to my family, to Ánh Ngọc and Hoàng Sam for their patience, understanding and support during this long journey.

Résumé

Les Métamatériaux (MTMs) électromagnétiques sont des matériaux artificiels qui présentent des propriétés remarquables non disponibles dans les substances naturelles. De récents travaux de recherche et de développement ont permis de démontrer des applications optiques et micro-ondes des MTMs, telles que des lentilles à super-résolution, des dispositifs d'invisibilité, de nouveaux filtres passe-bande, des coupleurs améliorés, des résonateurs et des antennes à ondes de fuite avec de nouvelles propriétés et performances. Avec la capacité à manipuler les ondes électromagnétiques se propageant par l'intermédiaire de leur support, les MTMs électromagnétiques pourraient devenir une clé importante des dispositifs et systèmes optiques, et micro-ondes de l'avenir.

Cette thèse présente les dernières avancées des MTMs micro-ondes basés sur le concept des Lignes de Transmission Composites à Main Gauche/Droite (Composite Right/Left-Handed Transmission Line - CRLH TL). Les CRLH TLs sont des structures non-résonantes, constituées de la répétition périodique de série de condensateurs et d'inductances shunt très petits par rapport à la longueur d'onde guidée, qui ont une large bande et de faibles pertes pour les applications micro-ondes. De plus, les CRLH TLs planaires permettent une fabrication à faibles coûts en utilisant la technologie des circuits imprimés et un niveau élevé d'intégration avec les autres composants et systèmes.

Ce travail constitue une contribution au développement de nouveaux composants, antennes et systèmes CRLH TL dans trois des classes d'applications spécifiques : onde guidée en régime harmonique, onde guidée en régime d'impulsionnel et onde rayonnée. Dans la première classe, un filtre passe-bande à large bande, un diviseur de puissance en série et des coupleurs à lignes couplées sont élaborés et vérifiés expérimentalement. La deuxième classe comprend un différentiateur et un émetteur à modulation par position d'impulsion. Dans la troisième classe, deux nouveaux concepts de recyclage de puissance améliorant systématiquement l'efficacité de rayonnement des antennes à ondes de fuite (Leaky-Wave Antenna - LWA) sont présentés, numériquement vérifiés par simulation électomagnétique et démontrés expérimentalement.

Application de l'onde guidée en régime harmonique

Le condensateur interdigital, généralement utilisé dans CRLH TLs, souffre d'une résonance transversale aux fréquences élevées à cause des courants en boucle formés entre ses doigts entrelacés. Cette résonance limite la bande passante des CRLH TLs. Pour cette raison, une nouvelle architecture de la CRLH TL basée sur le concept Métal-Isolant-Métal (MIM) a été proposée, caractérisée, démontrant sa capacité à supprimer complètement cette résonance transversale. La topologie MIM a les avantages d'être symétrique et de petite taille, tout en permettant d'exploiter pleinement la bande passante de la structure. Basé sur cette nouvelle architecture, un filtre passe-bande avec des résonateurs couplés à résonances progressives a été conçu, et sa bande passante ultra-large confirme son bon fonctionnement. De plus, un diviseur de puissance sériel à longueur d'onde infinie utilisant la même architecture MIM basée sur le concept du CRLH en configuration "stripline" a été proposé et fabriqué. Ce diviseur de puissance en série a un réseau d'adaptation accordable à l'entrée et supporte un nombre arbitraire de ports de sortie.

Les coupleurs à lignes MTMs couplées ont démontré un niveau de couplage extraordinaire comparé à celui des coupleurs conventionnels à lignes couplées. Cependant, l'analyse des modes pair et impair qui a été utilisée pour analyser les coupleurs formés par les lignes conventionnelles et/ou MTMs ne fournit qu'un aperçu incomplet du mécanisme de couplage. Pour y remédier, la théorie de modes couplés a été appliquée au coupleur composé avec la technologie MIM basés sur les CRLH TLs fournissant ainsi une explication phénoménologique du comportement complexe du couplage des coupleurs MTMs. Cette théorie a été, par après, simplifié au cas de l'onde quasi-TEM afin de fournir une compréhension apprefondie du mécanisme de couplage. Il importe de mentionner que l'équation de couplage dérivée indique un net avantage pour les coupleurs MTMs dont le couplage dépend de leur longueur de couplage. Trois exemples correspondants à trois différents types de topologies de coupleurs ont été démontrés et la théorie développée prédit fidèlement leur niveau de couplage et leur gamme de fréquences.

Application de l'onde guidée en régime d'impulsion

L'étude de la théorie des modes couplés dans le domaine du temps révèle une intéressante relation entre les ports d'entrée et couplé du coupleur à lignes couplées

conventionnelles dans le régime d'impulsion. Le coupleur à lignes couplées conventionnelles peut être considéré comme un cas particulier du coupleur à lignes couplées basée sur la CRLH TL où les éléments gauches sont infinis. Il est montré que la dérivée temporelle de premier ordre d'un signal impulsion d'une durée ΔT peut être obtenue exactement au port couplé d'un coupleur opérant à fréquence centrale f_0 et satisfaisant la condition $4\Delta T f_0 \gg 1$. Étant symétrique et un dispositif à quatre ports, le coupleur à lignes couplées peut simultanément fournir le couplage entre deux paires de ports d'entrée/couplé. Combiné avec une ligne à retard appropriée, ces propriétés mènent à un circuit dérivé de premier et second ordre employant seulement un coupleur à lignes couplées. Un coupleur a été fabriqué avec la technologie des circuits imprimés multicouches démontrant le principe d'opération et la faisabilité de ce concept pour des signaux à régime d'impulsion arbitraires.

Étant une ligne de transmission planaire ayant une propriété dispersive au sein de sa bande passante, la CRLH TL est appropriée aux applications à régime d'impulsion telles que les lignes à retard d'impulsion accordable. Basé sur ce concept, un nouvel émetteur à modulation par position d'impulsion a été conçu pour démontrer le principe et testé pour des systèmes de modulation binaire et quaternaire dans un lien sans-fil réel. Des efforts supplémentaires conduiraient à une ligne dispersive de taille plus petite avec un plus grand retard afin de satisfaire aux systèmes de modulation d'ordre supérieur.

Application de l'onde rayonnée

Il est bien connu que la structure CRLH TL ouverte supporte une onde rapide et peut donc opérer comme une antenne à ondes de fuite - LWA. Lorsqu' imprimée sur un substrat planaire commercial, la CRLH TL LWA fournit un balayage fréquentiel d'un faisceau directif couvrant l'espace entier, mais souffre d'une faible efficacité de rayonnement due à sa longueur restrainte. Pour remédier à ce problème, deux nouveaux concepts de recyclage de puissance ont été proposés afin d'améliorer de façon significative le rendement du rayonnement de l'antenne LWA et son antenne réseau 2D. Le premier concept, le *recyclage-croisé*, qui est approprié pour les antennes réseaux LWA 2D, recycle la puissance non rayonnée entre les éléments du réseau jusqu'à ce que la puissance ait presque toute été écoulée. Par conséquent, cela augmente effectivement la puissance rayonnée totale pour une puissance d'entrée donnée. De plus, il est démontré qu'en augmentant le nombre d'éléments du réseau la directivité et l'efficacité

du rayonnement de l'antenne réseau LWA 2D à recyclage-croisé sont améliorées. Le résultat mesuré de l'antenne réseau LWA 2D à cinq éléments donne une amélioration de 160% du niveau d'efficacité du rayonnement.

Contrairement au recyclage-croisé, le deuxième concept nommé *l'auto-recyclage* est appliqué qu'à une seule antenne LWA où la puissance non rayonnée à la fin de l'antenne est recyclée vers son port d'entrée via un réseau de rétroaction. Pour un design idéal sans pertes diélectriques, ohmiques et de désadaptation, l'auto-recyclage maximise la puissance totale rayonnée au même niveau que la puissance d'entrée ; ce qui veut dire une efficacité de rayonnement de 100%. Avec l'ajout d'un coupleur "rat-race", l'antenne LWA à auto-recyclage a été conçue et fabriquée sur un substrat commercial ayant une épaisseur et des pertes diélectriques déterminées. L'efficacité mesurée du rayonnement passe de 38% pour une simple antenne LWA à 68,45% pour une antenne LWA avec le système d'auto-recyclage. Ces résultats prometteurs donnent un net avantage à l'antenne LWA à deux ports sur les antennes de type résonant en termes de directivité et d'efficacité de rayonnement.

Abstract

Electromagnetic metamaterials (MTMs) are engineered artificial materials that exhibit unusual properties not available in natural materials. Recent research and development have shown promising optical and microwave applications of MTMs such as super-resolution lenses, cloaking devices, bandpass filter, enhanced couplers, resonators, and leaky-wave antennas with new properties and performance, to name a few. With the ability to manipulate electromagnetic waves propagating through its medium, electromagnetic MTMs are believed to hold an important key to many future optical and microwave devices and systems.

This dissertation presents the most recent advances in microwave MTMs based on the Composite Right/Left-Handed (CRLH) transmission line (TL) concept. The CRLH TL based MTMs are non-resonant structures which are constituted of periodic repetition of series capacitors and shunt inductors with a unit cell's size much smaller than the guided wavelength and have favorable broadband and low-loss properties for microwave applications. In addition, planar CRLH TL-based MTMs permit a low-cost fabrication using printed circuit board (PCB) technology and a high level of integration with other microwave components and systems.

This work contributes to the development of novel CRLH TL components, antennas and systems in three specific classes of application: harmonic regime guided-wave, impulse regime guided-wave and radiated-wave. In the first class, a wideband bandpass filter, an infinite wavelength series power divider and enhanced coupled-line coupler are developed and verified experimentally. The second class consists of a time differentiator component and a pulse position modulation transmitter system. In the third class, two novel power-recycling concepts to systematically enhance the radiation efficiency of Leaky-Wave Antennas (LWAs) are presented, verified numerically using electromagnetic simulation and demonstrated experimentally.

Harmonic regime guided-wave application

The interdigital capacitor, generally utilized in CRLH TLs, suffers a transverse resonance at high frequencies due to loop currents forming between adjacent interdigitated fingers. This resonance limits the operating bandwidth of CRLH TL based

MTMs. For this reason, an alternative CRLH TL architecture based on Metal-Insulator-Metal (MIM) capacitors was proposed, characterized, and demonstrated to completely suppress the transverse resonance. The MIM based CRLH TL topology has advantages of symmetric design and small size while allows full operating bandwidth. Based on the new architecture, a bandpass filter with tapered coupled resonators was designed and the achieved ultra-wide bandwidth confirms its operation. In addition, an infinite wavelength series power divider using the same MIM based CRLH TL architecture in a stripline configuration was proposed and fabricated. This series power divider has a tunable input matching network and supports an arbitrary number of output ports.

Metamaterial-based coupled-line couplers were shown to exhibit an extraordinary coupling level compared with conventional coupled-line couplers. However, the even/odd-mode analysis which was used to analyze MTM couplers provides little insight into the coupling mechanism. To this end, the coupled-mode theory is extended and applied to couplers consisting of the general CRLH TLs to provide a phenomenological explanation of the complex coupling behavior. The theory was simplified for a quasi transverse electromagnetic (quasi-TEM) case to provide further insight into the coupling mechanism. Importantly, the coupling equation indicates a distinct advantage of CRLH TL couplers, which have a maximum coupling depending on its coupling length. Three examples corresponding to three different coupling topologies were demonstrated and the developed theory accurately predicts the coupling level and coupling frequency range.

Impulse regime guided-wave application

The study of coupled-mode theory in the time domain reveals an interesting derivative relation between input and coupled ports of conventional coupled-line couplers operating under an impulse regime. The conventional coupled-line couplers can be considered as a special case of CRLH TL coupled-line couplers where the left-handed elements are infinite. It is shown that a first-order time derivation of an impulse signal of duration ΔT can be accurately obtained at the coupled port of a coupler operating at a center frequency f_0 and satisfying the condition $4\Delta T f_0 \gg 1$. As a symmetric, four-port device, a coupled-line coupler can simultaneously provide coupling between two pairs of input/coupled ports. Combining with a proper time delay circuit, these properties lead to a first- and second-order time derivative circuit

using only a single coupled-line coupler. A broadside coupler is fabricated in a multi-layer PCB technology, which shows the operating principle and the feasibility of this concept for other arbitrary impulse regime signals.

As planar TLs have a dispersive property within their operating bandwidth, CRLH TLs were found suitable for impulse regime application such as delay lines with a tunable time delay. Built upon this concept, a new pulse position modulator (PPM) transmitter was designed as a proof-of-principle and tested for both binary and quaternary modulation schemes in an actual wireless link. CRLH TLs having smaller size and a larger delay can be potentially realized which lead to a PPM transmitter with higher-order modulation schemes.

Radiated-wave application

It is well known that open CRLH TL structures support a fast-wave and therefore can operate as a leaky-wave antenna (LWA). Being conveniently printed on planar commercial substrate, CRLH TL LWAs provide a frequency-scanning directive beam in full space but suffer from a low radiation efficiency due to its finite lengths. For this reason, two novel *power-recycling* concepts were proposed to significantly enhance the radiation efficiency of LWA and its 2D array. The first *cross-recycling* concept which is suitable for 2D LWA arrays, recycles the non-radiated power between array elements until most of the input power has leaked out. Therefore, it effectively increases the total radiated power for a given input power. In addition, it is shown that an increasing in the number of array elements directly enhances both directivity and radiation efficiency of the cross-recycling 2D LWA array. The measured result of a 2D LWA array of 5 elements indicates an increase of 160% in radiation efficiency.

In contrast to the cross-recycling, the second *self-recycling* concept is applied to a single LWA where non-radiated power at the end of the LWA is recycled back into its input via a feedback network. For an ideal design having no dielectric, ohmic and mismatch losses, the self-recycling concept maximizes the total radiated power to the level of the input power; hereby yields a 100% radiation efficiency. A rat-race based, self-recycling LWA was designed and fabricated on a commercial substrate with a finite copper thickness and dielectric loss. The measured radiation efficiency increases from 38% for a single LWA to 68.45% for the self-recycling LWA. These promising results give any two-port LWA clear advantages over resonant-type antennas in terms of directivity and radiation efficiency.

Condensé en Français

Depuis le travail précurseur de Veselago en 1967 [1] et la démonstration réussie des métamatériaux dans le régime des micro-ondes par Smith et ses collègues en 2000 [2], la recherche et le développement sur les métamatériaux ont suscité un intérêt scientifique important au cours de la dernière décennie. Dans ce domaine, des progrès significatifs ont été réalisés dans presque tous les aspects de la recherche, allant des techniques numériques aux applications pratiques micro-ondes, terahertz et optiques [3], [4], [5], [6], [7].

Ce travail constitute une contribution au développement de nouvelles applications micro-ondes des métamateriaux et est présenté sous la forme d'articles de recherche académiques. La Ligne de Transmission (LT) Composite à Main Gauche/Droite (Composite Right/Left-Handed – CRLH TL), qui est une réalisation planaire et non-résonante des métamatériaux, est principalement utilisée dans la plupart des composants, antennes et systèmes développés dans ce travail. Ces composants, antennes et systèmes sont classés selon trois différentes classes d'applications: 1) application onde guidée en régime harmonique, 2) application onde guidée en régime impulsionnel, et 3) application onde rayonnée.

La classe onde guidée en régime harmonique est présentée au chapitre 3 avec trois exemples représentatifs: un filtre passe-bande à large bande, un diviseur de puissance en série à longueur d'onde infinie, et des coupleurs améliorés à lignes couplées. Tous ces exemples utilisent une architecture CRLH TL avec condensateur en configuration Métal-Isolateur-Métal (MIM), qui est exempt de résonances transverses et qui présente une large bande passante, ainsi qu'une cellule unitaire compacte et symétrique. Un résumé de la contribution et du principe de fonctionnement de chacun des exemples est donné aux articles 1, 2 et 3.

La classe onde guidée en régime impulsionnel est présentée au chapitre 4 où deux exemples choisis sont le différentiateur d'impulsion et l'émetteur à modulation par position d'impulsion. Contrairement aux applications en régime harmonique, où les composants sont alimentés par une source sinusoïdale, les éléments en régime d'impulsion sont excités par des sources générant des fonctions en échelon ou gaussiennes, par exemple. Un résumé de ces deux composants est fourni aux articles 4 et

5.

Les antennes à ondes de fuite sont l'application principale de la classe onde rayonnée dans ce travail. C'est le sujet du chapitre 5. Deux nouveaux exemples de recyclage de puissance d'antenne à ondes de fuite sont introduits et permettent d'améliorer de manière significative l'efficacité de rayonnement de l'antenne jusqu'à 100%. Les articles 6 et 7 couvrent l'opération de recyclage de puissance des antennes à ondes de fuite.

Article 1 : Filtre Passe-bande Hautement Sélectif à Large Bande Basé sur la Structure CRLH avec Résonateurs Couplés Progressifs (Broadband Highly Selective Bandpass Filter based on Tapered Coupled-Resonator CRLH Structure)

Puisque la structure CRLH TL est une ligne de transmission artificielle réalisée en juxtaposant un nombre fini de cellules unitaires composées d'inducteurs et de condensateurs, elle présente une structure de bande passante et bande interdite, propriété fondamentale des structures périodiques. Par conséquent, la structure CRLH TL peut être employée dans la conception de filtres passe-bande et coupe-bande. Cependant, cette structure lorsque réalisée avec des condensateurs planaires interdigitaux, possède plusieurs résonances transverses (non désirées) au sein de sa bande passante opérationnelle, rendant le filtre impropre aux applications large bande.

Dans ce travail, une structure CRLH alternative réalisée avec la configuration MIM est proposée et appliquée comme élément central du design d'un filtre passe-bande hautement sélectif. La structure CRLH employant la configuration MIM offre un design très compact et symétrique et permet d'éviter complètement les résonances transverses (non désirées). Cette structure a une coupure très nette à la bande coupée inférieure, conséquence directe de la réponse de plus en plus forte de l'onde lente de la structure CRLH dans la bande main gauche près des basses fréquences. Par contre, la bande coupée supérieure n'a pas la même caractéristique de coupure. Pour remédier à ce problème, le filtre passe-bande sélectif est réalisé en ajoutant à chaque cellule unitaire de la structure CRLH TL un résonateur couplé ayant une fréquence de résonance dans la bande interdite supérieure. Néanmoins, lorsqu'il est couplé à la structure CRLH TL, le résonateur crée un zéro de transmission ainsi qu'un pôle de transmission indésirable. Afin de supprimer ce pôle de transmission, les fréquences de résonance des résonateurs couplés sont conçues de manière à former une distribution progressive des pôles d'atténuation annulant les pôles d'atténuation correspondants

de manière itérative.

Le très sélectif Tapered Coupled-Resonator (TRC) CRLH BPF est fabriqué en technologie multicouche de circuits imprimés et présente une bande passante fractionnaire mesurée supérieure à 100%. La comparaison avec le filtre conventionnel à ondulations égales de même taille, ordre et substrat et ayant les mêmes pertes d'insertion montre qu'une bande 70% plus large est obtenue avec la structure TRC CRLH BPF.

Article 2 : Diviseur de Puissance Sériel Accordable à N-ports Arbitraires (Tunable Arbitrary N-port CRLH Series Power Divider)

Ce travail présente un diviseur de puissance CRLH TL utilisant la même architecture MIM basée sur le concept CRLH que proposée dans le précédent travail. Le diviseur de puissance sériel opère à la fréquence de transition ω_0 de la ligne de transmission CRLH en régime à longueur d'onde infinie. Dans ce régime, tous les ports de sortie du diviseur sont en parfait équilibre de phase et d'amplitude, indépendamment du nombre de ports de sortie, étant donné que la longueur électrique entre les différents ports est exactement zéro. En plus, un réseau d'adaptation accordable utilisant une capacité variable est ajouté au diviseur de puissance afin de supporter un nombre arbitraire de ports de sortie. Pour éviter tout risque de fuite par rayonnement, le diviseur de puissance a été fabriqué dans une configuration "stripline". Les résultats mesurés permettent de valider son principe fonctionnement.

Article 3 : Approche Généralisée de Modes Couplés des Coupleurs Métamatériaux (MTMs) à Lignes Couplées : Théorie de Couplage, Explication Phénoménologique et Démonstration Expérimentale (Generalized Coupled-Mode Approach of Metamaterial Coupled-Line Couplers: Coupling Theory, Phenomenological Explanation and Experimental Demonstration)

Cet article présente l'étude théorique, l'explication phénoménologique du couplage et la démonstration expérimentale de l'approche du mode couplé des coupleurs MTMs à lignes couplées. Cette approche est une extension de la théorie traditionnelle du mode couplé pour le cas de types arbitraires de coupleurs conventionnels ou MTMs avec des lignes représentées par le modèle le plus général de la CRLH TL.

La démarche proposée est totalement rigoureuse et s'applique à tous les types de coupleur: symétrique, asymétrique, conventionnel ou CRLH.

La théorie du mode couplé généralisée est dérivée de façon complète et les résultats analytiques pour les constantes complexes de propagation et les paramètres de diffusion sont fournis. Les formules simplifiées basées sur l'approximation quasi-TEM (exacte lorsque la structure est parfaitement TEM) sont dérivées pour les coupleurs contra-directionnels, qui sont les types les plus communs en micro-ondes. La phénoménologie des coupleurs à lignes couplées à la fois symétrique CRLH - CRLH et asymétrique microruban - CRLH est complètement expliquée, et ce pour la première fois, par l'approche proposée. De la théorie du mode couplé, il est établi que les constantes de propagation des coupleurs CRLH symétrique et asymétrique sont complexes, menant à un niveau de couplage élevé dépendant uniquement de leur longueur de couplage. Les prédictions théoriques et les explications phénoménologiques sont validées par la démonstration expérimentale, accompagnée par une simulation idéale du circuit pour les trois exemples suivants: 1) un coupleur symétrique classique à lignes microrubans, 2) un coupleur symétrique à lignes CRLH, et 3) un coupleur asymétrique à lignes conventionnelle microruban et CRLH.

Article 4 Différentiateurs de Premier et Second Ordres Basés sur les Coupleurs Directionnels à Lignes Couplées (First- and Second-Order Differentiators Based on Coupled-line Directional Couplers)

Dans ce travail, les différentiateurs de premier et deuxième ordres basés sur les coupleurs à lignes couplées sont présentés. L'effet dérivatif du temps des coupleurs à lignes couplées est exposé théoriquement en appliquant les lois de Kirchhoff aux sections TL infinitésimales couplées électromagnétiquement. Les couplages électrique et magnétique entre chacune des sections TL sont modélisés par une capacitance C_e et une inductance L_m, respectivement. Selon la condition $\Delta T f_0 \gg 1/4$, où ΔT est la largeur de l'impulsion d'entrée et f_0 est la fréquence centrale du coupleur, une forme analytique de l'expression de la tension au port couplé est fournie en termes de fonction dérivée du temps de la tension au port d'entrée et des éléments du couplage électromagnétique. Ainsi, la fréquence de fonctionnement est inversement proportionnelle à la durée de l'impulsion.

Comme les coupleurs à lignes couplées sont des dispositifs symétriques et à quatre ports, le couplage se produit entre les deux paires des ports d'entrée/couplé. En

conséquence, la dérivation de second ordre peut être obtenue en réinjectant le signal dérivé de premier ordre de la première paire des ports d'entrée/couplé dans la deuxième paire des ports d'entrée/couplé du même coupleur à lignes couplées. Pour éviter le chevauchement du signal d'entrée avec celui dérivé de second ordre, une ligne à retard est ajoutée entre le premier port couplé et le second port d'entrée. Dans ce travail, le coupleur utilise deux lignes microrubans conventionnelles dans une configuration "broadside" afin d'obtenir une directivité élevée, requise pour la dérivation de deuxième ordre. Les coupleurs auraient pu être implémentés en technologie CRLH pour une plus grande réduction de la taille et pour la possible application du contrôle de la forme de l'impulsion. Le coupleur est fabriqué en technologie multicouche des circuits imprimés et utilisé afin de démontrer expérimentalement le concept de la dérivée de premier et de second ordre. Les résultats mesurés concordent avec ceux obtenus à partir des dérivateurs idéaux (mathématiques).

Article 5 Ligne CRLH à retard Émettrice à Modulation par Position d'Impulsion (CRLH Delay Line Pulse Position Modulation (PPM) Transmitter)

Ce travail présente un émetteur PPM basé sur la ligne CRLH à retard. Cet émetteur, qui contient un générateur d'impulsions, un mélangeur, un oscillateur contrôlé en tension, une ligne de transmission CRLH et une antenne émettrice à large bande, fournit différentes fonctionalités. Le retard accordable des impulsions modulées est réalisé à partir de la propriété de dispersion de la ligne CRLH avec différentes fréquences porteuses de modulation. Ainsi, les symboles d'information peuvent être "codés" en assignant chaque symbole à une seule fréquence correspondante à un retard unique. Les avantages de l'émetteur PPM proposé sont son simple design, son retard d'impulsion continuement accordable et sa capacité d'ordre multiple du PPM.

Deux ensembles de lignes de transmissions CRLH basées sur le concept MIM, chacun composés de trente cellules unitaires, ont été fabriqués en technologie multicouche de circuits imprimés et employés comme lignes à retard de l'émetteur PPM. Pour simplifier, l'oscillateur contrôlé en tension est remplacé par des générateurs de signaux qui génèrent les fréquences correspondantes pour les symboles d'information. L'émetteur est évalué dans un réel lien sans fil où l'antenne réceptrice est directement reliée à l'oscilloscope à échantillonnage numérique, qui permet la visualisation des symboles d'information reçus.

Article 6 Antenne Réseau à Ondes de Fuite 2D à Efficacité Élevée employant un Réseau d'Alimentation en Série Recyclant la Puissance (Highly Efficient Leaky-Wave Antenna Array using a Power-Recycling Series Feeding Network)

Ce travail introduit un nouveau système de recyclage-croisé visant à améliorer la faible efficacité de rayonnement des antennes réseaux LWA 2D. Dans ce système, la puissance non rayonnée au bout de l'élément du réseau est recyclée vers l'élément voisin via un réseau d'alimentation en série jusqu'à ce que la plupart de la puissance d'entrée de l'antenne réseau LWA ait été rayonnée avant les charges de terminaison. Par conséquent le réseau LWA à recyclage-croisé a plus de puissance rayonnée pour la même puissance d'entrée. Ce réseau atteint donc une efficacité de rayonnement et de gain plus grande tout en conservant une longueur raisonnable dans la direction de propagation de l'onde.

L'efficacité dérivée du réseau LWA à recyclage-croisé dépend du produit du nombre d'éléments du réseau et de la longueur de chaque élément LWA. Par comparaison avec les antennes réseaux classiques, le réseau LWA à recyclage-croisé proposé fournit une variable de design additionnelle permettant d'optimiser la directivité et l'efficacité de rayonnement indépendamment. De plus, étant donné que la directivité et l'efficacité de rayonnement augmentent simultanément avec le nombre d'éléments du réseau, le gain du réseau LWA à recyclage-croisé augmente à un taux plus rapide que dans les réseaux conventionnels.

Une antenne réseau LWA à cinq éléments a été fabriquée et mesurée afin de valider le concept proposé. L'efficacité mesurée du réseau LWA à recyclage-croisé est de 60%. Ceci représente une hausse de 160% par rapport au même réseau LWA n'utilisant pas le réseau d'alimentation en série à recyclage-croisé.

Article 7 Système Rétroactif Recyclant la Puissance pour la Maximisation de l'Efficacité de Rayonnement des Antennes à Ondes de Fuite (Power-Recycling Feedback System for Maximization of Leaky-Wave Antennas Radiation Efficiency)

Ce travail propose un nouveau système rétroactif auto-recycleur servant à l'optimisation systématique de l'efficacité de rayonnement des antennes LWA. Dans ce système, la puissance non rayonnée après l'antenne est recyclée vers son port d'entrée via un système combinant de façon constructive les puissances d'entrée et recyclée tout en

assurant l'adaptation et l'isolement de ces deux signaux. Par conséquent, l'efficacité de rayonnement de l'antenne LWA isolée (sans la boucle), η_0, est améliorée par le facteur du système G_s ($G_s > 1$) à une efficacité globale de rayonnement de $\eta_s = G_s\eta_0$, qui peut atteindre 100% pour n'importe quelle valeur de η_0 dans un système sans pertes. Le design du système recyclant la puissance dépend de η_0, qui est généralement le résultat d'un compromis nécessaire entre la directivité et la taille restreinte.

Un coupleur "rat-race" est utilisé comme circuit combinant la puissance dans le système rétroactif LWA proposé. Par comparaison avec d'autres circuits à trois ports (combinateur de puissance de Wilkinson, T-magique) et à quatre ports (coupleur conique à lignes couplées), le coupleur "rat-race" présente des avantages en termes d'implémentation planaire, de rapport de division de puissance arbitraire et d'adaptation de tous les ports. Les équations exactes de design, qui déterminent à la fois les rapports d'impédance du coupleur "rat-race" et les conditions rétroactives de la phase du système pour une antenne LWA arbitraire, sont développées en utilisant l'analyse des paramètres de répartition. La passage de l'état transitoire à l'état permanent est demonstré par un simple modèle mathématique, suivi de simulations transitoires du circuit et électromagnétiques.

Une antenne isolée LWA de 3 dB et le système d'auto-recyclage de puissance de 3 dB ont été fabriqués sur un substrat commercial, incluant naturellement les pertes ohmiques et diélectriques, en plus d'autres imperfections. La mesure de l'efficacité de rayonnement de l'antenne LWA isolée est augmentée de $\eta_0 = 38\%$ à $\eta_s = 68\%$, correspondant à une amélioration de l'efficacité du système de $G_s = 1.8$. Le système proposé à auto-recyclage de puissance s'applique à toutes les antennes LWA et résout leur problème fondamental d'efficacité dans les applications impliquant un compromis entre la directivité relativement élevée et la petite taille requise.

Contents

List of Tables

List of Figures

List of Appendices

List of Abbreviations and Notations

Abbreviations

1D:	One-dimensional
2D:	Two-dimensional
3D:	Three-dimensional
BPF:	Bandpass Filter
BPSK:	Binary Phase Shift Keying
BW:	Bandwidth
CMT:	Coupled-Mode Theory
CR:	Coupled-Resonator
CRLH:	Composite Right/Left-Handed
EM:	Electromagnetics
FBW:	Fractional Bandwidth
HPBW:	Half Power Beam Width
LH:	Left-Handed
LWA:	Leaky-wave Antenna
MoM:	Method of Moments
MTM:	Metamaterial
PCB:	Printed Circuit Board
PPM:	Pulse Position Modulation
QPSK:	Quadrature Phase Shift Keying
TCR:	Tapered Coupled-Resonator
TD:	Time Delayer
TEM:	Transverse Electromagnetic
TL:	Transmission Line
RH:	Right-Handed
UC:	Unit cell
UWB:	Ultra Wideband

Notations

c:	speed of light in vacuum $3 \cdot 10^8$m/s
ε_0:	permittivity of free space
μ_0:	permeability of free space
k_0:	free space wave number
λ:	wavelength
β:	propagation constant
$\vec{E}$:	electric field intensity
$\vec{D}$:	electric flux density
$\vec{H}$:	magnetic field intensity
$\vec{B}$:	magnetic flux density
Z_B:	Bloch impedance

Chapter 1

Composite Right/Left-Handed (CRLH) Transmission Line (TL) Metamaterials (MTMs)

1.1 Introduction

Electromagnetic (EM) metamaterials (MTMs) are a class of effectively homogenous structures exhibiting unusual properties not readily available in natural materials. EM MTMs are therefore artificial, engineered structures, generally composed of periodically arranged sub-wavelength inductive and capacitive elements in 1D, 2D, or 3D configuration. The size of a unit cell (UC) containing these elements is much smaller than the operating wavelength (λ_g), i.e. $p \ll \lambda_g$, and therefore EM MTMs operate in the long-wavelength regime.

The first microwave MTM was demonstrated by Smith *et al.* in 2000 [2] using thin-wires and split-ring resonators to synthesize a medium with simultaneously effective negative permittivity ε and negative permeability μ. Because of the inherent resonant nature of the proposed structure, this first MTM had a narrow bandwidth. In addition, the structure was volumetric, bulky and lossy. Therefore, it is not suitable for microwave applications where most of the components and systems have planar implementations.

In 2002, the first planar transmission line (TL) MTMs operating at microwave frequencies were introduced by Caloz and Itoh [9], Iyer and Eleftheriades [10], and Oliner [11]. In contrast to the previous generation MTMs, planar TL MTMs, which are constituted of printed or discrete inductors and capacitors, are *not* resonant. As a result, planar TL MTMs exhibit broad bandwidth, low loss and the capability to be easily integrated with other microwave components and systems. The most general and practical TL MTMs are the composite right/left-handed (CRLH) TL MTMs.

The CRLH TL MTMs and their microwave applications are the main topic of this dissertation. The next section presents basic periodic structure theory used for the analysis of CRLH TL MTMs and summarizes useful formulas and key properties of CRLH TL MTMs used in this work. Most of the material presented in this section are extracted from [4]. Section 1.3 lists the previous guided-wave and radiated-wave applications of CRLH TL MTMs.

1.2 Basic Theory

1.2.1 Periodic Structure Analysis

The most general and practical MTMs for planar microwave applications are the CRLH TL MTMs, which are realized in planar form by periodically printing interdigital capacitors and shorted-stub inductors on conventional substrates, as shown in Fig. 1.1(a). Fig. 1.1(b) shows an equivalent LC circuit model of a symmetrical unit cell of size p. The symmetrical circuit model is essentially composed of series interdigital capacitors ($2C_L$) and a shunt inductor (L_L) formed by a TL shorted to the ground plane. Due to the inherent parasitic nature of a TL circuit at high frequency, a parasitic series inductor ($L_R/2$) and a shunt capacitor (C_R) are associated with the CRLH TL MTM structure.

The propagation constant ($\gamma = \alpha + j\beta$) and the Bloch impedance (Z_B) of the CRLH TL can be analyzed by applying the periodic boundary condition to the unit cell represented by its $[ABCD]$ matrix. For the equivalent LC circuit model of Fig. 1.1(b), this matrix is given as

$$\begin{bmatrix} A & B \\ C & D \end{bmatrix} = \begin{bmatrix} 1 & Z/2 \\ 0 & 1 \end{bmatrix} \begin{bmatrix} 1 & 0 \\ Y & 1 \end{bmatrix} \begin{bmatrix} 1 & Z/2 \\ 0 & 1 \end{bmatrix} = \begin{bmatrix} 1+\frac{ZY}{2} & Z\left(1+\frac{ZY}{4}\right) \\ Y & 1+\frac{ZY}{2} \end{bmatrix}, \quad (1.1)$$

where

$$Z/2 = j\omega L_R/2 + \frac{1}{j\omega 2C_L}, \quad (1.2a)$$

$$Y = j\omega C_R + \frac{1}{jwL_L}. \quad (1.2b)$$

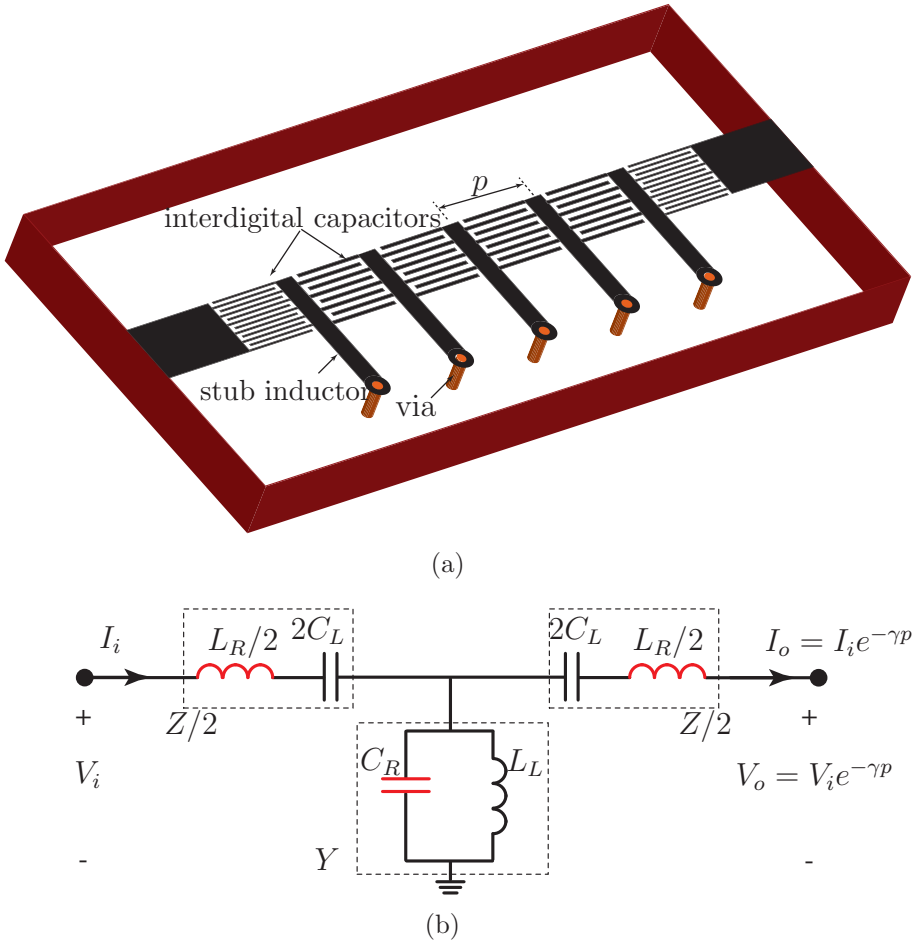

Figure 1.1 a) Planar CRLH TL MTM with interdigital capacitor and shorted stub inductor. b) Equivalent LC circuit model of a UC.

The output current I_o and voltage V_o can be related to the input current I_i and voltage V_i via this $[ABCD]$ matrix

$$\begin{bmatrix} V_o \\ I_o \end{bmatrix} = e^{-\gamma p} \begin{bmatrix} V_i \\ I_i \end{bmatrix} = \begin{bmatrix} A & B \\ C & D \end{bmatrix} \begin{bmatrix} V_i \\ I_i \end{bmatrix}. \tag{1.3}$$

Equation (1.3) can be rearranged to the form of a homogeneous linear system

$$\begin{bmatrix} A - e^{-\gamma p} & B \\ C & D - e^{-\gamma p} \end{bmatrix} \begin{bmatrix} V_i \\ I_i \end{bmatrix} = \begin{bmatrix} 0 \\ 0 \end{bmatrix}, \tag{1.4}$$

which has a nontrivial solution if and only if the determinant is equal to zero, i.e.

$$e^{2\gamma p} - (A + D)e^{\gamma p} + (AD - BC) = 0. \tag{1.5}$$

The $[ABCD]$ matrix given in (1.1) for the symmetrical equivalent LC network circuit of Fig. 1.1(b) has $AD - BC = 1$, hence (1.5) reduces to the following equation after multiplying (1.5) with $e^{-j\gamma p}$

$$\cosh(\gamma p) = 1 + \frac{ZY}{2}. \tag{1.6}$$

In the passband, the CRLH TL structure supports a propagating wave having a phase propagation constant β, which can be related to the LC circuit parameters through the following *dispersion relation* $(\beta - \omega)$

$$\cos(\beta p) = 1 + \frac{ZY}{2}. \tag{1.7}$$

Because the CRLH TL operates in the long-wavelength regime, the UC's size p is much smaller than the guided wavelength λ_g $(p \ll \lambda_g)$. As the result, the left-hand side of (1.7), $\cos(\beta p)$, can be approximated using Taylor expansion to the second order as $\cos(\beta p) \approx 1 - (\beta p)^2/2$. Substituting this relation back into (1.7), one obtains

$$\beta \approx \frac{1}{p}\sqrt{-ZY} = \frac{1}{p}\sqrt{\left(\omega^2 L_R C_R + \frac{1}{\omega^2 L_L C_L}\right) - \left(\frac{L_R}{L_L} + \frac{C_R}{C_L}\right)}. \tag{1.8}$$

When the balanced condition is satisfied, i.e. $L_R C_L = L_L C_R$, (1.8) simplifies to

$$\beta = \frac{1}{p}\sqrt{\frac{\omega^2}{\omega_R^2} + \frac{\omega_L^2}{\omega^2} - 2\frac{\omega_L}{\omega_R}} = \frac{1}{p}\left(\frac{\omega}{\omega_R} - \frac{\omega_L}{\omega}\right), \tag{1.9a}$$

with

$$\omega_R = \frac{1}{\sqrt{L_R C_R}}, \tag{1.9b}$$

$$\omega_L = \frac{1}{\sqrt{L_L C_L}}. \tag{1.9c}$$

The simplified dispersion relation given in (1.9a) can be seen as a superposition of the isolated RH TL contribution $(\frac{1}{p}\omega/\omega_R)$ and that of the isolated LH TL contribution

($\frac{1}{p}\omega_L/\omega$). Fig. 1.2(a) shows the dispersion diagrams of the CRLH TL MTM structure, isolated RH TL, and isolated LH TL.

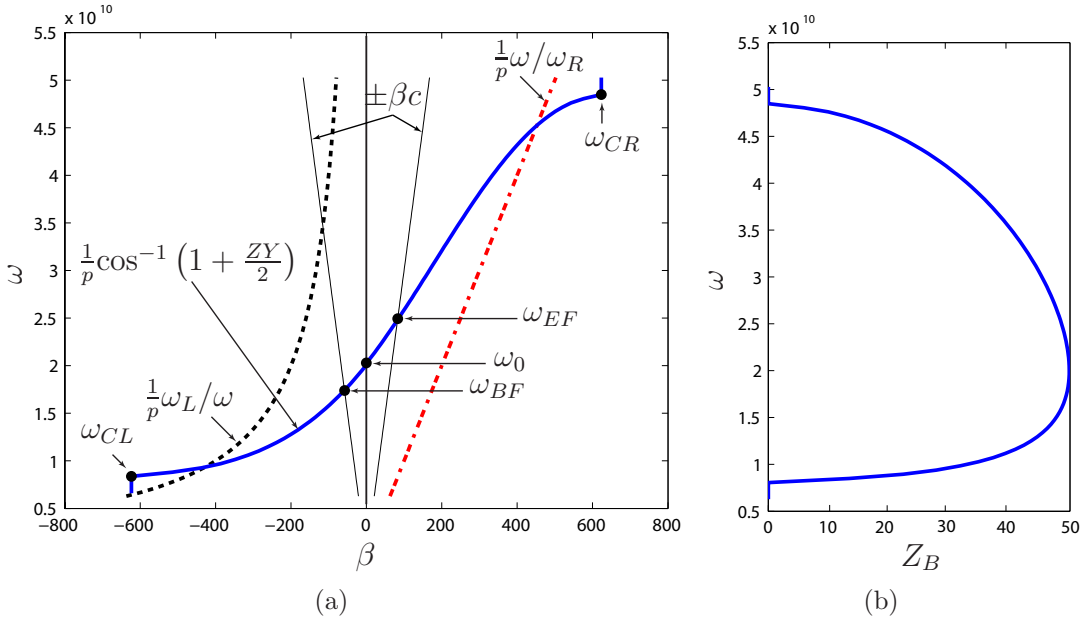

Figure 1.2 a) Dispersion diagram ($\beta-\omega$ diagram), and b) Z_B of a CRLH TL for the following unit cell parameters: $L_R = L_L = 2.5$ nH and $C_R = C_L = 1.0$ pF.

Unlike the conventional uniform RH TL such as microstrip or stripline TLs where the characteristic impedance can be defined at any point along the line, the periodic LC network representation of the CRLH TL does not have a well-defined impedance due to the loading of the network. In such a periodic network, the *Bloch* impedance, Z_B, is used instead, which is defined as the impedance at the terminals of the unit cell at any k-th point of the TL and given as

$$Z_B = \frac{V_k}{I_k} = \frac{V_i}{I_i} = -\frac{B}{A - e^{\gamma p}} \quad (\Omega). \tag{1.10}$$

Solving for $e^{\gamma p}$ in (1.5), the Bloch impedance can be obtained as a function the ZY parameters for the LC network of Fig. 1.1(b)

$$Z_B = \frac{\pm B}{\sqrt{A^2-1}} = \sqrt{\frac{Z}{Y}}\sqrt{1+\frac{ZY}{4}} \quad (\Omega). \tag{1.11}$$

Fig. 1.2(b) illustrates the Bloch impedance in the passband of the CRLH TL structure bounded by the lower LH ω_{CL} and the upper RH ω_{CR} cutoff frequencies.

Outside this range, the Bloch impedance is imaginary and the CRLH TL structure no longer supports a traveling wave.

1.2.2 Properties and Useful Formulas

Figs. 1.2(a) and 1.2(b) reveals useful properties of CRLH TLs which will be exploited in this work. They are infinite-wavelength regime, leaky-wave radiation, filtering, frequency dispersion, and backward-wave propagation. These properties and corresponding formulas are summarized in this section.

Under the balanced condition, the *infinite-wavelength* regime corresponds to the *transition frequency* ω_0 point on the dispersion diagram at $\beta = 0$. This is a unique property of CRLH TLs where the guided wavelength $\lambda_g = 2\pi/|\beta|$ is infinite at a non-zero frequency. This transition frequency can be found by setting (1.9a) to 0 and solve for ω_0

$$\omega_0 = \sqrt{\omega_R \omega_L}. \tag{1.12}$$

Inspecting Fig. 1.2(a) closely reveals that the dispersion curve of the CRLH TL penetrates into the fast-wave region which is delimited by the two lightlines $\omega = -\beta c$ and $\omega = +\beta c$. This indicates that the CRLH TL structure can operate as a *leaky-wave antenna* (LWA) if it is excited by a source with a frequency within this range where $|\beta| \leq k_0$. The radiation angle of the main beam of a CRLH TL LWA is given approximately as

$$\theta(\omega) = \sin^{-1}\left(\frac{\beta}{k_0}\right), \tag{1.13}$$

where θ is measured from the axis perpendicular to the plane of the LWA. Because the radiation angle of the main beam is a function of the applied frequency, frequency scanning is an important property of CRLH TL LWAs. In addition, since the dispersion curve intersects the two lightlines, CRLH TL LWAs provide full-space scanning from back-fire to end-fire including broadside radiations. The lower, back-fire and upper, end-fire frequencies of the leaky-wave radiating range can be obtained by setting

$\beta = \pm k_0$ and solving for ω_{BF} and ω_{EF}, respectively. The results are

$$\omega_{BF} = \frac{\omega_0}{\sqrt{1 + p\omega_R/c}}, \tag{1.14a}$$

$$\omega_{EF} = \frac{\omega_0}{\sqrt{1 - p\omega_R/c}}, \tag{1.14b}$$

where c is the speed of light in vacuum.

As can be observed from Fig. 1.2(b), in the frequency range where the Bloch impedance is real, the CRLH TL structure supports a traveling wave and therefore operates as a *bandpass filter* (BPF). It should be noted that because the Bloch impedance is not constant in the passband, BPF design based on CRLH TL structure is non-optimum in terms of passband insertion loss. However, the useful properties of CRLH TL BPFs are wide bandwidth and sharp rejection in stopbands. The lower and upper cutoff frequencies of the passband can be obtained by setting the Bloch impedance, as given in (1.11), to 0 and solve for ω_{cL} and ω_{cR}. The results are

$$\omega_{CL} = \omega_R \left(\sqrt{1 + \frac{\omega_L}{\omega_R}} - 1 \right), \tag{1.15a}$$

$$\omega_{CR} = \omega_R \left(\sqrt{1 + \frac{\omega_L}{\omega_R}} + 1 \right). \tag{1.15b}$$

Dispersion is another unique property of CRLH TLs which is evident from its dispersion diagram. The group velocity (slope of the dispersion curve) varies with frequency in the passband from ω_{CL} to ω_{CR} and given as

$$v_g = \left(\frac{d\beta}{d\omega} \right)^{-1} = \frac{p\sin(\beta p)}{(\omega/\omega_R^2) - (\omega_L^2/\omega^3)}. \tag{1.16}$$

The group velocity and phase velocity $v_p = \omega/\beta$ of a signal propagating along the CRLH TL structure are plotted in Fig. 1.3. Depending on the excited frequency, a signal that propagates from the source (located on the left side) toward the load (located on the right side) along the CRLH TL structure experiences either a *backward-wave* or a *forward-wave* or an *infinite-wave* phenomenon. When $\omega_{CL} < \omega < \omega_0$, the phase velocity $v_p = \omega/\beta$ is negative because $\beta < 0$ while the group velocity is positive. In this range, the phase and group velocities are antiparallel and hence the signal experiences a backward-wave phenomenon, that is, the signal's energy flows toward the load while the signal's phase advances toward the source. On the other hand,

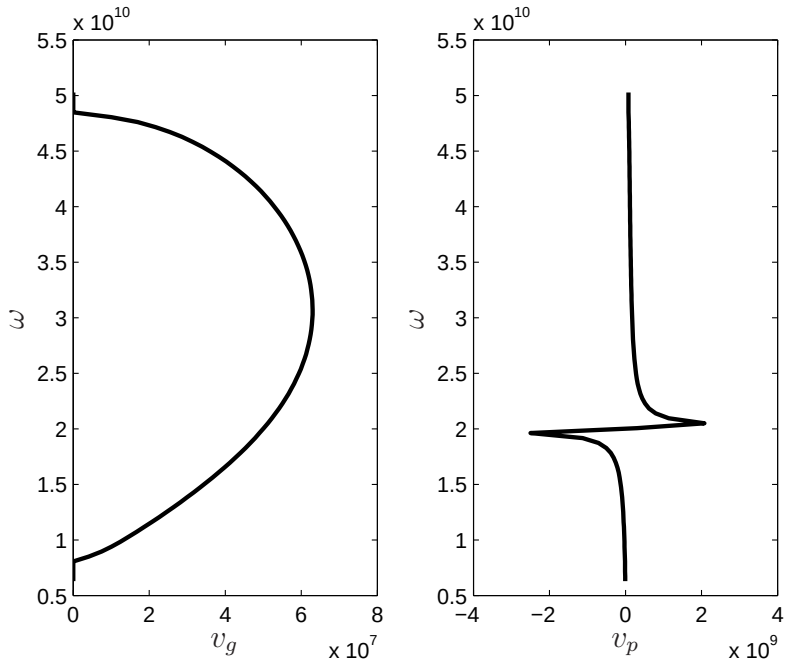

Figure 1.3 Group and phase velocities of a signal propagating along the CRLH TL structure with the same UC parameters given in the caption of Fig. 1.2.1.

when $\omega_0 < \omega < \omega_{CR}$, both phase and group velocities are positive and therefore they are parallel. In this range, the signal experiences a forward-wave phenomenon, that is, both signal's energy and phase flows toward the load. When $\omega = \omega_0$, the phase velocity is infinite because $\beta = 0$ while the group velocity is positive and given as $v_p(\omega = \omega_0) = p\omega_R/2$. At this point, the signal experiences an infinite-wave phenomenon, that is, the signal's energy still flows toward the load but the signal's phase is constant at all points along the CRLH TL structure.

1.3 Previous Applications

The preceding section has outlined some unusual properties of CRLH TL structure such as infinite-wavelength regime, full-space frequency scanning leaky-wave radiation, filtering, high frequency dispersion, and backward-wave propagation which are not commonly found in a conventional material structure. They have led to many microwave guiding and radiating applications. Some examples of these applications are listed in this section along with their operating principles and benefits [4], [5].

Guided-wave applications

- Multi-band components: The multi-band principle is essentially based on an ability to engineer the dispersion characteristic of the CRLH TLs to obtain specific phase shifts at arbitrary frequencies. Dual-band, triple-band and quad-band hybrid couplers, Wilkinson power dividers, TL matching stubs, subharmonically pumped mixer have been reported.
- Enhanced-bandwidth components: The essential principle of enhanced-bandwidth components is the combination of the CRLH's quasi hyperbolic dispersion characteristic with the conventional TL's linear dispersion characteristic to create a flatter phase difference over a wide frequency band. Power combiners/dividers, rat-race couplers, and baluns are among those enhanced-bandwidth components that have been realized with CRLH TLs.
- Tight coupled-line couplers: The arbitrary high coupling achieved in CRLH TL couplers is the result of complex coupled propagation constants within the coupling range. Both symmetric (two lines are CRLH TLs) and asymmetric (one line is CRLH TL and the other is conventional microstrip TL) coupled-line couplers fabricated in planar PCB with a coupling level close to 0 dB have been demonstrated.
- Zeroth-order resonators: The zeroth-order resonant condition is achieved by terminating CRLH TLs with short or open loads and operating CRLH TLs at the transition frequency, $\omega_0 \neq 0$. Because $\beta = 0$ at ω_0, zeroth-order resonators are independent of the physical length of CRLH TLs and therefore can be made arbitrarily small. Two types of zeroth-order resonators that have been reported are series and shunt two-port zeroth-order resonators.
- Compact components: The key to achieve compactness is to cascade a section of a CRLH TL with a section of a conventional microstrip TL to synthesize

required phase shifts in a smaller physical size. Some examples are phase-shifters, baluns, power dividers/combiners.

Radiated-wave applications

- Leaky-wave antennas: The leaky-wave radiating principle of the CRLH TL structure is due to its dispersion curve penetrating into the fast-wave region bounded by two lightlines as shown in Fig. 1.2(a). Because the phase constant β changes continuously with frequency, the unique property of CRLH TL LWAs is the full-space frequency scanning of the main beam. Leaky-wave examples such as backfire-to-endfire frequency scanned LWAs, electronically scanned (operating at a fixed frequency) LWAs, and conical-beam LWAs have been reported.
- Resonant antennas: In contrast to the traveling-wave nature of LWAs ($\beta \neq 0$), resonant antennas operate based on a resonating mechanism by terminating CRLH TLs with short or open loads, corresponding to series ω_{se} and shunt ω_{sh} resonances. Zeroth-order and dual-band, dual-polarized resonating ring antennas are examples of this type of CRLH TL antennas. In comparison with conventional resonant antennas such as microstrip patch antennas, the main benefit of CRLH TL resonant antennas is the size independent due to $\beta = 0$.

Chapter 2

Motivation, Objectives, Contributions and Coherence of the Thesis

Intense research in the past years has led to many groundbreaking CRLH TL-based components and systems for microwave guiding and radiating applications. These first-generation components and systems have unprecedented properties and performances not found in similar components or systems realized using conventional technologies. However, previous CRLH TL implementations using interdigital capacitors suffer from bandwidth limitations due to the existence of spurious transverse resonances which prohibit the use of CRLH TL MTMs in wide-band or impulse-regime applications. In addition, for guiding components such as tight coupled-line couplers, a rigorous analysis to explain the complex coupling mechanism in symmetric and asymmetric CRLH TL coupled-line couplers was still missing. Moreover, the CRLH TL leaky-wave antenna, an important radiating component, still suffered from low radiation efficiency and there was no simple method to improve this efficiency other than increasing the antenna's length.

These limitations motivated this work whose objectives is to provide practical solutions to the limitations of previous components and systems and to introduce novel CRLH TL MTM applications. Depending on their mode of operation, the main components and systems in this work are categorized into three different classes of applications: harmonic regime guided-wave, impulse regime guided-wave and harmonic regime radiated-wave. The next three sections discuss, in a greater details, the limitations of previous implementations and components, the solutions to these limitations, and some new CRLH TL MTM applications and components. Finally, section 2.4 discusses the coherence in the choice of articles presented this work.

2.1 Harmonic Regime Guided-wave Components

Three examples of CRLH TL MTM harmonic regime guided-wave components presented in this work are 1) BPF, 2) series power divider, and 3) coupled-line couplers. These components are commonly found in many systems and their functions are to control the signal's frequency response (filters), to distribute (power dividers) and to sample (couplers) the signal at a certain point in a system. They can be realized using various technologies depending on the requirements of each system. In this work, the three components are implemented using CRLH TL MTMs. As presented in chapter 1, the CRLH TL MTM is attractive because it has unprecedented properties suitable for realizing filters, power dividers and couplers with unparalleled characteristics. Subsections 2.1.1 and 2.1.2 discuss some limitations of previous interdigital capacitor CRLH TL structure and coupled-line couplers. The MIM capacitor, which introduced in this work as an important replacement of the interdigital capacitor, is an enabling element of new CRLH TL MTM applications. The benefits and applications of MIM capacitors are presented in subsection 2.1.3. Finally, subsection 2.1.4 discusses the generalized CMT analysis which explains the complex coupling of CRLH TL coupled-line couplers.

2.1.1 Limitations of Interdigital Capacitor CRLH TL Structure

The planar CRLH TL structure shown in Fig. 1.1(a) is implemented in a form of printed microstrip TL loaded with series interdigital capacitors and shunt stub inductors on a dielectric substrate. An advantage of interdigital capacitors is its simple planar implementation requiring only one metal layer. However, the low coupling and the presence of transverse current loops (resonances) between interdigitated fingers of the capacitors limit the maximum achievable capacitance value and reduce the highest operating frequency and hence the bandwidth of interdigital capacitors [12]. To increase the capacitance value, one can increase the length of interdigitated fingers, or reduce the gap between these fingers or increase the number of fingers. Unfortunately, the size of the gap is often restricted by the photolithographic resolution constraint and therefore only the length and the number of fingers can be conveniently adjusted. However, increasing the length and/or the number of fingers enlarges the overall size of the interdigital capacitors. In addition, a higher number of fingers results in a larger

number of transverse resonances as well as a lower frequency for the first transverse resonance. Consequently, the usable bandwidth is further reduced.

Because of these limitations, the planar CRLH TL structure implemented with interdigital capacitors has two major drawbacks. The first drawback is a large UC's size p due to a low capacitance per unit area of interdigital capacitors. The second drawback is a narrow bandwidth due to the presence of transverse resonances within the passband of the planar CRLH TL structure. In addition to these drawbacks, the planar interdigital capacitor CRLH TL UC has an inherent asymmetric configuration, which leads to an asymmetric CRLH TL structure. The asymmetric CRLH TL structure is undesirable because it has different Bloch impedance values at its input and output ports and therefore complicates the simultaneous matching of the two ports. In order to obtain a symmetric configuration, it is then necessary to redesign the interdigital capacitor of the first and last UCs so that it is twice the value of those of inner UCs. This is illustrated in Fig. 1.1(a), where the first and last capacitors have more number of fingers as well as a smaller gap between these fingers. In addition to more transverse resonances due to a larger number of fingers, the redesign of first and last capacitors further adds complexity to the overall design process of the CRLH TL structure.

2.1.2 Limitations of Even/Odd-mode Analysis of CRLH TL Couplers

The CRLH TL coupled-line coupler implemented represent a new type of planar couplers that exhibit a high and arbitrary coupling level not commonly available in conventional planar coupled-line couplers [13], [14]. The high-coupling phenomenon as well as its coupling level and frequency range have been previously explained using the even- and odd-mode decomposition technique. Since the even/odd-mode analysis decomposes the couplers' four-port structure into two two-port structures, it fails to address the exact and complex coupling nature of the planar CRLH coupled-line couplers. Additionally and more importantly, the even/odd-mode approach does not apply to asymmetric coupled-line couplers due to the structural difference of the two types of TL.

2.1.3 Metal-Insulator-Metal (MIM) Capacitor CRLH TL Structure

The limitations of interdigital capacitors have prevented the use of CRLH TL structure from wide bandwidth applications such as wideband filters and couplers. Therefore, another configuration free from transverse resonances and with high capacitance per unit area is needed to extend the applications of CRLH TL structure. The objective is to obtain a new CRLH TL structure with maximal bandwidth operation and a compact and symmetric configuration.

The MIM capacitor meets the capacitor's requirements for such a new CRLH TL structure. Formed by two parallel plates, the MIM capacitor's capacitance is a function of the overlapping area of the two plates and of the separation and permittivity of dielectric material between the two plates. A high capacitance per unit area can be easily achieved by selecting a thin dielectric material with a high permittivity constant. In addition, the MIM capacitor does not suffer from any resonances other than its self-resonance due to the presence of the inherent parasitic inductance of the plates. However, since the parallel plates have a wide width, the parasitic inductance is low and hence the MIM capacitor's self-resonant frequency is very high and above most of the frequency ranges of interest. The two parallel plates of MIM capacitors necessitate two metallic layers in addition to the ground plane layer required for planar CRLH TL structures. Fortunately, multilayer PCB fabrication has become a routinely task and is readily available by vertically aligning and bonding single layer substrates.

The advantages of MIM capacitors lead to a new MIM capacitor CRLH TL architecture that is symmetric (symmetry will be further explained in subsection 3.1.3), compact and free of transverse resonances. These characteristics make the MIM capacitor CRLH TL structure suitable for wideband filter, coupler and compact power divider applications, just to name a few. Wideband filters and couplers were not possible using the previous CRLH TL architecture due to the presence of spurious transverse resonance of interdigital capacitors. On the other hand, a BPF based on the MIM capacitor CRLH TL structure achieves an extremely wide geometric FBW and a sharp rejection in its stopbands. Coupled-line couplers are also implemented using MIM capacitor CRLH TL structures and have a two-fold reduction in the electrical size compared to their interdigital counterpart. As a last example of MIM

capacitor CRLH TL architecture, a tunable series power divider demonstrates a flexibility in designing a power distributing network with an arbitrary number of ports as well as an arbitrary separation between the ports.

2.1.4 Generalized Coupled-Mode Theory (CMT) Analysis of CRLH TL Coupled-line Couplers

In addition to the realization of MIM capacitor CRLH TL coupled-line couplers with a two-fold size reduction, an important contribution of this work is the generalized CMT analysis of CRLH TL couplers explaining, for the first time, the complex coupling phenomena governing both the symmetric and the asymmetric CRLH TL couplers. The CMT analysis uses a generalized CRLH TL circuit model, capable of modelling conventional RH TLs and CRLH TLs in symmetric and asymmetric CRLH TL couplers. A symmetric coupler with two CRLH TLs, the coupling analysis shows that maximal coupling occurs at the transition frequency ω_0 where the propagation constant of both isolated CRLH TLs is zero $\beta_1 = \beta_2 = 0$. On the other hand, in an asymmetric coupler with one conventional RH TL and one CRLH TL, maximal coupling occurs when the propagation constants of the isolated lines are different from zero and exactly opposite $\beta_1 = -\beta_2 \neq 0$. In both cases, coupling is shown to be proportional to the coupling length which leads to an arbitrary level of coupling, theoretically up to 0 dB. Closed-form expressions for the coupling are given explicitly for both TEM and quasi-TEM couplers. In contrast to conventional microstrip couplers, it is found that the CRLH TL coupler's propagation constants are purely imaginary and complex within the coupling range for the symmetric and asymmetric couplers, respectively.

2.2 Impulse Regime Guided-wave Components and Systems

Unlike the harmonic-regime devices, where signals are restricted to continuous waves, impulse-regime devices primary support transient pulse signals. Many applications such as pulse radars [15], time-division multiplexing pulse radio systems [16], and emerging pulse UWB wireless communications [17] operate in the impulse regime.

An important advantage of these impulse-regime systems is a simple front-end architecture. The transmitter often consists of a pulse generator, a pulse modulator, and a power amplifier. On the other side, the receiver might include some or all of the following components: a low-noise amplifier, a mixer, a local oscillator, and a pulse demodulator. Within the front-end, the pulse generator and pulse position modulator/demodulator are essential components that set a maximum resolution (by the pulse width), detection range and data rate (by the pulse repetition rate) of these impulse-regime systems.

A pulse generator and pulse modulator can be realized either using digital or analog technology. Digital technology is attractive at low frequency and for low power applications since it features low cost, small size, and high reliability [18], [19]. However, at high frequencies, digital technology is inappropriate due to performance limitation of digital to analog conversion and noise. Therefore, analog technology is still preferred for high frequency, high power, and low noise applications [20], [21]. This work proposes an analog time differentiation device suitable for a pulse generator and a pulse position modulating transmitter based on an analog delay line. The enabling component of the time differentiator is a passive, microstrip coupled-line coupler. For the PPM transmitter, the key element is the CRLH TL operating as a tunable dispersive delay line. The PPM transmitter is the first system of impulse-regime MTM applications. Novel impulse-regime MTM applications exploiting dispersion-engineering concept has motivated this work as well as those of the author's colleagues, which are introduced in subsection 2.2.1. A dispersive delay line is the main component in an impulse regime system and can be realized using different technologies other than planar CRLH TL. Subsection 2.2.2 discusses the advantages and disadvantages of available technologies to realize the dispersive delay line for impulse regime applications. Two contributions of this work, the analog time differentiator and the PPM transmitter, are summarized in subsections 2.2.3 and 2.2.4, respectively.

2.2.1 Impulse Regime MTM Applications

Due to its non-resonant and low-loss characteristics, the CRLH TL has already enabled many guiding and radiating applications as listed in section 1.3. All of these previous applications operate in the harmonic regime and while some of them might support multi-band (dual-band, tri-band, quad-band) operations, they have been

devised for narrow-band systems. The BPF presented in the previous section is the first wide-band component in which a new approach of dispersion-engineering, based on phase shaping other than magnitude control, has been utilized. Although the wide-band BPF was designed for harmonic regime operation, it could also be utilized in impulse regime applications.

In dispersion engineering, the phase (dispersion curve) in the passband is engineered to specifically meet requirements such as the absolute group delay value or the slope of the group delay within a certain frequency band. Dispersion engineering has been employed to design impulse regime components such as a pulse-compression filter in an frequency modulated pulse compression radar [15] or a microstrip quadratic-phase filter in a real-time spectrum analyzer [22]. The pulse-compression filter is a dispersive delay line whose delay time or group velocity is a function of frequency and whose function is to compresses a chirped frequency-modulated signal having a low amplitude but wide spectral bandwidth into a high amplitude but narrow spectral bandwidth signal. The microstrip quadratic-phase filter is an impedance modulated periodic structure operating in the Bragg condition which again provides a group velocity as a function of frequency required for the operation of a real-time spectrum analyzer.

CRLH TL MTMs are inherently dispersive because of their phase and group velocities vary strongly with frequency, as seen in (1.9a) and (1.16). Therefore, CRLH TL MTMs are suitable for dispersion-engineering components operating in the impulse regime [23]. However, the dispersion-rich characteristics of CRLH TL MTMs was not utilized in previous MTM applications. Only recently, this dispersion is properly exploited to design novel impulse-regime components and systems such as a PPM transmitter presented in this dissertation, a tunable pulse delay line [24], a true time delayer [25], compressive receivers [26], and a real-time spectrum analyzer [27].

2.2.2 Alternative Impulse Regime Technologies

Dispersion in the dispersive delay line can be achieved using different technologies which are categorized into two groups depending on their modes of operation. The first group is the *transmission* group, which includes surface acoustic wave (SAW) and magneto static wave (MSW) devices. Both SAW and MSW devices provide large absolute time delays and large time-bandwidth products. However, SAW devices are

suitable only for applications at low frequencies due to photolithographical fabrication limitations of transducers converting microwaves to SAWs and vice versa [28]. On the other hand, MSW devices can operate at high frequencies but require magnetic materials in addition to a biasing permanent magnet which are lossy, bulky and incompatible with planar microwave circuits [29].

The second group is the *reflection* group, which consists of multi-section coupling structures and chirped microstrip TLs. Due to their microstrip TL structures, reflection-mode devices can be realized conveniently in planar PCB fabrication. Multi-section coupling structures are composed of a number of series-connected coupled-line couplers and can be designed for high-frequency and wide-band operation. However, their absolute time delay and bandwidth are proportional to the length of the structure, which is often in an order of tens of the guided wavelength [30]. This long length results in an extremely high loss. Somewhat simpler than the multi-section coupling structure, a chirped microstrip TL is a periodic structure of high- and low-impedance TL sections operating in the Bragg condition, i.e. input signal is totally reflected rather than being transmitted [22]. However, similar to the multi-section coupling structure, its absolute time delay is also dependent on the TL's length and so the chirped microstrip TL has a high loss. In addition to being highly lossy, reflection-mode devices require a circulator to isolate the input signal and the time-delayed output signal.

2.2.3 Time Differentiator and Analog Pulse Generation Application

As mentioned earlier, analog technology is preferred than its digital counterpart due to its advantages of high speed and low noise. This work proposes, for the first time, an analog time differentiator based on a passive microstrip coupled-line coupler. This time differentiator is capable of providing first and second-order time differentiations of an input pulse. For the first-order differentiation, a single coupled-line coupler is needed, while for the second-order differentiation, an additional time delay circuit is required for operation. The time differentiator can be directly deployed in an analog pulse generator and is an unique impulse regime application of the conventional coupled-line couplers which operate frequently in the harmonic regime.

2.2.4 Analog Delay Line and Pulse Position Modulation (PPM) Application

The dispersive delay line employed in this work operates in the transmission mode and utilizes planar MIM capacitor CRLH TLs. In comparison with the alternative technologies of subsection 2.2.2, the planar MIM capacitor CRLH TL is more compact and lower-loss structure requiring no magnetic material and permanent magnet. Moreover, the MIM capacitor CRLH TL can be designed to operate at low or high frequency and exhibits a wide bandwidth.

The PPM transmitter is the first MTM-based impulse regime system application that exploits the dispersive property of CRLH TLs. Because tunable time delays can be achieved with a planar MIM capacitor CRLH TL using an external mechanism [24], a binary and a quaternary modulation schemes are demonstrated using the same PPM transmitter proposed in this work. Higher-order modulation schemes can also be supported by this transmitter.

2.3 Radiated Wave Components and Systems

The two novel power-recycling concepts introduced in this section enhance low radiation efficiency of LWAs. LWAs are attractive due to their structural simplicity (absence of a feeding network), high directivity (because of their travelling-wave nature), and easy fabrication. LWAs are classified into two different types depending on their physical guiding structures. The first type, the *uniform* LWAs, has a uniform waveguiding structure along the direction of propagation. Some uniform LWAs might have small and continuous tapering structures along the length to improve and control the sidelobe level. The second type, the *periodic* LWAs, has the waveguiding structure being periodically modulated along the direction of propagation. These two types have distinct operating characteristics and advantages but both of them suffer from severe limitations in terms of scanning range and radiation efficiency. These limitations are discussed in the following subsection 2.3.1. Subsection 2.3.2 presents the CRLH LWA and its full-space scanning benefit. Like other LWAs, the CRLH LWAs also suffer from low radiation efficiency. Two circuit-based methods proposed in this work as simple solutions for radiation efficiency enhancement of LWAs are presented in subsection 2.3.3.

2.3.1 Limitations of Leaky Wave Antennas (LWAs)

LWAs are either uniform or periodically modulated waveguiding structures that allow energy to continuously leak out as it propagates along the direction of propagation. In order to radiate, both types of LWAs must have a complex propagation constant $\gamma = \alpha + j\beta$ with the attenuation constant $\alpha \neq 0$ and the phase constant β with $-k_0 \leq \beta \leq k_0$. The phase constant β controls the direction of the main beam, which is given approximately in (1.13), whereas the attenuation constant α is the leakage and therefore controls the radiation efficiency of LWAs. Because β is a function of frequency, LWAs can scan with frequency from backfire to endfire direction as β varies from $-k_0$ to $+k_0$.

The frequency scanning capability of LWAs is an important advantage for scanning antenna applications. However, conventional uniform and periodic LWAs suffer from a limited scanning range. Uniform LWAs have a dominant propagating mode that is fast and positive, i.e. $0 < \beta_{uniform} \leq k_0$. As a result, uniform LWAs only radiate and scan in the forward quadrant between broadside and endfire direction. In addition, broadside radiation is prohibited because β is positive. Recently, a new ferrite-loaded uniform LWA introduced by Kodera and Caloz [31] is the first uniform LWA that has $-k_0 \leq \beta_{uniform} \leq k_0$ and therefore can radiate in both forward and backward quadrants. However, this uniform LWA requires a lossy ferrites and undesirable magnetic bias.

Periodic LWAs have periodically modulated structures and so support an infinite number of space harmonics $n = 0, \pm 1, \pm 2, ...$ Each space harmonic has a phase constant β_n related to the fundamental space harmonic $n = 0$ of the unmodulated structure as $\beta_n = \beta_0 + 2n\pi/p$, where p is the period of the periodically modulated structure. While fundamental $n = 0$ space harmonic of periodic LWAs is slow and does not radiate, other *negative* space harmonics $n = -1, -2, ...$ can be made to be fast and radiate by appropriately designed the period p. For periodic LWAs radiating a single beam, the period p is designed so that the $n = -1$ space harmonic is fast while all others $n = -2, -3, ...$ are slow. In contrast to uniform LWAs, periodic LWAs operating in the $n = -1$ space harmonic can radiate in both backward and forward quadrants. This is because the phase constant of the first space harmonic can be designed such that $-k_0 \leq \beta_{-1} = \beta_0 - 2\pi/p \leq k_0$. Unfortunately, broadside radiation is also not possible in periodic LWAs because at broadside the period p of the periodic waveguiding structures is equal to one wavelength ($\beta_{-1} = \beta_0 - 2\pi/p = 0 \rightarrow$

$p = 2\pi/\beta_0 = \lambda$) corresponding to a standing wave where input signal is total reflected rather than being radiated. Very recently, Paulotto *et. al.* [32] has introduced a novel technique to permit broadside radiation in periodic LWAs. However, this proposed technique requires a delay line and a quarter-wave transformer within each period p. The presence of the quarter-wave transformer results in a very narrow frequency bandwidth and limited scanning angles around the broadside direction. Tab. 2.1 summarizes the performances of uniform and periodic LWAs in terms of scanning range and broadside radiation capability.

Table 2.1 Performances of Uniform and Periodic LWAs

	Uniform LWAs	Periodic LWAs
Scanning Quadrants	Forward	Backward and Forward
Broadside Radiation	No	No

As mentioned earlier, the attenuation constant α of the travelling wave relates to the leakage rate per unit length of the waveguiding structure. Travelling LWAs with a small α are advantageous as they have a long *effective* aperture which provides a narrow beam (high directivity). However, the *physical* length must be sufficiently long so that most of the power has leaked out before reaching the termination. For 90% efficiency, a typical LWA might be greater than 10 wavelengths long, which is impractical at low frequencies. As a result, most practical and finite size LWAs suffer from a low radiation efficiency.

2.3.2 Full-Space Scanning Benefit of CRLH TL LWAs

As discussed in the preceding subsection, uniform and periodic LWAs of finite lengths have two fundamental limitations: 1) narrow scanning range and 2) low radiation efficiency. These limitations have prohibited the application of LWAs in many low-frequency systems.

CRLH TL LWAs are periodic LWAs and have a microstrip implementation using interdigital capacitors and shorted stub inductors as shown in Fig. 1.1. An important difference between CRLH TL LWAs and conventional periodic LWAs is that the CRLH TL LWAs has a fast $n = 0$ space harmonic. As shown in Fig. 1.2(a), the disper-

sion curve of the CRLH TL LWA operating in its fundamental $n = 0$ space harmonic penetrates the fast-wave region and intersects the $-k_0$ and $+k_0$ light lines at ω_{BF} and ω_{EF}, respectively. Consequently, the CRLH TL LWA radiates in both backward and forward quadrants for $\omega \in [\omega_{EF}, \omega_{BF}]$. Another key advantage of CRLH TL LWAs is that broadside radiation is possible because at broadside frequency ω_0, the periodic CRLH waveguiding structure operates in the infinite-wavelength regime $\beta = 0, \alpha \neq 0$ and does not resonate. As a result, the input signal propagates and radiates a beam at broadside since all the UC elements have the same phase. In summary, the planar CRLH TL LWA with its full-space (backward and forward quadrants including broadside direction) scanning benefit alleviates the narrow scanning limitation of periodic LWAs.

2.3.3 Power Recycling Efficiency Maximization in LWAs

While the CRLH LWA provides an important full-space scanning benefit compared to conventional periodic LWAs, it suffers from the typical low radiation efficiency of periodic travelling-wave antennas. A straightforward approach to improve the radiation efficiency is to increase the antenna's length. But as discussed above, this approach results in a impractical size for applications at low frequencies. Another solution is to control the leakage rate by independently engineering the attenuation constant. However, any attempt to control the attenuation constant α leads to a change in the phase constant β following from Kramers-Kronig relations for the complex propagation constant $\gamma = \alpha + j\beta$ [33]. As a consequence, the main beam points to a different direction or, in the extreme case, disappears because the phase constant becomes greater than the free-space wavenumber, i.e. $|\beta| \geq k_0$.

In [34], Gomez-Tornero *et. al.* proposes a mechanism to independently control the attenuation constant to improve radiation efficiency of a microstrip LWA operating in its second higher order mode. This technique requires two metallic parallel plates to be erected on both sides of the microstrip line and on top of the dielectric substrate supporting the microstrip line. The height of these plates controls the amount of power leakage from the microstrip LWA's second higher order mode and therefore does not alter the phase constant of this mode. This novel mechanism has two main drawbacks. The first drawback is that it is only applied to LWAs supporting lateral electric field which is perpendicular to the metallic plates. Therefore, this mechanism

cannot be applied to improve the radiation efficiency of the CRLH LWA because its electric field is longitudinal. The second drawback is the requirement of the parallel plates which are bulky and inappropriate for planar waveguiding structure.

The power-recycling techniques proposed in this work provide simple solutions to systematically maximize the radiation efficiency of the CRLH LWA. The main objective is to maximize the radiation efficiency without changing the phase constant or increasing the waveguiding structure's length of the original CRLH LWA. The two proposed techniques reuse the frequently wasted power at the termination of a finite length 2-port CRLH LWA and reapply this power to the input of neighbouring antenna elements (cross power-recycling technique) or to the input of the same antenna (self power-recycling technique). The total radiated power is thus effectively increased and therefore the radiation efficiency, computed as a ratio of radiated power and input power, increases. Because the power-recycling techniques are *external* to the CRLH LWAs, they do not alter the phase and attenuation constants nor the length of the original waveguiding structures. It is worth to mention here that since the proposed cross and self power recycling are external, circuit-based techniques, they are ideally applicable to any 2-port uniform or periodic LWAs. Details of the proposed power-recycling techniques are given in Chapter 5.

2.4 Organization and Coherence in the Choice of the Articles

This thesis is written in the format of published articles. The articles are organized in three classes of CRLH TL applications: harmonic regime guided-wave, impulse regime guided-wave and radiated-wave applications. This section outlines the organization of the dissertation and the selected articles in each chapter.

Chapter 3 Harmonic Regime Guided-wave Components

This chapter presents three passive components that are generally operating in the harmonic regime. They are a wideband bandpass filter [35], an infinite-wavelength series power divider [36], and enhanced coupled-line couplers [37]. These components are selected to demonstrate the filtering, the infinite-wavelength at a non-zero frequency, and the complex and non-harmonic coupling properties of CRLH TL MTMs.

Chapter 4 Impulse Regime Guided-wave Components and Systems

This chapter presents first- and second-order time differentiators suitable for analog pulse generator applications and a PPM transmitter system found in impulse regime applications. The time differentiator utilizes a passive coupled-line coupler and a time delayer to generate first- and second-order pulse differentiations [38]. The PPM transmitter exploits the tunable pulse delay property of the CRLH TL dispersive delay line [39]. Although the time differentiators do not use a CRLH TL, they are still selected for presentation here because they represent unique passive components for analog pulse generation used in many impulse regime applications.

Chapter 5 Radiated-wave Components and Systems

This chapter presents two novel power-recycling concepts to maximize the radiation efficiency of LWAs. The first cross power-recycling concept utilizes a series feeding network and a power divider to recycle non-radiated power between LWA array's elements and therefore can be applied to any 2-port LWA arrays [40]. The second self power-recycling concept utilizes a feedback system to recycle non-radiated power and combine it with the input signal for efficient radiation. The feedback system is external to the LWA and thus it is applicable to maximize the radiation efficiency of any 2-port LWA [41].

Chapter 6 Assessment of the Thesis's Contributions

A general assessment of the thesis's contributions are discussed in this chapter.

Chapter 7 Conclusions and Future Works

This chapter concludes with a summary of the work performed in this thesis and a list of possible extensions of this work.

Chapter 3

Harmonic Regime Guided-Wave Components

This chapter is the first of two chapters which present the guided-wave components and systems developed in the thesis. Components operating in the harmonic regime are the focus of this chapter. In all of the guiding applications discussed in the present and the next chapters, the applied electromagnetic energy is confined inside the components and systems and generally does not leak out to the surrounding space. The three components discussed in this chapter exploit the filtering characteristic, infinite-wavelength operation and complex propagation constant of CRLH TLs.

This chapter is organized as follows. Section 3.1 presents a wideband BPF which is implemented in a MIM capacitor CRLH TL architecture. Section 3.2 presents a tunable arbitrary N-port series power divider operating in the infinite-wavelength regime. The series power divider is implemented using the MIM capacitor CRLH TL in a shielded configuration to avoid any leakage loss. Finally, section 3.3 presents three examples of CRLH TL coupled-line couplers. The couplers are analyzed using the coupled-mode theory, verified numerically with electromagnetic simulation and demonstrated experimentally.

3.1 Article 1: Broadband Highly Selective Band-pass Filter based on a Tapered Coupled-Resonator (TCR) CRLH Structure

A BPF is a two-port network which transmits the input signal at the frequencies within its passband and rejects the input signal in its stopbands [42]. In practical BPFs, these fundamental characteristics translate into complex design parameters such as bandwidth, insertion loss in the passband and attenuation in the stopbands.

Size and cost are other equally important parameters in the design of BPFs. To achieve a wide passband and sharp rejection, a number of new BPF structures were proposed, based for instance on spurline resonators [43], ring resonators [44], [45], complementary split ring resonators [46], combination of highpass and lowpass filters [47], or aperture compensation technique [48]. All of these BPFs are implemented in a planar, low profile, and low cost microstrip technology and exhibit an ultra-wide fractional bandwidth (FBW) greater than 20% of the centre frequency.

This work introduces a new BPF design based on the concept of CRLH TL. The CRLH TL concept emphasizes on the design of phase response between the input and output ports instead of amplitude response commonly found in conventional filter designs by the insertion loss method. Consequently, the CRLH TL BPF relaxes the insertion loss in its passband to achieve sharp rejections at low and high cutoff frequencies as well as a wide passband. As it will become apparent later, the high selectivity in the lower cutoff frequency is due to the inherent slow-wave property of the CRLH TL in its LH range while the high selectivity in the higher cutoff frequency is due to the attenuation poles introduced by the tapered coupled resonators. In order to achieve the wide passband, the BPF is implemented in a new MIM capacitor based CRLH TL architecture proposed for the first time in this work. The proposed CRLH TL BPF obtains a measured FBW of 115% and sharp rejections at both cutoff frequencies.

This section is organized as follows. An overview of the properties of conventional CRLH TLs relevant to BPF applications is given in subsection 3.1.1, followed by an introduction of the modified TCR CRLH TL structure providing high selectivity at the higher cutoff frequency. The alternative MIM capacitor based CRLH TL implementation for wideband BPF applications is presented in subsection 3.1.3. Subsections 3.1.4 and 3.1.5 provide the results and comparison with conventional BPF having the same order. Finally, subsection 3.1.6 outlines some conclusions.

3.1.1 Filtering Characteristics of CRLH TLs

Fig. 3.1(a) shows the equivalent circuit model of a conventional symmetrical CRLH unit cell (UC). The symmetrical UC is preferred over its asymmetric counterpart because it has the same Bloch impedances Z_B seen at the input and output ports and therefore both ports can be simultaneously matched to the same impedance value

[4]. This model can be seen to be constituted by the combination of a low-pass filter section composed of $L_R/2$ inductors and C_R capacitors and of a high-pass filter composed of $2C_L$ capacitors and L_L inductors. Under input and output ports matched condition, the frequency transfer function of the CRLH UC exhibits the bandpass behavior shown by the solid curve in Fig. 3.1(b), which is derived from the [ABCD] matrix of (1.1) [42] and given as

$$S_{21}(s) = \frac{2L_L C_L s^2}{1 + (L_R C_L + L_L C_R + 2L_L C_L)s^2 + L_R C_R L_L C_L s^4} \tag{3.1}$$

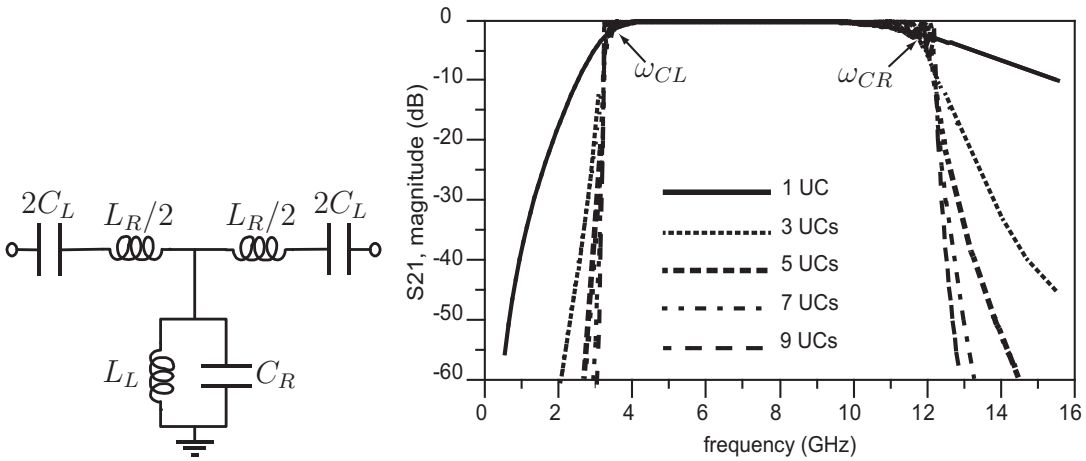

Figure 3.1 Conventional CRLH structure. (a) UC equivalent circuit model. (b) Transmission response as a function of the number of UCs.

Under the so-called balanced condition, $L_R C_L = L_L C_R$, the transition frequency ω_0, lower (LH) and upper (RH) cutoff frequencies [as derived in (1.12), (1.15a), (1.15b)

and provided here again for convenience], and the bandwidth of the CRLH UC are

$$\omega_0 = \frac{1}{\sqrt[4]{L_R L_L C_R C_L}} = \sqrt{\omega_R \omega_L}, \tag{3.2}$$

$$\omega_{CL} = \omega_R \left(\sqrt{1 + \frac{\omega_L}{\omega_R}} - 1 \right), \tag{3.3}$$

$$\omega_{CR} = \omega_R \left(\sqrt{1 + \frac{\omega_L}{\omega_R}} + 1 \right), \tag{3.4}$$

$$\text{BW} = \omega_{CR} - \omega_{CL} = 2\omega_R, \tag{3.5}$$

where $\omega_R = 1/\sqrt{L_R C_R}$ and $\omega_L = 1/\sqrt{L_L C_L}$ are the cutoff frequencies of the isolated low-pass and high-pass filter sections, respectively. The four unknown inductance and capacitance values can be calculated using (3.2)-(3.5) for given bandwidth and cutoff frequencies specifications. The inductance and capacitance values which yield the transmission response shown in 3.1(b) are listed in Table 3.1. The transmission responses of the ladder network constituted by 3, 5, 7, and 9 cascaded UCs are also shown in Fig. 3.1(b). They reveal that the CRLH cutoffs become sharper as the number of UCs increases up to a certain number of UCs, which is around 7. Therefore, 7 UCs will be selected to achieve the best trade-off between high-selectivity and compactness.

As can be seen from (3.3) and (3.4), the cutoff frequencies do not vary with the number of UCs. The FBW of the CRLH TL can be computed by taking the ratio of BW and the average center frequency, ω_c. Two commonly used average center frequency definitions, arithmetic average and geometric average center frequency and their corresponding fractional bandwidth are given in the following equations for the optimum case where the cutoff frequencies of the isolated low-pass and high-pass section are equal, i.e. $\omega_R = \omega_L$,

Arithmetic average

$$\begin{aligned} \omega_c &= (\omega_{CL} + \omega_{CR})/2 \\ &= \omega_R \sqrt{1 + \omega_L/\omega_R} \\ &= \sqrt{2}\omega_R. \end{aligned} \tag{3.6}$$

metic bandwidth is

$$\begin{aligned} \text{FBW} = \frac{BW}{\omega_c} = \frac{2\omega_R}{\sqrt{2}\omega_R} \\ = \sqrt{2} \text{ or } 141.42\% \end{aligned} \tag{3.7}$$

Hence, the maximum fractional *arith-*

Geometric average

$$\begin{aligned}\omega_c &= \sqrt{\omega_{CL}\omega_{CR}} \\ &= \sqrt{\omega_R\omega_L} \\ &= \omega_R = \omega_0.\end{aligned} \tag{3.8}$$

Hence, the maximum fractional *geometric* bandwidth is

$$\begin{aligned}\text{FBW} = \frac{BW}{\omega_c} = \frac{2\omega_R}{\omega_R} \\ = 2 \text{ or } 200\%\end{aligned} \tag{3.9}$$

Equation (3.7) or (3.9) reveals that CRLH TLs have, in general, a FBW larger than 20% and therefore are suitable for ultra wideband (UWB) filter applications.

A striking difference between the higher and lower stopband rejection may also be observed in the graph of Fig. 3.1(b). When the number of UC is relatively small (less than 7 here), the low frequency stopband has a sharper rejection than that of the high frequency stopband. This leads to an unequal attenuation of spurious signals in the stopbands. In order to achieve a sharp rejection also at the higher cutoff, transmission zeros are introduced with the modified tapered coupled resonator (TCR) CRLH TL presented in the next section.

3.1.2 Tapered Coupled-Resonator CRLH BPF

Single UC Coupled-Resonator (CR) CRLH TL and Scheme for Rejection Sharpness and Bandwidth Improvement

Fig. 3.2(a) shows the equivalent circuit model for the unit cell of the proposed tapered coupled-resonator (TCR) CRLH TL. The CR (which will have different parameter values in the different cells building up the complete TL) is introduced at the center point of the circuit to preserve the symmetry of the CRLH UC. This CR consists of a coupling capacitor C_c in series with a resonator tank composed of a shorted stub inductance L_s and a parasitic capacitance C_s. An approximation of the CR CRLH UC transmission response is derived from the corresponding [ABCD] matrix of CR CRLH UC and given by

$$S_{21}(s) = \frac{2L_L C_L s^2[1 + L_s(C_c + C_s)s^2]}{1 + Ks^2 + Ms^4 + Ns^6}, \tag{3.10}$$

where

$$K = (L_R C_L + L_L C_R + 2L_L C_L),$$
$$M = [L_s(C_C + C_s)(L_R C_L + L_R C_R + 2L_L C_L) + L_R C_R L_L C_L],$$
$$N = C_L L_L L_R L_s[C_R C_s + C_c(C_R + C_s)],$$

where the denominator coefficients with negligibly small values have been ignored. Equation (3.10) indicates that the CR introduces in the CRLH TL a transmission zero at

$$\omega_z = \frac{1}{\sqrt{L_s(C_s + C_c)}} \tag{3.11}$$

as shown in Fig. 3.2(b) If the CR CRLH TL includes several CR CRLH UC cascaded in series so as to form a ladder network, the order of this transmission zero is increased, which results in a sharper rejection as the number of UCs is increased. Comparing the transmission responses of the CR CRLH UC (Fig. 3.2(b)) with that of the conventional CRLH UC (Fig. 3.1(b)) at the higher stopband, we observe that the CR transmission zero leads to a dramatic improvement in terms of rejection sharpness in the close vicinity of the high cutoff frequency. Unfortunately, this transmission zero also generates an undesired transmission pole, representing a spurious passband, at the slightly higher frequency, which is derived from the transfer function as

$$\omega_p = \frac{1}{\sqrt{L_s\left(C_s + \frac{C_R C_c}{C_R + C_c}\right)}} \tag{3.12}$$

and shown in Fig. 3.3

In order to suppress this transmission pole, an additional cell introducing a transmission zero exactly at its frequency may be added to the structure. This transmission zero in turn introduces another transmission pole at an even higher frequency, and so on. The process can be reiterated by adding up to the structure a sufficient number of UCs until the desired level of rejection sharpness and bandwidth is achieved. From (3.11) and (3.12), the locations of the transmission zeros and poles can be varied by tuning either the coupling capacitance C_c or the shorted stub resonator's shunt

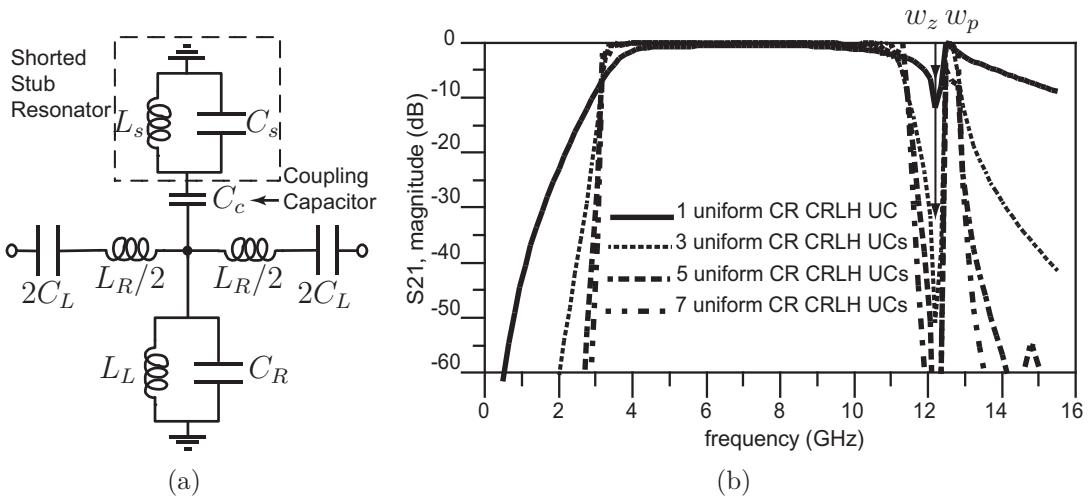

Figure 3.2 Uniform coupled-resonator (CR) CRLH TL structure. (a) UC equivalent circuit model. (b) Transmission response as a function of the number of UCs.

inductance ℓ_s. Fig. 3.3 shows the transmission response of the CR CRLH UC with three different shorted stub resonator's frequencies. The different curves in this graph all correspond to a single CR CRLH UC and not to a complete structure. However, it is well-known in fundamental filter theory [49] that a filter consisting of several cells with different transmission and attenuation zeros connected in series exhibits a response including all of theses zeros. Therefore, a simple series cascading of the different cells into the overall filter structure will yield a response essentially consisting of the superposition of the different transmission zeros if the CRs have sufficiently high Q values and are sufficiently separated from each other in frequency to avoid inter-coupling.

Tapered Coupled Resonator CRLH TL

Following the principles evoked in the previous subsection a TCR CRLH TL filter can be designed with the desired higher-frequency cutoff performances. The lower-frequency cutoff is unaffected by the CRs due to their high Q. To obtain symmetric input/output responses, a CR tapered symmetrically with respect to the center of the structure is used. This introduces the constraint of an odd number of TCR CRLH UCs (Fig. 3.3). Fig. 3.4 shows the transmission response of a TCR CRLH BPF

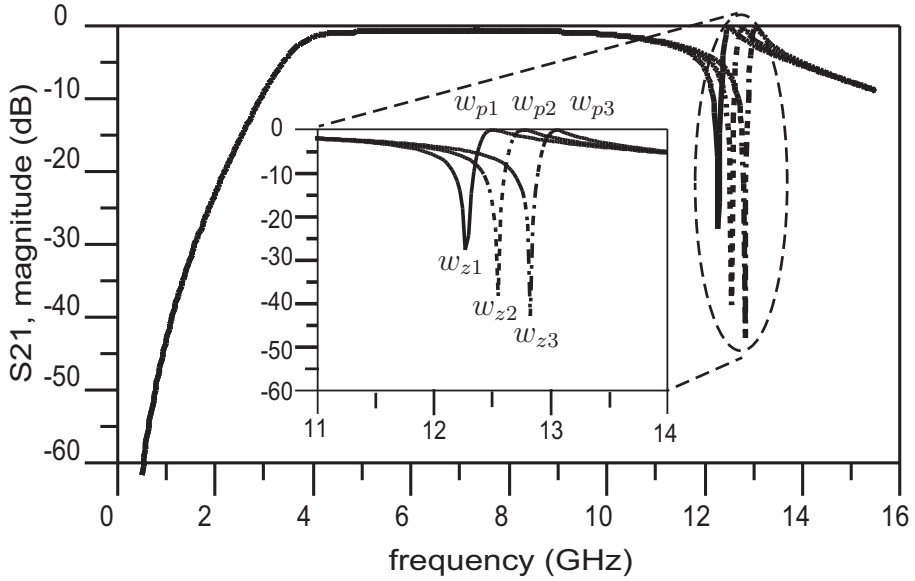

Figure 3.3 Transmission response of the CR CRLH UC with different resonator's frequencies.

structure as a function of the number of UCs. Comparison of the responses of Fig. 3.4 to those of Fig. 3.2(b) shows that the transmission poles were reduced to a level below -40 dB in the case of seven UCs and that the TCR CRLH TL filter has a symmetric and sharp rejection response with wide stopbands.

3.1.3 MIM Implementation of CRLH TLs

It has been recently shown that the interdigital capacitors used in the conventional CRLH structure suffer of spurious transverse resonances falling within its operating passband at relatively high frequencies (i.e. typically in the RH passband) [12]. The number of these resonances depends on the number of fingers forming the interdigital capacitors. In the BPF application, where low insertion loss is required through out the full CRLH passband, the existence of such spurious resonances cannot be tolerated. In order to mitigate this problem, in a context different than that of filters, a wire-bonded interdigital capacitor was proposed in [12]. However, wire bonds are well-known to be fragile and to introduce spurious inductances at higher frequencies, so that they should be avoided whenever possible. For this reason and also for the sake of compactness, a MIM capacitor implementation of the proposed TCR CRLH

Table 3.1 Circuit parameters of the CRLH TL structure of Figs. 3.1(a) and 3.2(a)

Symbol	Description	Value
C_L	series capacitor	0.375 pF
L_L	shunt inductor	0.938 nH
C_R	shunt capacitor	0.700 pF
L_R	series inductor	1.750 nH
C_c	coupling capacitor	0.040 pF
L_s	resonator shunt inductor	1.200 nH
C_s	resonator shunt capacitor	0.100 pF

TL is chosen here. In addition to compactness, the MIM capacitor presents the advantage of much higher simplicity in term of design compared to the interdigital capacitors. This is at the expense of an additional metal layer, but this difficulty can now be easily addressed with high-quality multilayer PCB process. Due to the fact that the MIM capacitor is completely immune from parasitic transverse resonances, it represents an excellent choice for the TCR CRLH BPF. In terms of size, it has been observed that the conventional CRLH structure based on MIM capacitors for a leaky-wave antenna application is around 1.8 times smaller than that based on interdigital capacitors presented in [50].

The layout of a CR CRLH UC is shown in Fig. 3.5. The equivalent circuit elements of the conventional CRLH UC (Fig. 3.2(a)) are formed by the MIM capacitor (LH capacitance C_L and parasitic RH inductance L_R), a shorted stub inductor (inductance L_L and parasitic capacitance C_R). The CR is constituted by a gap coupling capacitor (capacitance C_c) and a shorted stub resonator (anti-tank L_s and C_s). Ground vias short both the CRLH and the CR stubs to the ground plane.

In addition to the elimination of transverse resonance, clear and distinct advantages of MIM capacitor based CRLH TL architecture in comparison with the conventional CRLH TL are its inherent balanced and symmetrical characteristics. In conventional CRLH structure, the interdigital capacitors at the input and output must be re-designed to achieve twice the capacitance and half the inductance values comparing to the inner interdigital capacitors [4]. In contrast, these requirements are

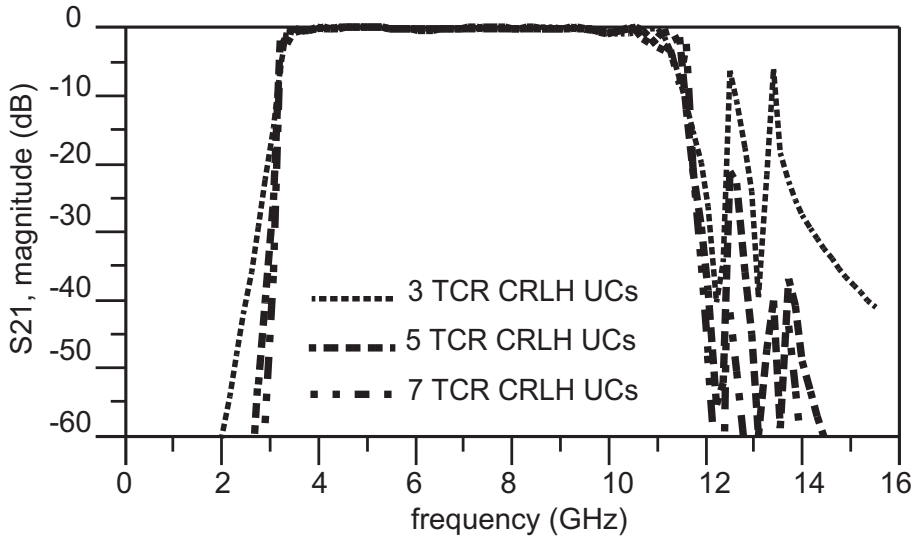

Figure 3.4 Transmission responses of TCR CRLH TL as a function of the number of cells.

automatically obtained in MIM CRLH TL, because the two inner MIM capacitors of adjacent UCs are connected in series, hence total capacitor is exactly a half and total inductor is twice those of the input and output capacitors.

The MIM series capacitor C_L and shunt inductor L_L are approximated as [42]

$$C_L = C_{MIM} = \varepsilon_0 \varepsilon_r \frac{w_2^2}{h_1}, \tag{3.13}$$

$$L_L \approx \frac{Z_s}{\omega} \tan(\beta \ell_s), \tag{3.14}$$

where Z_s is the characteristic impedance of the TL having a width w_s. The shunt capacitor C_R is the total parasitic capacitance to the ground which can be approximated as [51]

$$C_R \approx \varepsilon_0 \varepsilon_r \frac{w_s \ell_s + w_1 \ell}{h_1 + h_2}, \tag{3.15}$$

The series inductor L_R is formed mainly by a narrow TL section connected between two MIM capacitors. Such a step impedance inductor with discontinuity between w_2 and w_1 has an inductance value approximately given by [51].

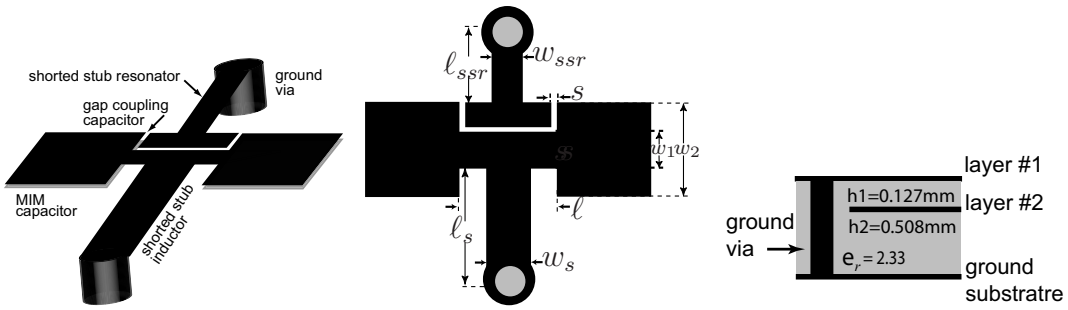

Figure 3.5 Metal-Insulator-Metal (MIM) implementation of a CR CRLH UC. (a) Perspective view. (b) Top view. (c) Side view.

$$L_R \approx \frac{Z_2\sqrt{\varepsilon}_{e2}\ell}{c} + 0.000987(h_1 + h_2)\left(1 - \frac{Z_2}{Z_1}\sqrt{\frac{\varepsilon_{e2}}{\varepsilon_{e1}}}\right) \tag{3.16}$$

The shunt inductance L_s and shunt capacitance C_s of the shorted stub CR can be approximated using (3.14) and (3.15) with appropriate parameter values. Due to the shape of the gap between the CRLH and the CR, the empirical formula for the coupling capacitance C_c can only be approximated to the first order as given in [52]. Therefore its value is extracted from full-wave simulation. Since equations (3.13-3.16) are approximations and provide only initial values of the layout dimensions, electromagnetic full-wave simulations and optimizations are required to fine-tune the structure into its optimal performance. Table 3.2 gives the dimensions of the fabricated TCR CRLH BPF for the values of its circuit parameters shown in Table 3.1.

3.1.4 Filter Demonstration

The fabricated TCR CRLH BPF consists of 7 UCs in a Duroid 5870 substrate with the dielectric constant of 2.33 and loss tangent (tanδ) of 0.0012 at 10 GHz. The substrate parameters are shown in Fig. 3.5(c). Fig. 3.6(a) shows the top (Layer 1) and bottom (Layer 2) metal layers of the same substrate, while Fig. 3.6(b) shows the complete implementation of the BPF. The dimensions of the overall BPF are 2.2 cm by 5.8 cm.

The TCR CRLH BPF is demonstrated by both simulation and measurement. In the former case, the circuit simulator Agilent ADS-Schematic and the electromag-

Table 3.2 Parameters of the TCR CRLH BPF structure. Definitions of the layout parameters are shown in Fig. 3.5

Symbol	Description	Value
w_2	width of MIM capacitor	2.134 mm
w_1	width of interconnect TL	0.762 mm
w_s	width of stub inductor	1.270 mm
l_s	length of stub inductor	2.667 mm
w_{ssr}	width of SSR	0.660 mm
l_{ssr}	length of first 3 SSRs (left to right)	2.54, 2.46, 2.41 mm
	length of the middle SSR	2.29 mm
	length of last 3 SSRs (left to right)	2.41, 2.46, 2.54 mm
s	coupling capacitor gap	0.152 mm
l	length of TL between MIM capacitors	2.54 mm

netic frequency-domain and time-domain simulators Agilent ADS-Momentum and CST-Microwave Studio, respectively, are used. In the latter case, the measurement is performed using an HP-8510C vector network analyzer. Figs. 3.7 present the simulation and measurement results. Fig. 3.7(a) shows the S-parameter responses. The measured -3 dB bandwidth extends from 3.28 to 12.2 GHz, which corresponds to a fractional bandwidth of 115%. The passband has insertion loss and ripple levels of 1dB and 1.5 dB, respectively. The presence of a dip in the S_{21} response from 5 to 6 GHz is explained by the unbalance of the CRLH structure induced by imperfections of the fabricated prototype, including mostly inaccuracy in the location and width of the thickness of the via holes. Stopband rejections are measured as the difference of attenuation levels between -3 dB cutoff frequency (f_{-3dB}) and $f_{-3dB\pm1\text{GHz}}$. The measured low-frequency stopband rejection is -115dB per 1 GHz offset and high-frequency stopband rejection is -38 dB per 1 GHz offset. The filter's group delay within the passband is shown in Fig. 3.7(b). Its measured value within the filter's passband is 0.7±0.2 ns.

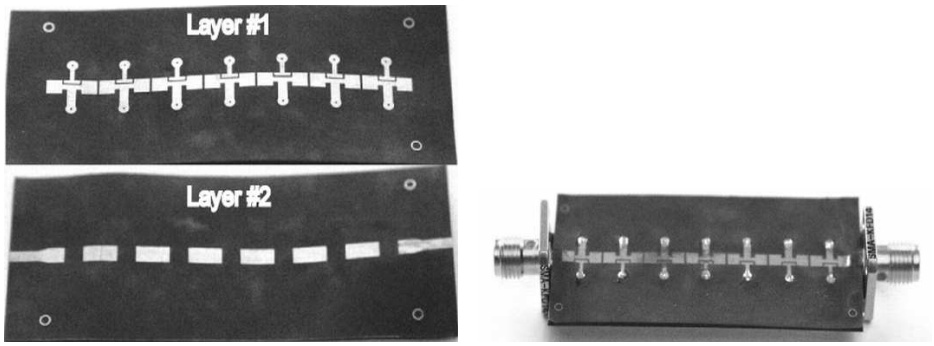

(a) (b)

Figure 3.6 CR CRLH BPF prototype. (a) Top two metal layers (same substrate). The length of the TCRs (layer 1) symmetrically varies along the structure (see Table 1), the differences are too small to be visible. (b) Assembled prototype with the ground plane substrate.

3.1.5 Comparison with an Equal-Ripple BPF

A conventional equal-ripple BPF having the same size and substrate material as the TCR CRLH BPF is designed and measured for comparison. In order to obtain the same physical size, a BPF is of the seventh-order ($N = 7$), with 0.5 dB equal-ripple comparable to the ripples of the TCR CRLH BPF and with a center frequency of 8 GHz. The BPF is designed using offset, broadside-coupled microstrip TL in a two-layer stripline configuration to achieve stronger coupling and broader bandwidth than what can be obtained using edge coupled microstrip TL, as depicted in Fig. 3.8(a) (where the direction of propagation is z). The striplines in layer 1 and layer 2 are etched on both sides of a Duroid 5870 0.127 mm substrate. Two Duroid 5870 substrates with thickness of 0.508 mm are placed at the top and at the bottom to form the required ground planes. Fig. 3.8(b) shows the equal-ripple BPF prototype. Its dimensions are 2 cm by 6 cm (comparable to the 2.2 cm by 5.8 cm of the TCR CRLH BPF of Fig. 3.6(b)).

Fig. 3.9 shows the simulated and measured responses of the equal-ripple BPF. The performances of this filter in compared with those of the TCR CRLH BPF are summarized in Table 2.

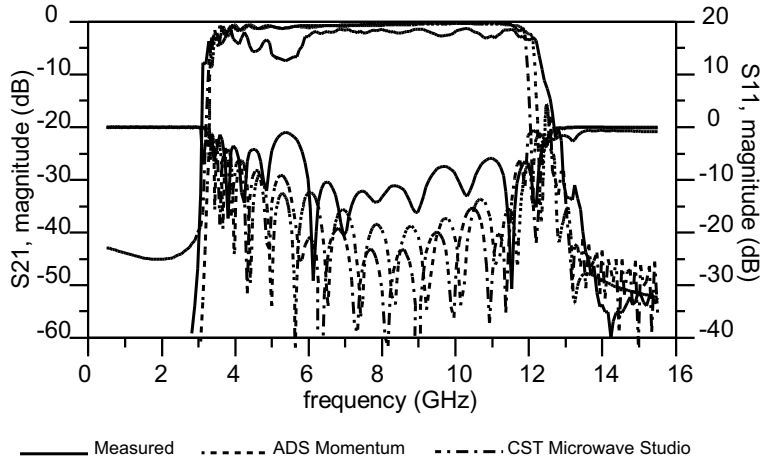

(a)

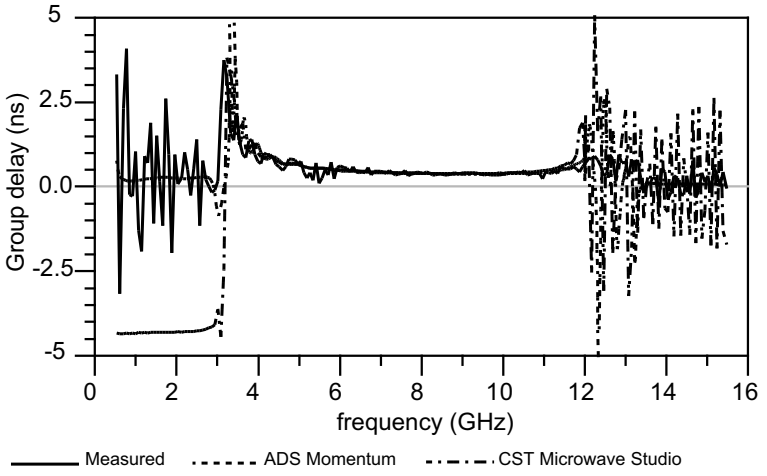

(b)

Figure 3.7 Simulated and measured results for the CR CRLH BPF. (a) S-parameters. (b) Group delay.

3.1.6 Conclusions

This work has demonstrated a highly selective BPF based on the CRLH TL and TCR concepts. CRLH TL filter design emphasizes primarily on the phase response instead of the amplitude response of the signal in its passband. As a result, the CRLH TL BPF is non-optimum in terms of passband ripple level and insertion loss. However, the essential properties of CRLH TL BPF are the ultra-wide bandwidth and sharp rejection in its stopbands. The high selectivity of the lower cutoff is due

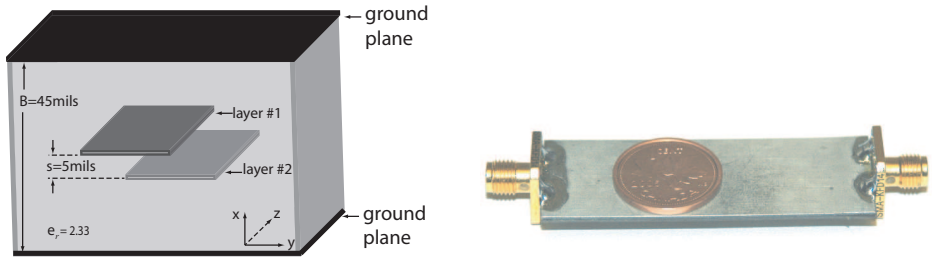

(a) (b)

Figure 3.8 Equal-ripple BPF. (a) Architecture of the multilayer stripline design. Only one cell is shown here, while the complete filter includes 7 cells. (b) Assembled prototype.

Table 3.3 Comparison of Measured Performances between the CR-CRLH and Conventional Equal-ripple BPFs

Symbol	CR-CRLH BPF	Equal-ripple BPF
Bandwidth	3.28-12.20 GHz	5.20-10.55 GHz
FBW	115%	68%
Low frequency selectivity	-115 dB/GHz	-36 dB/GHz
High frequency selectivity	-38 dB/GHz	-35 dB/GHz
Insertion loss	-1.5 dB	-1.0 dB
Return loss	less than -6.5 dB	less than -8.45 dB
Size	2.2 cm x 5.8 cm	2 cm x 6 cm

to the inherent slow-wave property of the CRLH structure in its LH range while the high selectivity of the higher cutoff is due to the attenuation poles introduced by the TCR.

The fabricated TCR CRLH BPF has a measured FBW in excess of 110% with the very sharp frequency stop bands of -115dB/GHz for the lower cutoff and -38dB/GHz for the higher cutoff. Comparison with a conventional equal-ripple filter of same size and same substrate with comparable insertion loss shows that the TCR CRLH BPF exhibits a 70% broader bandwidth. Alternatively, for a given selectivity, this TCR CRLH BPF would be considerably smaller. The TCR CRLH BPF is implemented in

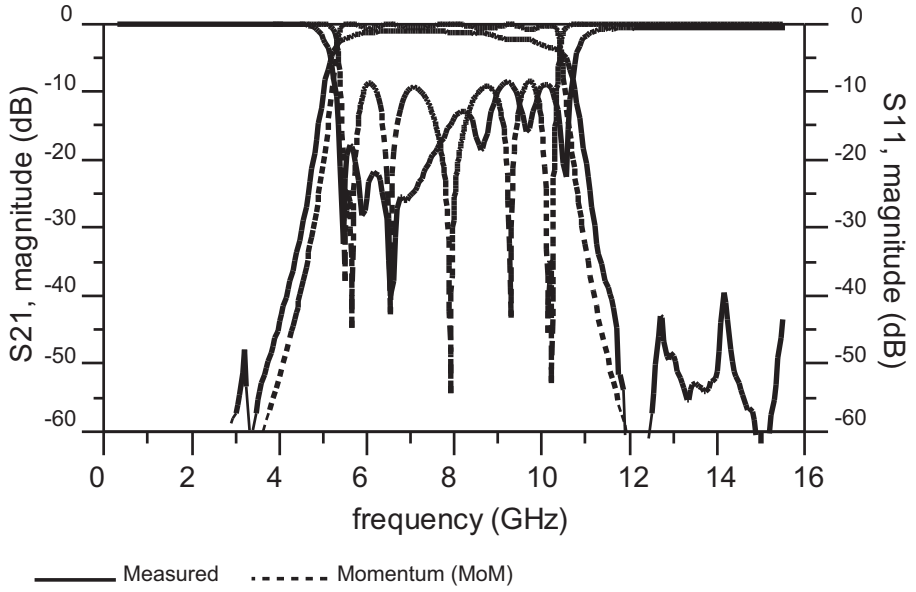

Figure 3.9 Simulated and measured results for the 0.5dB equal-ripple BPF.

a MIM configuration. This implementation has been shown to provide high compactness as well as symmetry and to suppress the spurious transverse resonances typically existing in the interdigital implementation of CRLH TLs.

The proposed TCR CRLH BPF represents a new filter design, which can potentially achieve broader arithmetic or geometric FBW up to the limit of 141% or 200%, respectively. Considering that the FBW allocated by the Federal Communications Commission for UWB systems is of 110% (3.1 to 10.6 GHz), the potential usefulness of this TCR CRLH BPF (which exhibits approximately the same bandwidth) for UWB applications is evident.

3.2 Article 2: Tunable Arbitrary N-port CRLH Infinite-wavelength Series Power Divider

Most conventional antenna array systems require a feeding network to distribute power from an input port to each array element or to combine power from all array elements to the input port [53]. There are essentially three existing types of feeding networks: the corporate feed, the series feed and the hybrid feed (combination of

corporate and series feeds). These feeding networks generally suffer of high loss, complex design, or magnitude/phase imbalance between the output ports. Recently, series feeding networks based on MTM TLs or waveguides have been proposed and demonstrated to provide magnitude and phase balance and to allow arbitrary spacing between the output ports [54], [55], [56]. However, these series power dividers are designed only for a fixed number of output ports.

This work proposes a new CRLH TL series power divider with an arbitrary and tunable number of output ports. This device operates at the CRLH infinite-wavelength frequency for equi-magnitude/phase power division and in the travelling-wave (as opposed to resonant) mode for frequency independence from the number of output ports. Due to the infinite-wavelength regime (operating at ω_0), the location of the output ports can be chosen arbitrarily. The proposed power divider is implemented in a shielded configuration and hence is immune to leaky-wave radiation loss. In addition, its input impedance can be tuned to accomodate an arbitrary number of output ports by using a simple inductor and varactor-based L matching network. By reciprocity, this divider may also be used as a combiner.

3.2.1 Principle of Operation

Fig. 3.10 shows the proposed divider. Due to the infinite-wavelength regime, the fields are perfectly uniform at $\omega = \omega_0$, both in magnitude and in phase, along the structure. Therefore, no phase shift occurs between the unit cells and the CRLH TL sections between the output ports are electromagnetically transparent. Thus, all of the output ports may be seen as if they were connected to a common potential point. If they have the same port admittance (Y_p), the power injected at the input of the divider will be distributed equally to each port, regardless of the number of unit cells (N) and of the number of output ports (P). The proposed divider is also operated in the traveling-wave mode (as opposed to resonance mode), and therefore its operation frequency is conveniently independent from both N and P.

From Fig. 3.10, the input admittance Y_{in} is hence the sum of the conductance G_p of the loads (the ports are considered to have a practical real admittance) connected to the P output ports and of the admittances G_s of the stubs of the CRLH N unit cells:

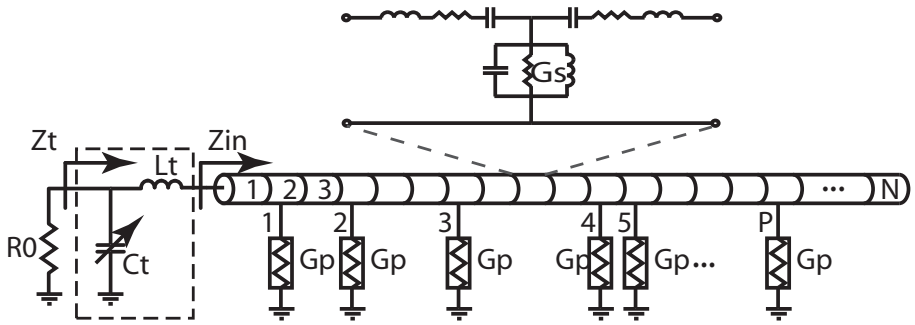

Figure 3.10 Arbitrary N-port CRLH series feeding network with a tunable input matching.

$$Y_{in} = PG_p + NG_s = \frac{1}{Z_{in}} \tag{3.17}$$

This result reveals that the input impedance depends on the number of ports P for a structure with a given number of unit cells N. This dependence may be removed by introducing an L-matching circuit composed of a series inductor L_t and a shunt varactor C_t [57], as shown in Fig. 3.10. The input impedance (Z_{in}) of the series power divider is then transformed to the termination impedance Z_t

$$Z_t = \frac{1}{j\omega C_t}||(j\omega L_t + Z_{in}) = \frac{Z_{in} + j\omega L_t}{1 - (\omega/\omega_t)^2 + j\omega Z_{in} C_t} \approx \frac{L_t}{Z_{in} C_t}, \tag{3.18}$$

where the approximation is justified by the facts that the matching network is designed so as to have its resonance frequency ($\omega \approx \omega_t = 1/\sqrt{L_t C_t}$) coinciding with the operation frequency of the divider and that it is assumed to have a high quality factor $Q = \omega_t L_t / Z_{in} \gg 1$. By combining (3.17) and (3.18), it is found that the varactor can then be tuned, as a function of N and P (possibly varying in real-time) for matching to an input port of resistance R_0 ($Z_t = R_0$), following the formula

$$C_t(P, N) = \frac{L_t}{R_0 Z_{in}} = \frac{L_t(PG_p + NG_s)}{R_0}. \tag{3.19}$$

The required capacitance range of the varactor diode is obtained by taking the derivative of (3.19) with respect to P and N,

$$\triangle C_t = \frac{\partial C_t}{\partial P}\triangle P + \frac{\partial C_t}{\partial N}\triangle N. \tag{3.20}$$

In practice, only the number of output ports P would be likely varied (for instance by employing switches), and the variation of C_t with respect to P is then simply given by $\triangle C_t/\triangle P = L_t G_p/R_0$. For example, for $L_t = 0.8$ nH, $G_p = 0.02$ S and $R_0 = 50$, a variation of $\triangle P = 5$ in the number of output ports requires a variation of 1.6 pF for C_t. Fig. 3.11 illustrates the variation of Z_{in} and C_t versus P.

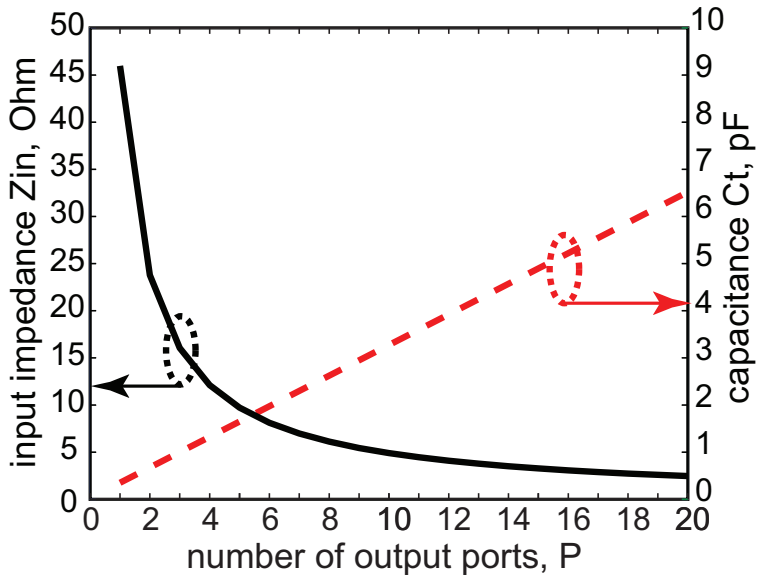

Figure 3.11 Variation of input impedance Z_{in} and required varactor diode capacitance C_t against number of output ports P, computed by 3.17 and 3.19, respectively, for L_t =0.8 nH, G_p =0.02 S, and $R_0 = 50$.

3.2.2 Implementation and Experimental Results

It is well established that a CRLH TL operating at its infinite-wavelength frequency exhibits leaky-wave radiation when the structure is open to free space [4]. In order to eliminate the radiation loss, the proposed CRLH TL divider is implemented in a shielded (closed) [58] MIM configuration with four metal layers. The input matching microstrip network (open structure) is implemented on a separate board for fabrication simplicity. Fig. 3.12 shows the open and closed views of the experimental prototype with a close-up view of the CRLH unit cell MIM structure in the inset.

Fig. 3.13 presents the full-wave simulated and measured results. Figs. 3.13(a) and 3.13(b) show the magnitude and phase of S_{10}, S_{40}, and S_{50} (arbitrarily chosen

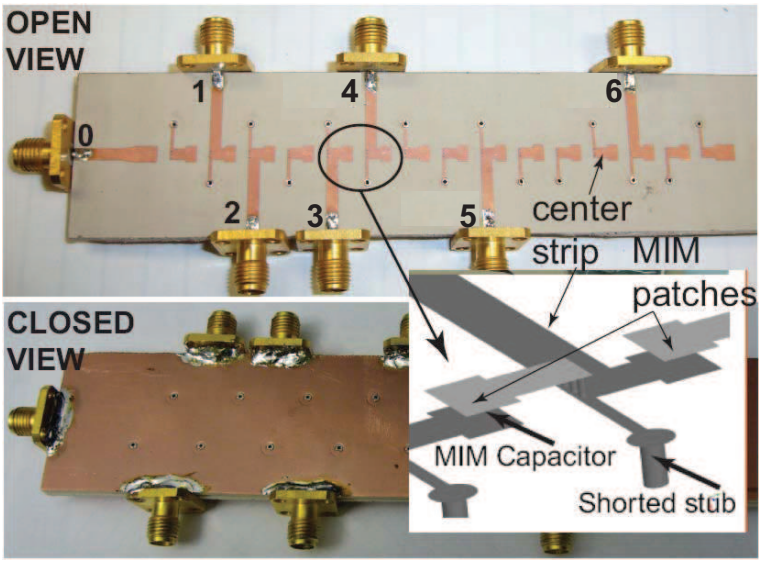

Figure 3.12 Experimental prototype (with six ports) in shielded stripline configuration.

output ports) with all 6 output ports connected. The higher insertion losses seen in the MoM full-wave results are probably due to the excitation of spurious parallel-plate modes in the infinitely extended ground plane. Fig. 3.13(c) shows the input return loss S_{00} (only ports 2, 5, and 6 are connected and other ports are left open) and the power difference between these three ports. Good matching is maintained by tuning the varactor, when the number of output ports is changed.

3.2.3 Conclusions

An arbitrary N-port series power divider utilizing the infinite-wavelength characteristic of CRLH TLs has been presented and shown to exhibit magnitude/phase balance at all of its output ports. In addition, the proposed series power divider can be dynamically adjusted using a tunable input matching network comprised of a series inductor and a shunt varactor diode to accommodate an arbitrary number of output ports in addition to arbitrary spacings. Compared to conventional series power dividers, the proposed series power divider offers in addition to an arbitrary number of output ports, the following advantages: 1) simple and compact design, 2) tunable input matching, and 3) arbitrary spacing between output ports. The proposed series power divider may find various applications in beam-forming phased-array antenna

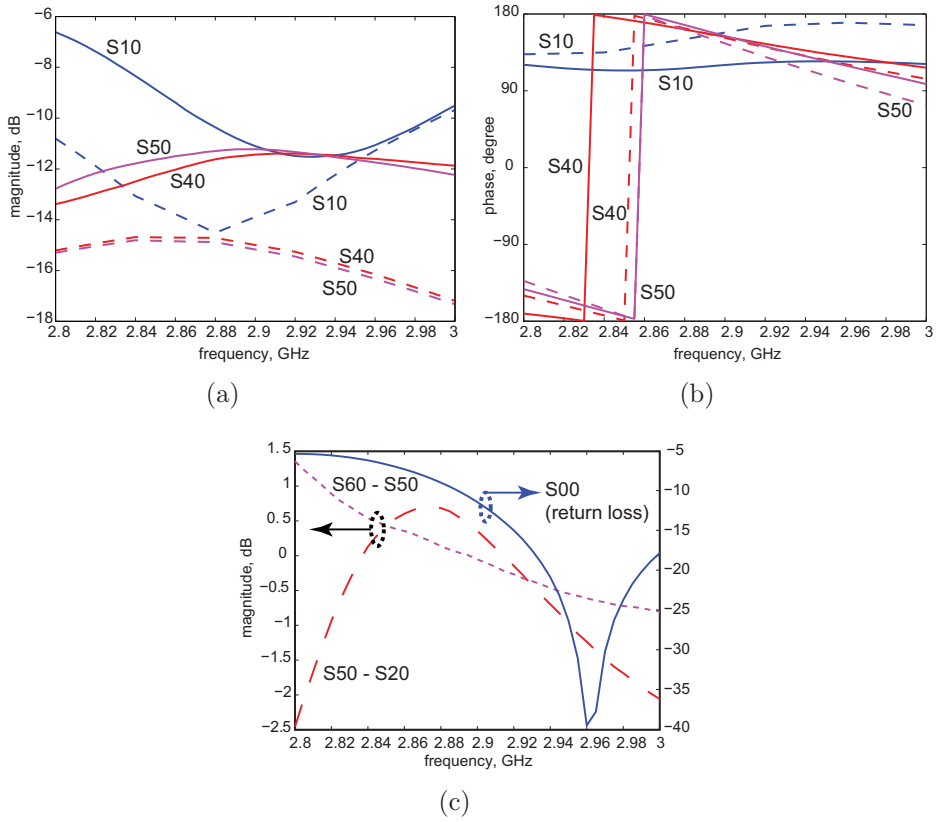

Figure 3.13 Scattering parameter for infinite-wavelength power divider of Fig. 3.16 designed at frequency of 2.88 GHz. a) Full-wave (dashed) and measured (solid) results with all six output ports connected ($C_t = 2$ pF with $L_t = 0.8$ nH). b) Idem for phase. c) Measured results when only ports 2, 5, and 6 are connected, while other ports left open ($C_t = 1$ pF with $L_t = 0.8$ nH).

and power dividing/combining.

3.3 Article 3: Generalized Coupled-mode Approach of Metamaterial Coupled-line Couplers: Coupling Theory, Phenomenological Explanation, and Experimental Demonstration

A coupled-line coupler is a four-port network constituted of the juxtaposition of two unshielded TLs exchanging power between each other in ratios that can be controlled with design parameters such as the interspacing between the two lines and the length of the overall structure [49], [51], [52]. While branch-line type couplers have all their ports interconnected physically by TL sections and are based on multi-path interference mechanisms, coupled-line type couplers have no connection between the ports located on either side of each line and are based on more complex coupling phenomena. Coupled-line couplers have the advantage of providing much broader bandwidth (typically more than 25%) than branch-line couplers (typically less than 10%). However, they are generally restricted to weak coupling levels (typically less than 10 dB) in uniplanar edge-coupled configurations (e.g. microstrip TL or coplanar waveguide). In broadside-coupled configurations (e.g. stripline), strong coupling levels can be achieved, but the structure is non-uniplanar and requires at least four metal layers. Lange-type couplers can combine the benefits of broad bandwidth and strong coupling, at the expense of requiring cumbersome and parasitic-prone bonding wires [52].

CRLH TL MTM structures [4] have lead to novel coupled-line couplers with unprecedented characteristics [13],[14], [59], [60], [8] such as arbitrary coupling level in addition to the broad bandwidth of conventional coupled-line couplers. To date, two different types of couplers employing MTM TLs have been reported. The first type is constituted of two identical CRLH TLs operated in their LH frequency range as illustrated in Fig. 3.14(c) [14], [8]; the second type includes one conventional RH and one CRLH TLs as illustrated in Fig. 3.14(d) [13], [59]. CRLH - CRLH couplers have been rigorously analyzed and synthesized by the even/odd mode decomposition technique in [4], [14], [8]. In contrast, RH - CRLH couplers, which cannot be described by even/odd mode decomposition due to their asymmetric nature, have been studied from a more speculative prospect [13], [60]; for this type of coupler, a rigorous theory for the complete understanding and efficient design over the full coupling bandwidth

is still lacking.

This section fills this gap and presents a generalized coupled-mode approach of coupled-line couplers [61], [62], [63], which is valid for any type of coupled-line couplers and equally applicable to both the conventional and CRLH metamaterial couplers. As further derived in the next section, this theory is developed in the most general case of a coupler constituted of two CRLH TLs, and then particularized to the cases of the CRLH - CRLH and RH - CRLH. Closed form expressions for both the complex propagation constants and scattering parameters are provided. In addition, simplified formulas based on a quasi-TEM approximation (exact in the perfectly TEM limit) are also developed for contra-directional couplers, which are the most common types in microwaves. Both types of couplers, implemented in a MIM capacitor based CRLH TL configuration, are demonstrated experimentally in comparison with theoretical predictions.

This section is organized as follows. Subsection 3.3.1 presents the CRLH generalized coupled-mode theory while subsection 3.3.2 develops a quasi-TEM approximation (exact for TEM structures) of the coupled-mode theory, which provides both simplified formulas for practical contra-directional couplers and straightforward insight into coupling phenomena. The coupled-mode theory is demonstrated experimentally and compared to circuit simulation predictions in subsection 3.3.3 for three different types of couplers. Finally, conclusions and perspectives are given in subsection 3.3.4.

3.3.1 CRLH-Generalized Coupled-Mode Theory

Fig. 3.14 represents the different existing types of conventional and metamaterial, symmetric and asymmetric, coupled-line couplers. All of them can be analyzed with the generalized coupled-mode theory which is presented in this section.

Fig. 3.15 shows a coupled-line coupler constituted of the generalized CRLH TLs [4]. Fig. 3.15(a) shows the forward (propagating in the $+z$ direction) and backward (propagating in the $-z$ direction) *coupled-mode* waves used in the coupled-mode theory, $a_n^{\pm}$, where the subscript n ($n = 1, 2$) indicates the line considered and the superscript $\pm$ denotes forward ($+$) or backward ($-$) wave propagation [62], [63]. Fig. 3.15(b) shows the equivalent circuit for the coupled-line structure, where L_{Rn}, L_{Ln} are the RH $-$ LH self-inductances and C_{Rn}, C_{Ln} are the RH $-$ LH self-capacitances per unit length of line n in the presence of other line, and where magnetic and electric

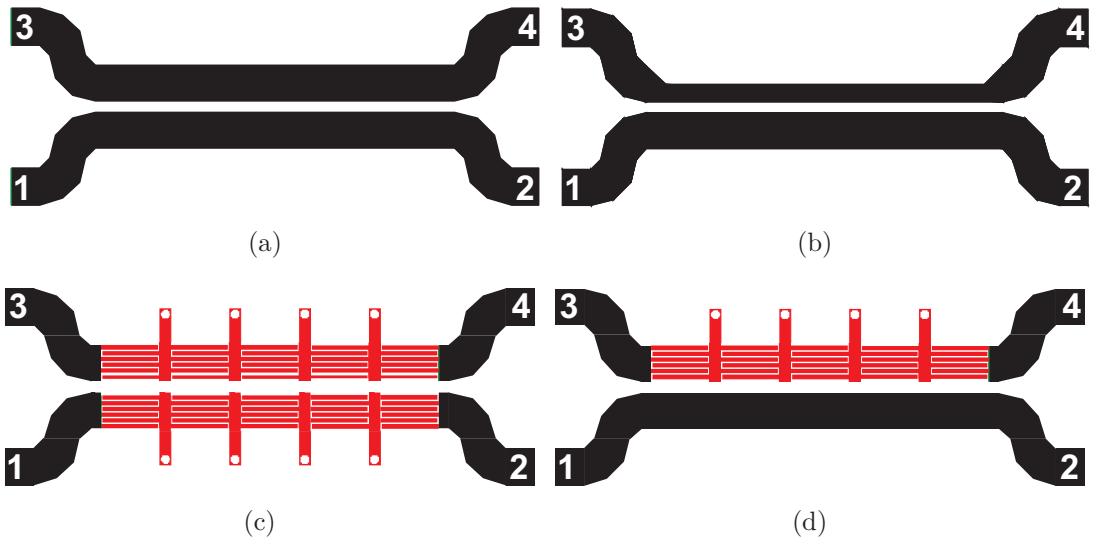

Figure 3.14 Different possible types of coupled-line couplers. a) RH (conventional) symmetric (two identical RH lines). b) RH asymmetric (two different RH lines). c) CRLH symmetric or asymmetric (two identical or different CRLH lines). d) RH - CRLH line asymmetric (one RH line and one CRLH line).

coupling between the two lines are represented by L_m and C_e, respectively.

The CRLH coupled-line coupler shown in Fig. 3.15 is the most general coupled-line configuration because its CRLH-based TL can represent any physical TL structure. Therefore, any kind of coupled-line coupler (Fig. 3.14) can be described with this generalization with the particular configurations shown in Tab. 3.4. Formally, couplers including purely LH TLs ($L_R = C_R = 0$) can also be handled by the model of Fig. 3.15(b); however, it is known that such structures cannot be realized physically due to parasitic [4] and are therefore not considered per se.

The Kirchhoff's voltage and current laws for the circuit of Fig. 3.15(b) in harmonic regime with the time dependence convention $e^{j\omega t}$ constitute the following system of first-order *coupled* differential equations

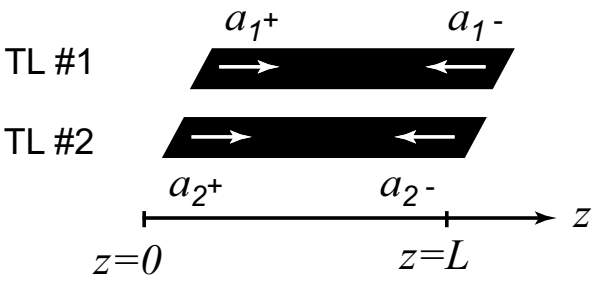

(a)

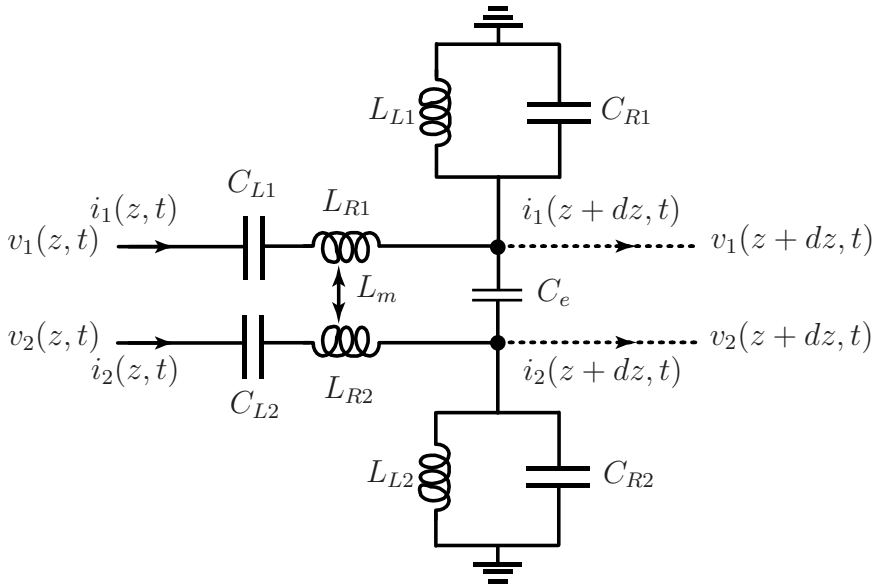

(b)

Figure 3.15 Generalized CRLH line coupled-line coupler representing any of the possible coupler types shown in Fig. 3.14. (a) Generic representation with forward and backward coupled-mode waves on each line. (b) Infinitesimal CRLH equivalent circuit.

$$\frac{\partial V_1}{\partial z} + j\omega\left(L_{R1} + \frac{1}{\omega^2 C_{L1}}\right) I_1 + j\omega I_2 L_m = 0 \tag{3.21a}$$

$$\frac{\partial I_1}{\partial z} + j\omega\left(C_{R1} + \frac{1}{\omega^2 L_{L1}}\right) V_1 + j\omega V_2 C_e = 0 \tag{3.21b}$$

$$\frac{\partial V_2}{\partial z} + j\omega\left(L_{R2} + \frac{1}{\omega^2 C_{L2}}\right) I_2 + j\omega I_1 L_m = 0 \tag{3.21c}$$

$$\frac{\partial I_2}{\partial z} + j\omega\left(C_{R2} + \frac{1}{\omega^2 L_{L2}}\right) V_2 + j\omega V_1 C_e = 0 \tag{3.21d}$$

Table 3.4 Different Coupler Types as a Function of the LC Parameters in the General Model of Fig. 3.15(b). (The crosses indicate finite nonzero values.)

	L_{R1}/C_{R1}	L_{L1}/C_{L1}	L_{R2}/C_{R2}	L_{L2}/C_{L2}
RH-RH (Fig. 3.14(a) and 3.14(b)	x	∞/∞	x	∞/∞
CRLH-CRLH (Fig. 3.14(c)	x	x	x	x
CRLH-RH (Fig. 3.14(d)	x	x	x	∞/∞

In essence, the coupled-mode solution is an extension of the solution to the uncoupled system, taking into account coupling. Let us therefore consider first the uncoupled system. In the absence of coupling ($L_m = C_e$ =0), (3.21a)-(3.21d) reduce to the telegrapher's equations, whose solutions are

$$V_n(z) = V_n^+ e^{-j\beta_{CRLH_n} z} + V_n^- e^{+j\beta_{CRLH_n} z} \tag{3.22a}$$

$$I_n(z) = \frac{V_n^+}{Z_n} e^{-j\beta_{CRLH_n} z} - \frac{V_n^-}{Z_n} e^{+j\beta_{CRLH_n} z} \tag{3.22b}$$

where

$$\beta_{CRLH_n} = \omega\sqrt{L_{Rn}^{iso} C_{Rn}^{iso}} - \frac{1}{\omega\sqrt{L_{Ln}^{iso} C_{Ln}^{iso}}} \tag{3.22c}$$

and

$$Z_n = \sqrt{\frac{L_{Rn}^{iso}}{C_{Rn}^{iso}}} = \sqrt{\frac{L_{Ln}^{iso}}{C_{Ln}^{iso}}} \tag{3.22d}$$

are the propagation constants and characteristic impedance of each *isolated* CRLH. The isolated self-inductance $L_{Rn/Ln}^{iso}$ and self-capacitance $C_{Rn/Ln}^{iso}$ can be approximated to the coupled-structure self-inductance and capacitance as

$$L_{Rn/Ln}^{iso} = L_{Rn/Ln} + L_m \tag{3.23a}$$

$$C_{Rn/Ln}^{iso} = C_{Rn/Ln} + C_e. \tag{3.23b}$$

Adding and subtracting (3.22a) and (3.22b) multiplied by Z_n yields the normalized

forward and backward waves

$$a_n^{\pm}(z) = \frac{1}{2\sqrt{Z_n}}[V_n(z) \pm Z_n I_n(z)] = \frac{1}{\sqrt{Z_n}} V_n^{\pm} e^{\mp j\beta_{CRLHn} z}. \tag{3.24}$$

Inverting this relation provides the following alternative expression to (3.22a) and (3.22b) for the voltage and current

$$V_n(z) = \sqrt{Z_n}[a_n^+(z) + a_n^-(z)], \tag{3.25a}$$

$$I_n(z) = \frac{1}{\sqrt{Z_n}}[a_n^+(z) + a_n^-(z)]. \tag{3.25b}$$

Equation (3.25) can now be inserted into system (3.21a)-(3.21d) to account for coupling. This leads, after some algebraic manipulations, to the following linear system of equations:

$$\frac{\partial a_1^+}{\partial z} = -j\beta_{CRLH1} a_1^+ - jK_{FW} a_2^+ + jK_{BW} a_2^- \tag{3.26a}$$

$$\frac{\partial a_1^-}{\partial z} = +j\beta_{CRLH1} a_1^- - jK_{BW} a_2^+ + jK_{FW} a_2^- \tag{3.26b}$$

$$\frac{\partial a_2^+}{\partial z} = -j\beta_{CRLH1} a_2^+ - jK_{FW} a_1^+ + jK_{BW} a_1^- \tag{3.26c}$$

$$\frac{\partial a_2^-}{\partial z} = +j\beta_{CRLH1} a_2^- - jK_{BW} a_1^+ + jK_{FW} a_1^- \tag{3.26d}$$

where

$$K_{FW} = \sqrt{\beta_{RH1}\beta_{RH2}\left(\frac{k_m - k_e}{2}\right)} \tag{3.26e}$$

$$K_{BW} = \sqrt{\beta_{RH1}\beta_{RH2}\left(\frac{k_m + k_e}{2}\right)} \tag{3.26f}$$

with

$$k_m = \frac{L_m}{\sqrt{L_{R1}L_{R2}}}, \quad k_e = \frac{C_e}{\sqrt{C_{R1}C_{R2}}} \tag{3.26g}$$

$$\beta_{RHn} = \omega\sqrt{L_{Rn}C_{Rn}} \tag{3.26h}$$

where k_m and k_e are defined as the magnetic and electric coupling coefficients, respectively, and K_{FW} and K_{BW} are defined as the forward and backward coupling coefficients in reference to (3.26) and Fig. 3.15(a), respectively.

The coupled-mode characteristic impedances are obtained from the characteristic impedances of the isolated lines with Eqs. (3.23a) and (3.23b) as

$$Z_n = \sqrt{\frac{L^{iso}_{Rn/Ln} - L_m}{C^{iso}_{Rn/Ln} + C_e}} \tag{3.27}$$

Although this expression has been cancelled after insertion of (3.25) into (3.21), as seen in (3.26), it represents the coupled impedances of each line (Z_1 for line 1 and Z_2 for line 2) in the presence of other line and therefore are the impedances to be considered for exact matching of the coupled-line structure.

The coupled-mode system (3.26) may be interpreted as follows. In the absence of coupling ($k_m = k_e = 0$), each forward or backward wave is coupled only to itself, and the four equations (3.26a)-(3.26d) reduce to the wave equations of two isolated CRLH TLs with propagation constant β_{CRLHn} of (3.22). If coupling is present, then the waves are coupled to each other via the general form of (3.26). The two following cases are of particular interest. If $k_m = k_e \neq 0$, the wave incident at port 1 of line 1 is coupled only to the wave of the opposite direction on line 2; consequently, only backward-wave coupling is produced and the resulting coupler is termed contra-directional. If $k_m = -k_e \neq 0$, the wave incident at each port is coupled only to the wave of the same direction in the other line; consequently, only forward-wave coupling is produced and the resulting coupler is termed co-directional [61], [63]. In the most general case where $|k_m| \neq |k_e|$, the incident wave is coupled to all the other waves; depending on whether the ratio k_m/k_e is closer to $+1$ or to -1, we have a contra-directional or a co-directional coupler with imperfect isolation.

Let us now solve the system of equations (3.26a)-(3.26d) in order to determine the coupled forward and backward waves $a_n^{\pm}(z)$ as well as the subsequent scattering parameters for the coupler. For this purpose, we assume general solutions of the form

$$a_n^{\pm}(z) = A_0 e^{j\beta z} \tag{3.28}$$

where β represents the coupled complex propagation constant to be determined. Although the coupled-mode approach can straightforwardly handle non-uniform lines, we will restrict the analysis here, for simplicity, to the case of uniform lines, where the transmission parameters (propagation constant β and characteristic impedance

Z_c) do not vary with the position z. By substituting the waveform of (3.28) into (3.26a)-(3.26d), we obtain the following homogenous matrix equation

$$\begin{bmatrix} \beta+\beta_{CRLH1} & 0 & K_{FW} & -K_{BW} \\ 0 & \beta-\beta_{CRLH1} & K_{BW} & -K_{FW} \\ K_{FW} & -K_{BW} & \beta+\beta_{CRLH2} & 0 \\ K_{BW} & -K_{FW} & 0 & \beta-\beta_{CRLH2} \end{bmatrix} \begin{bmatrix} a_1^+(z) \\ a_1^-(z) \\ a_2^+(z) \\ a_2^-(z) \end{bmatrix} = \begin{bmatrix} 0 \\ 0 \\ 0 \\ 0 \end{bmatrix} \tag{3.29}$$

which admits a non-trivial solution only if the determinant of the matrix vanishes. Setting this determinant to zero yields a biquadratic equation in β which has the solutions

$$\beta_{I,II}^2 = \left(K_{FW}^2 - K_{BW}^2 + \frac{\beta_{CRLH1}^2 + \beta_{CRLH2}^2}{2} \right) \pm \sqrt{\left(\frac{\beta_{CRLH1}^2 - \beta_{CRLH2}^2}{2} \right)^2 - K_{BW}^2(\beta_{CRLH1} - \beta_{CRLH2})^2 + K_{FW}^2(\beta_{CRLH1} + \beta_{CRLH2})^2} \tag{3.30a}$$

The general forward and backward wave solutions of (3.28) can now be written explicitly in terms of superposition of the waves with the propagation constants found in (3.30) and their unknown amplitude coefficients can be determined by the application of appropriate boundary conditions, as done in Appendix A. The explicit $a_n^{\pm}(z)$ solutions are given by (A.1)-(A.2). The scattering parameters are then obtained from their definitions as

$$S_{11} = \frac{a_1^-(z=0)}{a_1^+(z=0)} = C + D \tag{3.31a}$$

$$S_{21} = \frac{a_1^+(z=L)}{a_1^+(z=0)} = Ae^{-j\beta_I L} + Be^{-j\beta_{II} L} \tag{3.31b}$$

$$S_{31} = \frac{a_2^-(z=0)}{a_1^+(z=0)} = \frac{X \cdot K_{BW} + Y \cdot K_{FW}}{K_{BW}^2 - K_{FW}^2}|_{z=0} \tag{3.31c}$$

$$S_{41} = \frac{a_2^+(z=L)}{a_1^+(z=0)} = \frac{X \cdot K_{FW} + Y \cdot K_{BW}}{K_{BW}^2 - K_{FW}^2}|_{z=L} \tag{3.31d}$$

where X and Y are given by (A.2c) and (A.2c), respectively, and A, B, C, and D are given by (A.4). It is important to note that (3.31) assume that all ports are matched, which is a reasonable assumption in practice. If this was not assumed,

multiple reflections would occur and result in more complicated expressions.

3.3.2 Quasi-TEM Contra-Directional Approximation

Most planar microstrip microwave couplers are quasi-TEM, which result into contra-directional couplers [61]. In the case of a quasi-TEM symmetric coupler, it may be shown [52] that the magnetic and electric coupling coefficients are approximately equal, $k_m \approx k_e$ (e.g. microstrip), where the approximation becomes an equality in the TEM case (e.g. stripline). Under this condition, the forward and backward coupling coefficients (3.26e) and (3.26f) reduce to

$$K_{FW} = \sqrt{\beta_{RH1}\beta_{RH2}}\left(\frac{k_m - k_e}{2}\right) \approx 0 \tag{3.32a}$$

$$K_{BW} = \sqrt{\beta_{RH1}\beta_{RH2}}\left(\frac{k_m + k_e}{2}\right) \tag{3.32b}$$

which shows with (3.26a)-(3.26d) that the forward wave couples only to the backward wave and vice versa. Substituting (3.32) into (3.26) and assuming that the excitation is applied at port 1, we obtain the reduced linear equations

$$\frac{\partial a_1^+}{\partial z} = -j\beta_{CRLH1}a_1^+ + K_{BW}a_2^- \tag{3.33a}$$

$$\frac{\partial a_2^-}{\partial z} = +j\beta_{CRLH2}a_2^- - jK_{BW}a_1^+ \tag{3.33b}$$

Inserting (3.28) into this system leads to the matrix equation

$$\begin{bmatrix} \beta + \beta_{CRLH1} & -K_{BW} \\ K_{BW} & \beta - \beta_{CRLH2} \end{bmatrix} \begin{bmatrix} a_1^+(z) \\ a_2^-(z) \end{bmatrix} = \begin{bmatrix} 0 \\ 0 \end{bmatrix} \tag{3.34}$$

By setting the determinant of this matrix to zero yields the coupled propagation constant solution

$$\beta_{I,II} = \beta_d \pm \beta_r \tag{3.35a}$$

where

$$\beta_d = \frac{|\beta_{CRLH1} - \beta_{CRLH2}|}{2} \tag{3.35b}$$

and

$$\beta_r = \sqrt{\beta_a^2 - K_{BW}^2} \tag{3.35c}$$

$$\beta_a = \frac{\beta_{CRLH1} + \beta_{CRLH2}}{2} \tag{3.35d}$$

The propagation constants of the three couplers analyzed in this work correspond to the following three cases.

Case 1: RH-RH coupler (refer to Fig. 3.14(a))

In this case, $\beta_{CRLH1} = \beta_{CRLH2} = \beta_{RH}$ and therefore, β_d =0 so that $\beta_{I,II} = \pm\sqrt{\beta_{RH}^2 - K_{BW}^2} = \pm\beta_{RH}\sqrt{1 - [(k_m + k_e)/2)]^2}$. This corresponds to two purely real solutions since the coupling coefficients k_m and k_e are always smaller than unity.

Case 2: CRLH-CRLH coupler (refer to Fig. 3.14(c))

In this case, from $\beta_{CRLH} = \beta_{RH} + \beta_{LH}$, where $\beta_{RH} = \omega\sqrt{L_R C_R}$ and $\beta_{LH} = -1/\omega\sqrt{L_L C_L}$, we have $\beta_{I,II} = \pm\sqrt{(\beta_{RH} + \beta_{LH})^2 - \beta_{RH}^2\,[(k_m + k_e)/2]^2}$, which for a given coupler can be either purely real or purely imaginary depending on frequency.

Case 3: RH-CRLH coupler (refer to Fig. 3.14(d))

In this case, $\beta_{CRLH1} = \beta_{RH1}$; therefore $\beta_d = (\beta_{RH1} - \beta_{CRLH2})/2 \neq 0$, and the propagation constants $\beta_{I,II}$ are either real or complex in the frequency ranges where β_r is purely real or purely imaginary, respectively.

These three cases will be illustrated in subsection 3.3.3 with the experimental demonstration of corresponding prototypes. As in the general case presented in subsection 3.3.1, the general forward and backward wave solutions in (3.28) can be written explicitly in terms of superposition of the waves with the propagation constants found, here (3.35), and their unknown amplitude coefficients can be determined by the application of appropriate boundary conditions. This is shown in Appendix B

and the explicit $a_n^{\pm}(z)$ solutions are given by (B.1)-(B.2). The scattering parameters are then obtained from their definitions as

$$S_{11} = \frac{a_1^-(z=0)}{a_1^+(z=0)} = 0 \tag{3.36a}$$

$$S_{21} = \frac{a_1^+(z=L)}{a_1^+(z=0)} = \frac{2\beta_r e^{-j(\beta_d-\beta_r)L}}{\beta_r\left(1+e^{j2\beta_r L}\right)-\beta_a\left(1-e^{j2\beta_r L}\right)} \tag{3.36b}$$

$$S_{31} = \frac{a_2^-(z=0)}{a_1^+(z=0)} = K_{BW}\frac{\left(1-e^{j2\beta_r L}\right)}{\beta_r\left(1+e^{j2\beta_r L}\right)-\beta_a\left(1-e^{j2\beta_r L}\right)} \tag{3.36c}$$

$$S_{41} = \frac{a_2^+(z=L)}{a_1^+(z=0)} = 0 \tag{3.36d}$$

These expressions are considerably simpler than those given for the general coupled-mode theory of subsection 3.3.1 in (3.31) and are therefore very convenient for contra-directional couplers. They are exact for TEM symmetric couplers and approximate but practically satisfactory for quasi-TEM symmetric couplers. Since $S_{41} = 0$, due to the assumption $k_m = k_e$, finite isolation in non-perfectly TEM couplers cannot be predicted, but the through and coupled parameters, S_{21} and S_{31}, respectively, are predicted accurately. In the case of co-directional couplers, where the coupled and isolated ports are 4 and 3, respectively, the general solutions of subsection 3.3.1 must be used. Dual approximate solutions corresponding to the assumption of $k_m = -k_e$, or $K_{BW} = 0$ according to (3.26f), could also be developed, but this is not done here due to the rarity of co-directional coupled-line couplers in microwaves.

3.3.3 Experimental Demonstrations

The following demonstrations present experimental results for the generalized coupled-mode theory discussed in the previous sections. For this purpose, we consider a RH − RH symmetric coupler (Fig.3.14(a)), a CRLH − CRLH symmetric coupler (Fig.3.14(c)) and a RH − CRLH asymmetric coupler (Fig.3.14(d)), whose prototypes are shown in Figs.3.16(a), 3.16(b), and 3.16(c), respectively. The asymmetric RH−RH coupler (Fig. 3.14(b)) is not considered explicitly as it may be considered as a particular (and simplified) case of the RH−CRLH one. The three couplers considered are essentially contra-directional. All three prototypes are designed using the Agilent ADS Momentum MoM commercial software. The Momentum results have

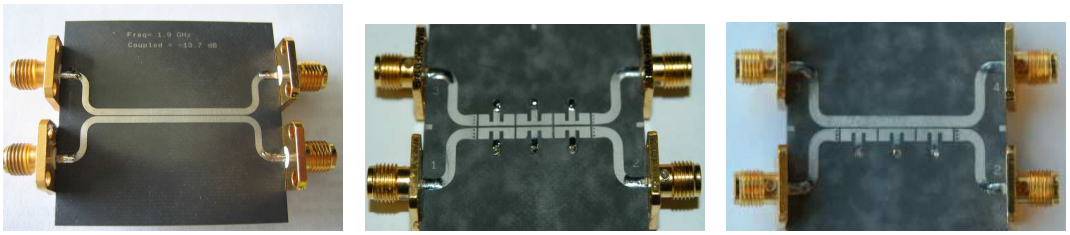

(a) (b) (c)

Figure 3.16 3-dB coupled-line coupler prototypes used for the validation of the generalized coupled-mode theory. a) RH - RH, b) CRLH-CRLH line [8], c) RH - CRLH.

shown very close agreement with measurements in all testing prototypes. Therefore Momentum results are not reported since they provide little information beyond measurements. Instead, comparison with the more informative, fast and insightful, ideal circuit model of Fig. 3.15(b) is provided.

RH-RH Coupler (Case #1)

Fig. 3.16(a) shows the RH − RH coupled-line coupler prototype. Since this coupler is quasi-TEM, it may be analyzed by the quasi-TEM approximation of coupled-mode theory developed in subsection 3.3.2. Here, we have β_d =0, $\beta_{CRLH} = \beta_{RH}$, and $\beta_r = \beta_{RH}\sqrt{1-k^2}$ with $k = (k_m + k_e)/2$. The purely real forward and backward propagation constants are shown in Fig. 3.17 along with the propagation constants of each line in the presence of the other one. The coupled propagation constants are slightly smaller than those of the isolated lines due to the presence of coupling since, from the above, $\beta_{I,II} = \pm\beta_r = \pm\beta_{RH}\sqrt{1-k^2}$. These propagation constants can be shown to be equivalent to the well-known even and odd mode propagation constants [51], where the assumption $k_m \approx k_e$ is typically made.

The expressions for the through and coupled scattering parameters can here be simplified from (3.36) to yield

$$S_{21} = \frac{\sqrt{1-k^2}}{\sqrt{1-k^2}\cos(\beta_r L) + j\sin(\beta_r L)} \tag{3.37a}$$

$$S_{31} = jk\frac{\tan(\beta_r L)}{\sqrt{1-k^2} + j\tan(\beta_r L)} \tag{3.37b}$$

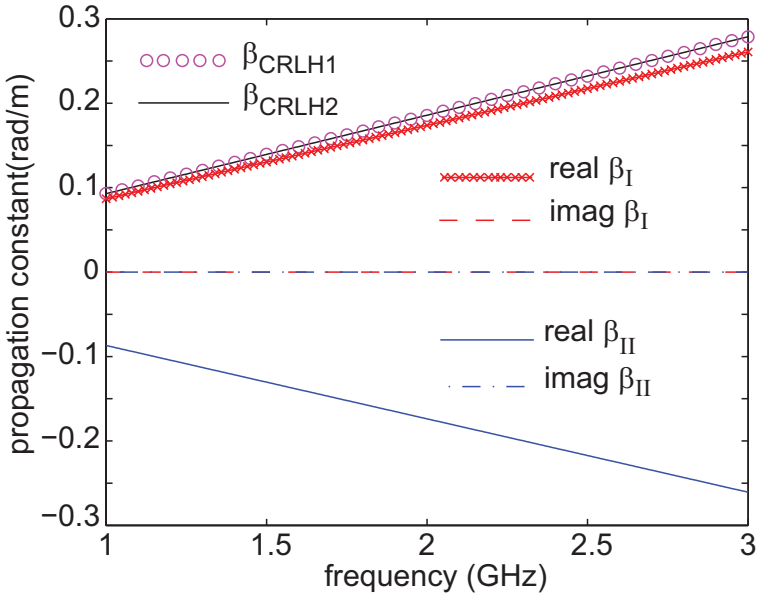

Figure 3.17 Coupled-mode propagation constants computed by (3.35) for the RH - RH coupled-line coupler prototype of Fig. 3.16(a) with the extracted parameters $L_{R1} = L_{R2} = 0.684$ nH, $C_{R1} = C_{R2}$ =0.298 pF, $L_{L1}, L_{L2}, C_{L1}, C_{L2} \rightarrow \infty$, $L_m = 0.167$ nH, $C_e = 0.072$ pF. The (identical) propagation constants for the two coupled lines (i.e. each line in the presence of the other one) are also shown for comparison.

which are recognized to be equivalent to the well-known even/odd mode expressions [52], [42] with $\beta = \beta_r$. The return loss, through, coupling and isolation parameters obtained by measurement, circuit simulation, quasi-TEM theory [(3.36) and (3.37)] and coupled-mode theory [(3.31)] are shown in Fig. 3.18. Excellent agreement is observed for the through (S_{21}) and coupled (S_{31}) parameters. The fact that the quasi-TEM approximate solution for S_{21} is closer than the coupled-mode theory solution to the measurement result may seem paradoxical, but is most likely due to the fact that the measured S_{21} is reduced by losses, not accounted for in the present coupled-mode theory modelling (for simplicity). In contrast, significant disagreement is observed between circuit simulation/measurement and the coupled-mode theory for the return loss (S_{11}) and isolation (S_{41}) results. This disagreement is explained by the fact that reflections due to imperfect matching [the impedance seen into the four ports of the coupler were designed based on the isolated lines impedance, (3.22d) whereas the exact impedance as modified by coupling is that given in (3.27)] are not taken

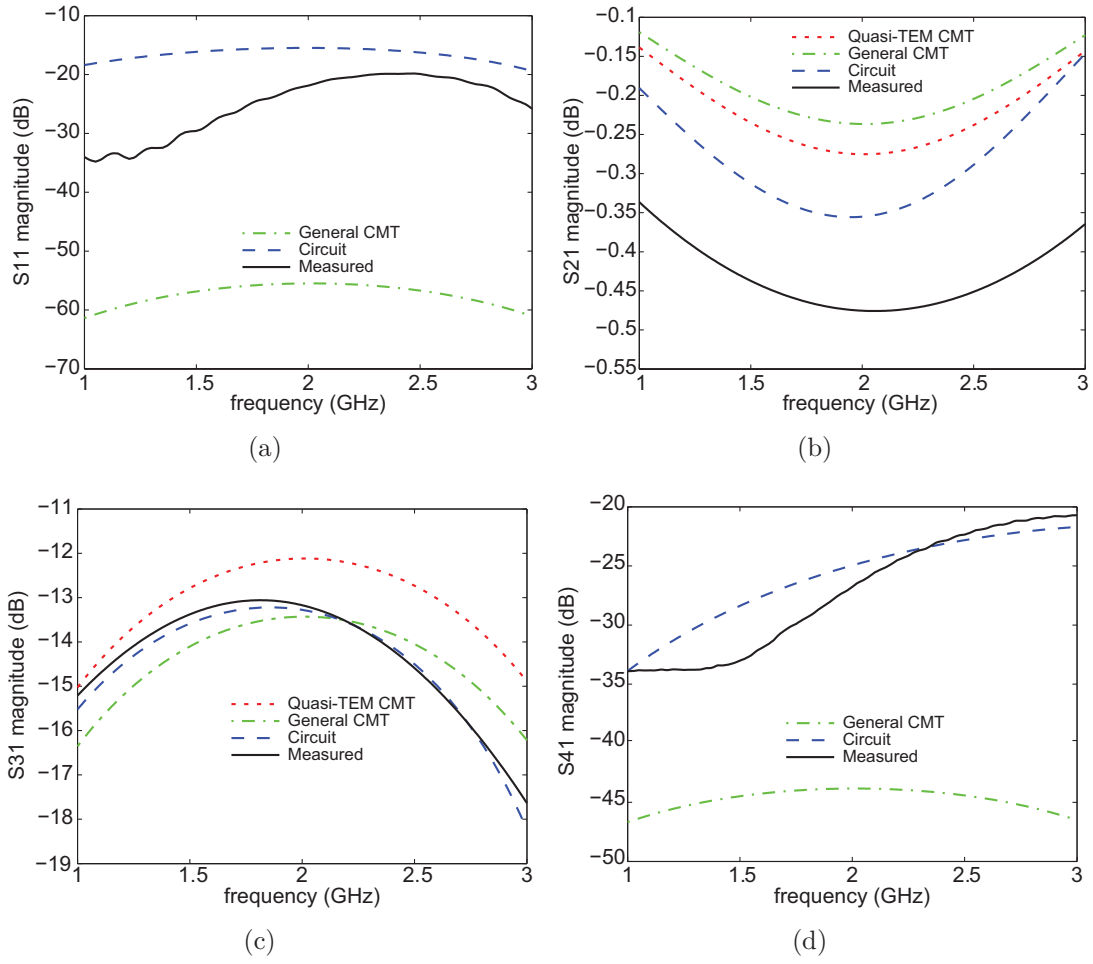

Figure 3.18 Scattering parameters obtained by measurement, circuit simulation, quasi-TEM approximation of coupled-mode theory [(3.36) and (16)] and general coupled-mode theory (CMT) [(3.31)] for the RH - RH coupled-line coupler of Fig. 3.16(a). a) Return loss, S_{11}, b) Through, S_{21}, c) Coupled, S_{31}, d Isolation, S_{41}.

into account in the present coupled-mode theory, while it is naturally included in the circuit simulation. In the case of perfect matching, the return loss and isolation would be very close to the coupled-mode theory result.

CRLH-CRLH Coupler (Case #2)

Let us now examine the CRLH−CRLH coupled-line coupler prototype shown in Fig. 3.16(b). Similar to the RH−RH coupler, this coupler is quasi-TEM, and therefore

can be analyzed by the quasi-TEM coupled-mode theory of subsection 3.3.2. We have here $\beta_d = 0$, with $k = (k_m + k_e)/2$, and may be either purely real or purely imaginary depending on the operating frequency range. These forward and backward propagation constants are plotted in Fig. 3.19, and are seen to be purely imaginary in the coupling range and purely real outside of the coupling range, as it may be easily verified mathematically. Also plotted in Fig. 3.19 are the propagation constants of each line in the presence of the other one. The coupled-mode propagation constants can be shown to be equivalent to the even and odd mode propagation constants described in [14] and [8], where the assumption $k_m \approx k_e$ is typically made. The

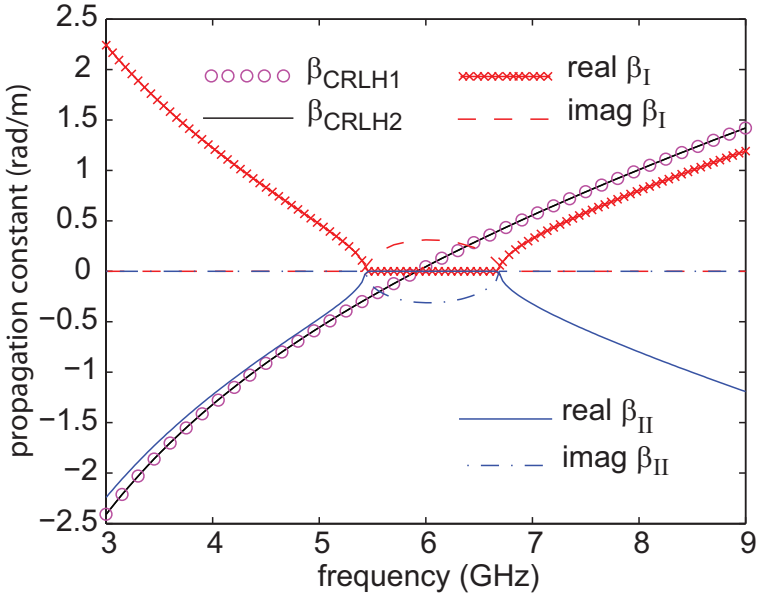

Figure 3.19 Coupled-mode propagation constant computed by (3.35) for the CRLH - CRLH coupler prototype of Fig. 3.16(b) with the following extracted parameters $L_{R1} = L_{R2}$ =1.938 nH, $C_{R1} = C_{R2} = 0.841$ pF, $L_{L1} = L_{L2} = 0.749$ nH, $C_{L1} = C_{L2} = 0.416$ pF, $L_m = 0.361$ nH, $C_e = 0.189$ pF. The (identical) propagation constants for the two coupled lines (i.e. each line in the presence of the other one) are also shown for comparison.

expressions for the through and coupled scattering parameters within the range where the coupled-mode propagation constants are purely imaginary can be simplified from

(3.36) to yield

$$S_{21} = \frac{|\beta_r|}{|\beta_r|\cosh(|\beta_r|L) - \beta_a \sinh(|\beta_r|L)} \tag{3.38a}$$

$$S_{31} = K_{BW} \frac{\tanh(|\beta_r|L)}{|\beta_r| + \beta_a \tanh(|\beta_r|L)} \tag{3.38b}$$

which are recognized to be equivalent to the even/odd mode expressions of [14] and [8] with $\beta = \beta_r$. The return loss, through, coupling and isolation parameters obtained by measurement, circuit simulation, quasi-TEM theory [(3.36) and (3.38)] and coupled-mode theory [(3.31)] are shown in Fig. 3.20. Similar observations as in the previous case may be made for the comparison of the different results.

As first shown in [14], this CRLH−CRLH TL coupler has the capability to achieve any level of coupling (up to quasi 0 dB) even in an edge-coupled configuration. This unusual and useful property is due to the *imaginary* nature of the coupled-mode propagation constant in the coupling range. As seen in (3.38) and plotted in Fig. 3.21, when β_r becomes imaginary, the trigonometric functions in (3.38) transform into hyperbolic functions and the coupling level consequently increases monotonically with the length of the coupler until complete coupling is achieved. Whereas the RH−RH coupler exhibits a well-known propagating coupled-mode periodic (trigonometric) response as a function of length, the CRLH-CRLH coupler exhibits an evanescent coupled-mode monotonic (hyperbolic) response as a function of length, which explains why the former has a bounded maximum coupling level whereas the latter can achieve complete power transfer to the coupled port. Mathematically, maximum coupling occurs in (3.38) when $\beta_a = 0$ (i.e. $\beta_{CRLH1} = \beta_{CRLH2} = 0$) and consequently these equations reduce to

$$S_{21} = \mathrm{sech}(\beta_r L) \tag{3.39a}$$

$$S_{31} = -j\tanh(\beta_r L) \tag{3.39b}$$

It should be noted that, even though maximum coupling occurs in the frequency range where the propagation constants are purely imaginary, coupling does not abruptly drop when frequency is moving to the bands where they are purely real. In fact, in these bands the coupler operates as a conventional coupled-line structure exhibiting coupling levels periodically varying with the length of the structure [(3.36)] instead

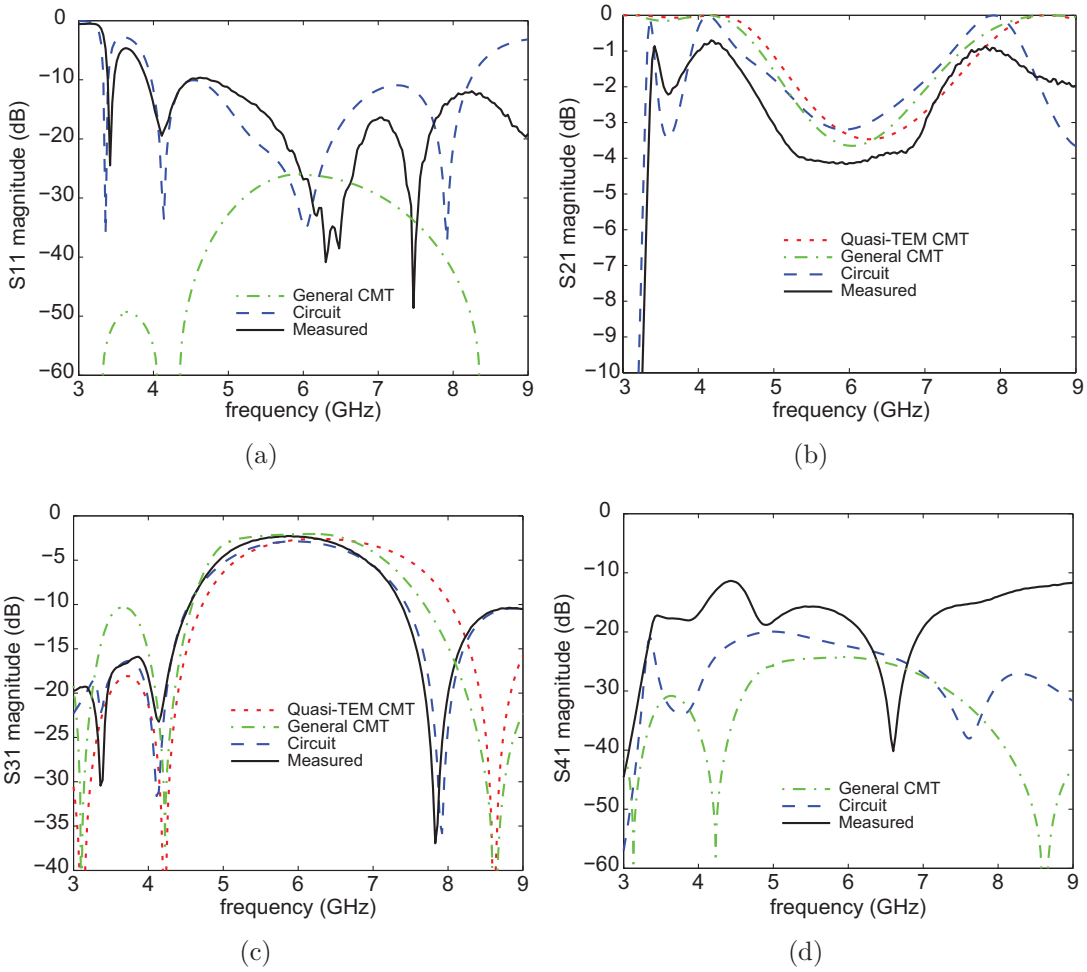

Figure 3.20 Scattering parameters obtained by measurement, circuit simulation, quasi-TEM approximation of coupled-mode theory [(3.36) and (3.38)] and general coupled-mode theory [(3.31)] for the CRLH-CRLH coupled-line coupler of Fig. 3.16(b). a) Return loss, S_{11}, b) Through, S_{21}, c) Coupled, S_{31}, d) Isolation, S_{41}.

of monotonically increasing to complete coupling.

RH-CRLH Coupler (Case #3)

Finally, let us consider the RH−CRLH coupled-line coupler shown in Fig. 3.16(c). This coupler is still quasi-TEM, but asymmetric and generally more complicated. As mentioned in subsection 3.3.2 , in the quasi-TEM approximation of the CMT, here we have $\beta_d = (\beta_{RH1} - \beta_{CRLH2})/2 \neq 0$, and $\beta_{I,II}$ is either purely real or complex in

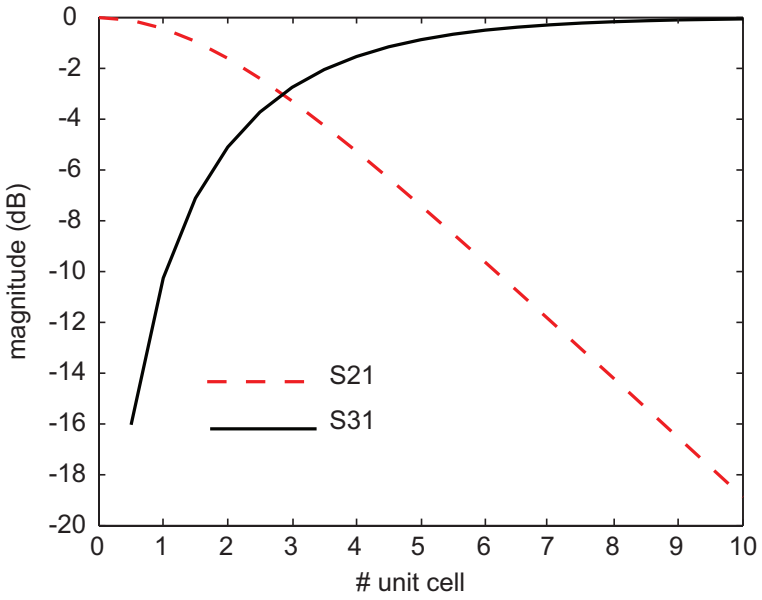

Figure 3.21 Coupled and through parameters computed by (18) as a function of the coupler length ($L = N \cdot p$) at the center frequency of coupling region. N: number of unit cell and p: size of each unit cell.

the frequency range where β_r is purely real and purely imaginary, respectively. These complex propagation constants are plotted in Fig. 3.22. They may be shown to be equivalent to the c and π mode propagation constants described in [60] and [59] for a metamaterial MS/NRI coupled-line coupler. As in the case of the CRLH−CRLH, arbitrary level of coupling can also be achieved, due here to the imaginary part of the complex propagation constant in the coupling frequency band.

The expressions for the through and coupled scattering parameters within the coupling range and at the frequency point where $\beta_{RH1} = -\beta_{CRLH2}$, simplified from (3.36), read here

$$S_{21} = e^{-j\beta_d L}\text{sech}(\beta_r L) \tag{3.40a}$$

$$S_{31} = -j\tanh(\beta_r L) \tag{3.40b}$$

which are recognized to be equivalent to the c and π mode expressions with $\beta_I = \beta_c$ and $\beta_{II} = \beta_\pi$. The return loss, through, coupling and isolation parameters obtained by measurement, circuit simulation, quasi-TEM theory [(3.36) and (3.40)] and

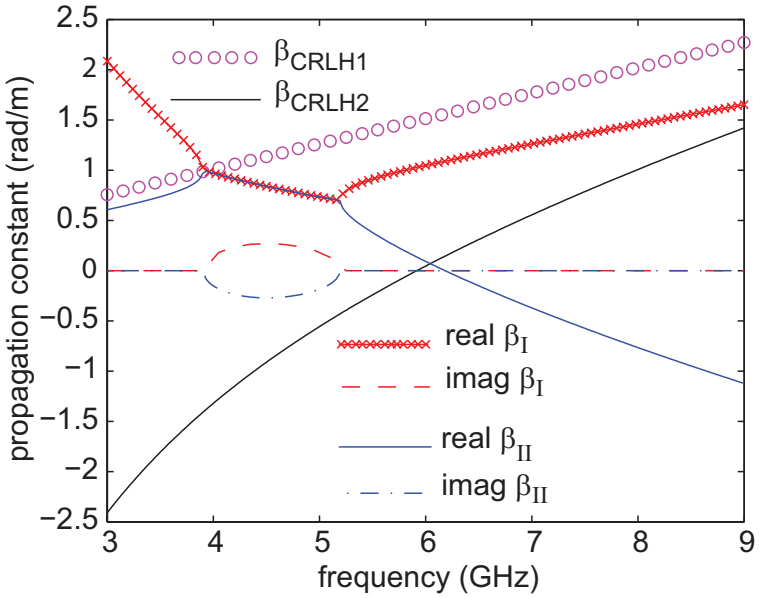

Figure 3.22 Coupled system propagation constant from (3.35) of RH - CRLH coupled-line coupler prototype for the parameters $L_{R1} = 2.903$ nH, $C_{R1} = 0.507$ pF, $L_{L1} = 1.225$ nH, $C_{L1} = 0.287$ pF, $L_{R2} = 1.415$ nH, $C_{R2} = 0.681$ pF, L_{L2}, $C_{L2} \to \infty$, $L_m = 0.684$ nH, $C_e = 0.130$ pF. The propagation constants for the two coupled lines (i.e. each line in the presence of the other one) are also shown for comparison.

coupled-mode theory [(3.31)] are shown in Fig. 3.23. Similar comments as in the previous two cases can be made here.

3.3.4 Conclusions

A completely rigorous and general coupled-mode approach of CRLH TL MTM coupled-line couplers has been presented. This approach is based on the CRLH generalization of the TLs constituting the coupler. Exact and quasi-TEM approximation formulas for the coupled mode propagation constants and scattering parameters have been derived, and accurate explanations have been provided to explain the unusual coupling phenomena, such as super-high coupling in edge couplers, occurring in the presence of CRLH MTM TLs. For a symmetric coupler with two CRLH TLs, the coupling analysis provides the exact maximal coupling around the transition frequency where the propagation constants of the two isolated CRLH TLs are zero $\beta_1 = \beta_2 = 0$. On the other hand, for a asymmetric coupler with one CRLH TL and one conven-

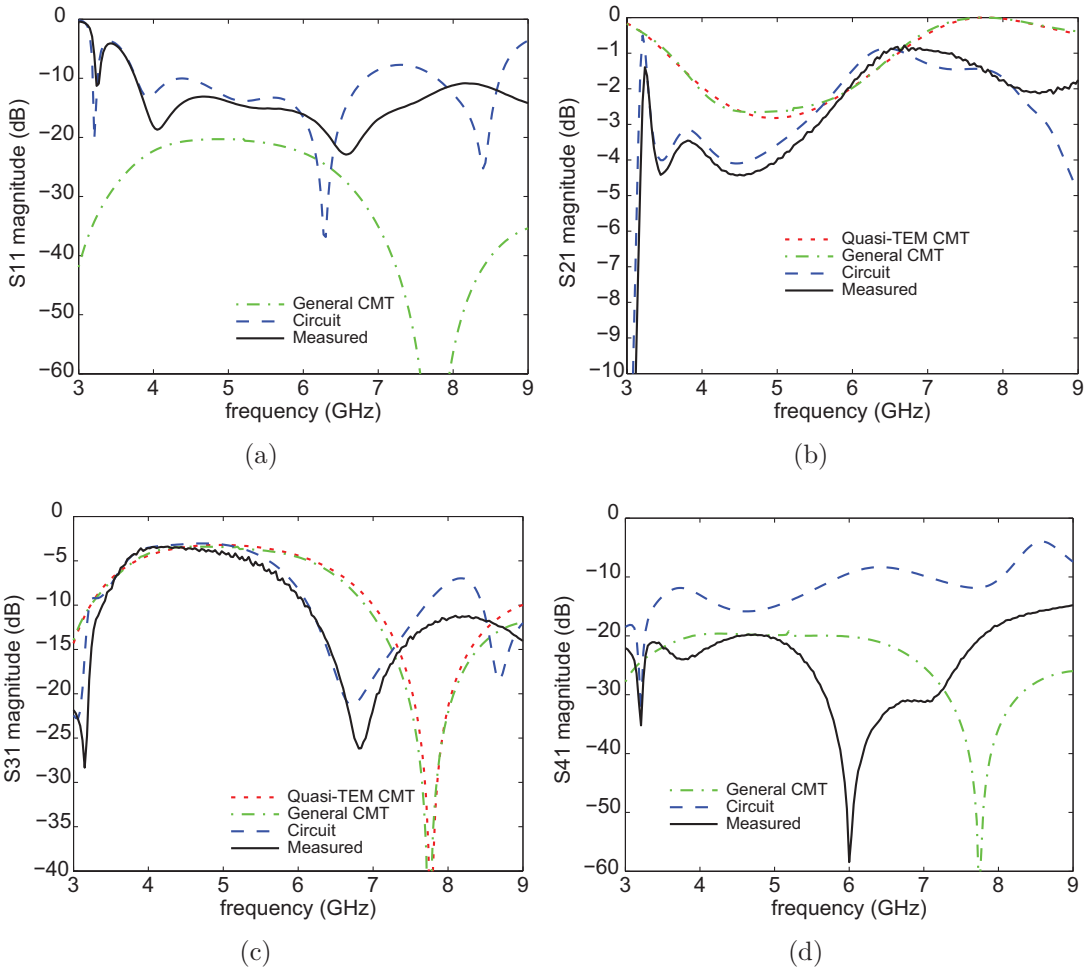

Figure 3.23 Scattering parameters obtained by measurement, circuit simulation, quasi-TEM approximation of coupled-mode theory [(3.36) and (3.40)] and general coupled-mode theory (CMT) [(3.31)] for the RH - CRLH coupled-line coupler of Fig. 3.16(c). a) Return loss, S_{11}, b) Through, S_{21}, c) Coupled, S_{31}, d) Isolation, S_{41}.

tional microstrip TL, the maximal coupling occurs when the propagation constants of the isolated lines are different from zero and exactly opposite $\beta_1 = -\beta_2 \neq 0$. Furthermore, in both cases, the coupling is shown to be proportional to the length which leads to an arbitrary level of coupling, up to close to 0 dB. The theoretical predictions and phenomenological explanations have been validated by experimental demonstration and circuit simulations for three different conventional and CRLH TL MTM couplers.

Chapter 4

Impulse Regime Guided-wave Components and Systems

The previous chapter presented novel microwave metamaterial components utilized in the harmonic regime guided-wave application, i.e. monochromatic sinusoidal excitation. There are, however, other microwave components and systems utilized in the impulse regime guided-wave application such as compressive receivers, pulse radar and impulse UWB communication systems. These systems operate in the time domain and employ periodic pulses of various shapes such as gaussian, monocycle, or cosine-square.

This chapter continues the guided-wave applications, but in contrast, introduces impulse regime component and system. Under impulse regime, the component and system either generate or being driven by periodic pulse excitation source. The component (time differentiator) exploits the interesting time derivative characteristic (first and second order) of the coupled-line coupler and is used to generate periodic pulse signals. On the other hand, the system (PPM transmitter) exploits the dispersive property of the CRLH TL MTMs and is driven by a periodic Gaussian pulse signal. This is the first time the dispersive characteristic of a CRLH TL MTMs is introduced in the impulse regime and applied to design a complete transmitter.

This chapter is organized as follows. Section 4.1 presents the first- and second-order time differentiators using a RH coupled-line coupler. The time-derivative effect of coupled-line couplers is shown theoretically by applying Kirchhoff's laws to infinitesimal electromagnetically coupled TL sections. The required operating condition is derived and the device is demonstrated experimentally and compared with the ideal (mathematical) derivators. In Section 4.2, the CRLH delay line PPM transmitter is proposed and demonstrated by circuit and experimental results for both binary and quaternary PPM.

4.1 Article 4: First- and Second-order Differentiators based on Coupled-line Directional Couplers

Coupled-line directional couplers are ubiquitous components in microwave circuits. They are widely employed in vector network analyzers, spectrum analyzers, radars, QPSK generators, power level sensors, and many other systems. The rigorous time-domain analysis of directional couplers based on coupled-modes theory was developed by B. M. Oliver in 1954 [61]. Oliver presented the complete coupling phenomenon and impulse response of the directional coupler with constant coupling for the first time in his work.

Since most conventional communication systems operate in a narrow-band harmonic regime with the exception of radar and UWB communication, the study of coupled-line couplers has been mostly performed in the frequency domain using the even/odd modes decomposition technique [52], [64]. However, this technique does not provide the exact nature of the electric and magnetic coupling occurring between the two coupled TLs of a coupled-line coupler.

This section demonstrates theoretically and experimentally the time-derivative effect of coupled-line couplers on electromagnetic pulses in the impulse regime. In comparison with analog differentiators, which consist of a capacitor, a resistor, and an operational amplifier [65], coupled-line couplers exhibit a simple, purely passive and scalable configuration. Moreover, a single coupled-line coupler may provide first-, second-, and possibly higher-order time-derivation. The proposed differentiators may find various applications in radar and UWB communication systems [17] and in photonics.

4.1.1 Time-Derivative Characteristics of Coupled-line Couplers

Demonstration of the Time-Derivative Effect

Figure 4.1 shows a coupled-line coupler with an input TL (TL 1) and an infinitesimal (d_z) coupled output TL section (TL 2) to be used for the demonstration of the time-derivative effect. The input line is excited by a voltage source v_1 at port 1 and

terminated by a matched impedance Z_2 at port 2. The infinitesimal section $\triangle z$ of TL 2 is terminated by the impedances Z_3 and Z_4. Electric and magnetic coupling between two lines are modelled by the coupling capacitance C_{12} (F/m) and mutual inductance L_{12} (H/m), respectively. The time-varying voltage v_1 on line 1 impresses a displacement current $\triangle i_2$ through C_{12}. The time-varying current i_1 induces an electromotive force voltage $\triangle v_2$ on line 2 through L_{12}. A detail of electromagnetic coupling derivation of the coupling current and voltage is summarized in Appendix C [66]. The coupling current and voltage are given approximately as

$$\triangle i_2 = (C_{12}\triangle z)\frac{dv_1}{dt}, \tag{4.1a}$$

$$\triangle v_2 = (L_{12}\triangle z)\frac{di_1}{dt}. \tag{4.1b}$$

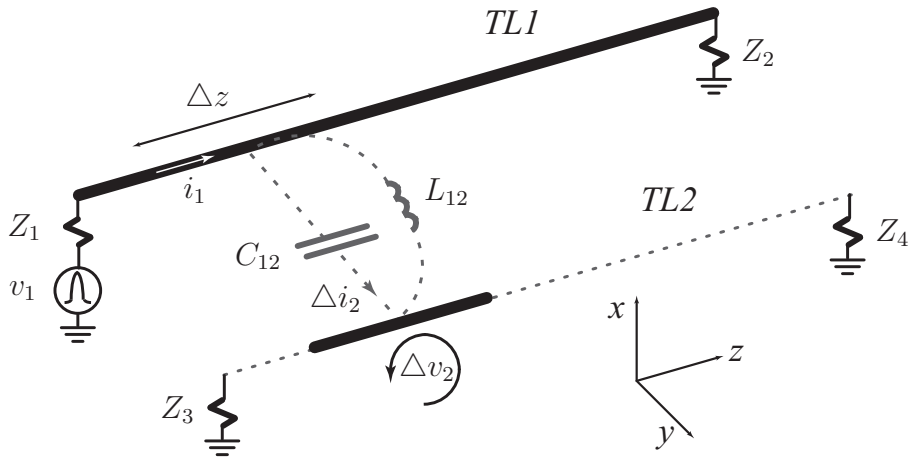

Figure 4.1 Coupled-line coupler with an input TL (line 1) and an infinitesimal (d_z) coupled output TL section (line 2) used for the demonstration of the time-derivative effect. The electric and magnetic couplings are modelled by the capacitor C_{12} and the inductor L_{12}, respectively.

The current arriving at impedance Z_3 is a superposition of two contributions: 1) $\triangle i_2$ and 2) $\triangle v_2$ and is given as

$$\triangle i_{Z_3} = \left(\triangle i_2 \frac{Z_4}{Z_3 + Z_4} + \triangle v_2 \frac{1}{Z_3 + Z_4}\right). \tag{4.2}$$

By substituting (4.1a) and (4.1b) into (4.2) and using the assumption that the

coupler is matched so that $di_1/dt = \frac{1}{Z_1} dv_1/dt$, the voltage at impedance Z_3 for an infinitesimal section $\triangle z$ can be expressed in terms of the input voltage on line 1, v_1 as follows

$$\triangle v_{Z_3} = Z_3 \frac{(Z_4 C_{12} + L_{12}/Z_1)}{Z_3 + Z_4} \frac{dv_1}{dt} \triangle z. \tag{4.3}$$

For a coupled TL 2 of length $z = \ell$, the voltage at impedance Z_3 or port 3 is the sum of all of the infinitesimal voltages $\triangle v_{Z_3}$, which yields by integration of (4.3)

$$\begin{aligned} v_{p3} &= \int_{z=0}^{z=\ell} \left[\frac{Z_3 (Z_4 C_{12} + L_{12}/Z_1)}{Z_3 + Z_4} \frac{dv_1}{dt} \right] \triangle z \\ &\cong \left[\frac{Z_3 (Z_4 C_{12} + L_{12}/Z_1)}{Z_3 + Z_4} \ell \right] \frac{dv_1}{dt} \propto \frac{dv_1}{dt}, \end{aligned} \tag{4.4}$$

where dv_1/dt has been taken outside of the integral, based on the assumption that dv_1/dt exhibits a negligible variation over the interval $z = [0,\ \ell]$. This assumption is valid if the duration ΔT of the input pulse is much larger than its travel time τ across the coupler, i.e. $\Delta T \gg \tau = \ell/v_g$, where v_g is the group velocity. In the case of a conventional directional coupler (case considered in this paper), which is a quarter of guided wavelength long at the coupling center frequency f_0, this condition reads $\Delta T/\tau = 4\Delta T v_g/\lambda_g = 4\Delta T f_0 \ \gg \ 1$ or $\Delta T \gg \ 1/(4f_0)$, showing that shorter pulses can be handled by couplers designed at higher frequencies. When the pulse duration is large enough so as to satisfy this condition, then the approximation in (4.4) is valid and it is therefore clear that v_{p3} is proportional to the time-derivative of the input voltage v_1.

This time derivation effect is generally expected, since both inductive and capacitive coupling are simultaneously present in a coupled-line coupler. Either inductive or capacitive coupling can produce the time derivation in a coupled system providing the above condition is satisfied.

If $Z_1 = Z_3 = Z_4 = Z_0 = Y_0^{-1}$, as in a conventional coupler, and if we consider that the coupler must be a quarter-wave in length at the signal center frequency for maximal coupling ($\ell = \lambda_g/4$), (4.4) reduces to

$$v_{p3} = \frac{(Z_0 C_{12} + L_{12} Y_0)}{2} \ell \frac{dv_1}{dt} = \frac{\lambda_g}{8} (Z_0 C_{12} + L_{12} Y_0) \frac{dv_1}{dt}, \tag{4.5}$$

where the coupling coefficient $\lambda_g(Z_0C_{12} + L_{12}Y_0)/8$ is necessarily smaller than, but as close as possible to unity, to provide the time-derivation with minimal attenuation.

First-order Derivative

Figure 4.2(a) shows a simple directional coupler configuration for a first-order time derivation. An input Gaussian pulse with a full-width 1.27 ns and a delay of 2 ns is applied at the input port (port 1). Fig. 4.2(b) shows the input Gaussian pulse, its analytical first-order time derivative, and the full-wave simulated output pulse. For comparison, the analytical time-derivative pulse is time-shifted by approximately 0.22 ns to align with the simulated output pulse. This time shift corresponds to the actual time delay between the input and coupled ports of the actual directional coupler. The simulated output pulse is wider than the ideal analytical derivative due to the limited bandwidth of the coupler.

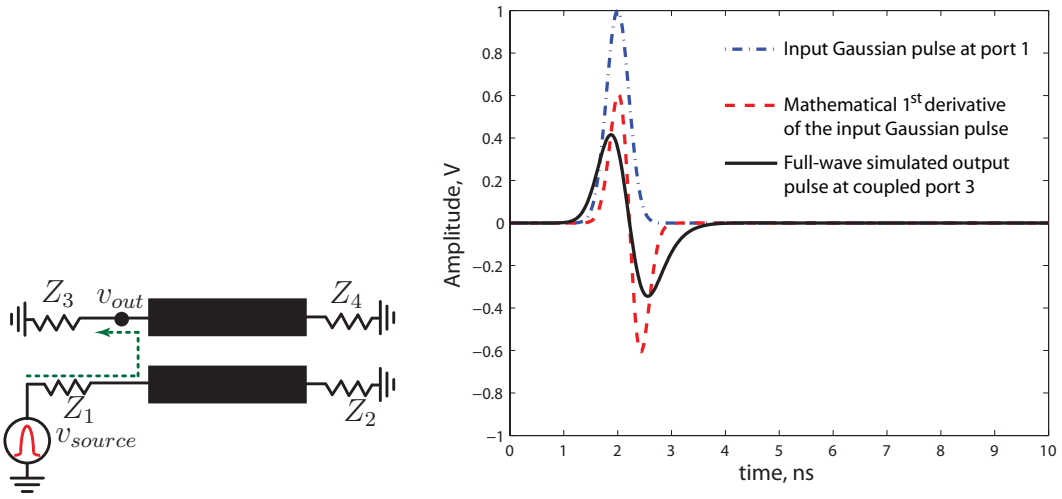

(a) (b)

Figure 4.2 First-order time-derivative effect of the coupled-line coupler. (a) Coupler configuration with center frequency of $f_0 = 1.9$ GHz. (b) Input Gaussian pulse with full width of $\Delta T = 1.27$ ns ($\Delta T f_0 = 2.41 \gg 0.25$), analytical 1st derivative of the input Gaussian pulse, and full-wave simulated output pulse at the coupled port. The full-wave simulation is for a 3-dB broadside-coupled stripline.

Second-order Derivative

In a coupled-line coupler, coupling occurs between ports 2 and 4 as well as between ports 1 and 3, depending on the location of the input port. In the first-order differentiator mentioned above, ports 2 and 4 were not used and were terminated with matched loads. Since coupling also occurs between ports 2 and 4, a second-order time derivation of the pulse injected at port 1 can be achieved by re-applying the output pulse at port 3 into port 4 and collecting the output pulse at port 2. This is illustrated in Fig. 4.3(a). A time delayer is inserted in the loop connecting ports 3 and 4 to eliminate any overlap between the direct output pulse and the second-order time derivative pulse at port 2. The finite directivity of practical directional couplers (in addition to their limited bandwidth) might distort the first-order time derivative pulse at port 4, due to signal leakage from port 1 to port 4. However, this effect might be minimized by using a high-directivity broadside coupled-line coupler [52], [64].

Figure 4.3(b) shows the input Gaussian pulse, its time-shifted analytical second-order time-derivative, and the full-wave simulated output pulses at port 2. The first pulse arriving at port 2 is the direct through pulse (which might be suppressed by a triggered diode mechanism) while the second pulse is the desired and delayed (by $\tau = 7.4$ ns) second-order time-derivative. Again, the resulting wider pulse compared to its analytical representation is a result of the coupler's limited bandwidth.

4.1.2 Coupled-line Coupler Implementation and Results

A broadside coupled-line coupler was realized in a multilayer stripline configuration to provide a coupling of ≈ 3 dB and a directivity of 23 dB. The prototype is shown in the inset of Fig. 4.4(a). The input Gaussian pulse is approximated by a narrow pulse generated by the Picosecond Pulse Lab's pulse generator, model 10.070 A and the output pulses are recorded by a Agilent's digital sampling oscilloscope (DSO), model 81204B.

The input pulse is divided by a T-junction splitter where one part of the pulse signal is connected to the DSO while the other part is applied to the coupler's input port 1. The mathematical first- and second-order time derivative pulses are obtained by using a built-in differential mathematical function of the DSO. Figs. 4.4(a) and 4.4(b) show the measured first- and second-order time-derivative pulses obtained for the configurations of Figs. 4.2(a) and 4.3(a), respectively.

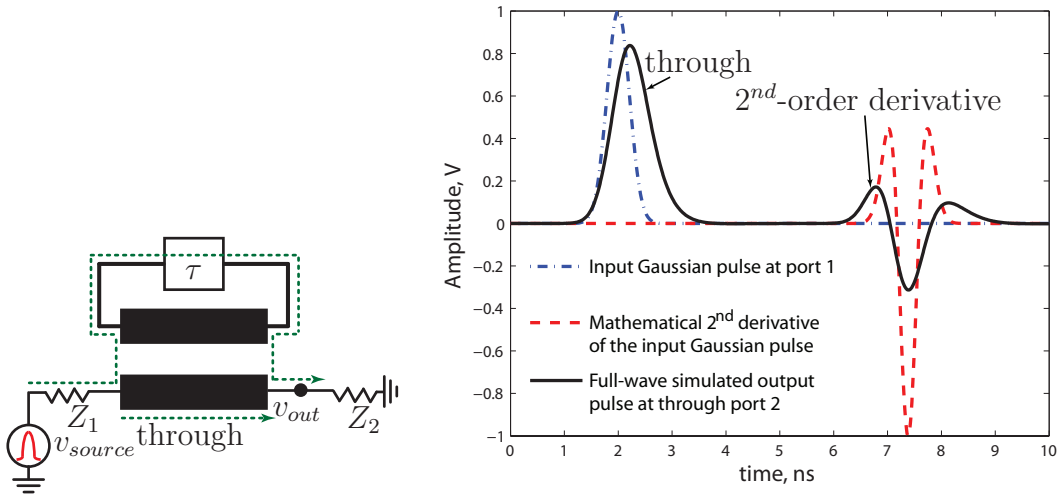

Figure 4.3 Second-order time derivative effect of the coupled-line coupler. (a) Coupler configuration. (b) Input Gaussian pulse having a width of 1.27 ns, analytical 2nd order derivative of the input Gaussian pulse, and full-wave simulated output pulse at port 2. The parameters of the coupler are the same as in Fig. 4.2.

4.1.3 Conclusions

This section has demonstrated the first- and second-order differentiators using a single coupled-line coupler. A detail explanation of the electromagnetic coupling behavior of coupled-line couplers was provided using Maxwell's equations. In particular, the electric coupling was explained by considering a displacement current flowing from the input (excited) TL 1 to the output (coupled) TL 2 in the presence of a time-varying voltage on TL 1 and the magnetic coupling was explicated by considering a magnetic flux linkage between TL 1 and TL 2 in the presence of a time-varying current on TL 1. Based upon this coupling analysis, the time-domain relation between the input and coupled output signals has been derived and it reveals a time-derivative effect of conventional coupled-line couplers. An operating condition of the time-derivation is developed and proven accurate under the condition $\Delta T f_0 \gg 1/4$, where T and f_0 are the pulse width and central frequency of coupled-line couplers.

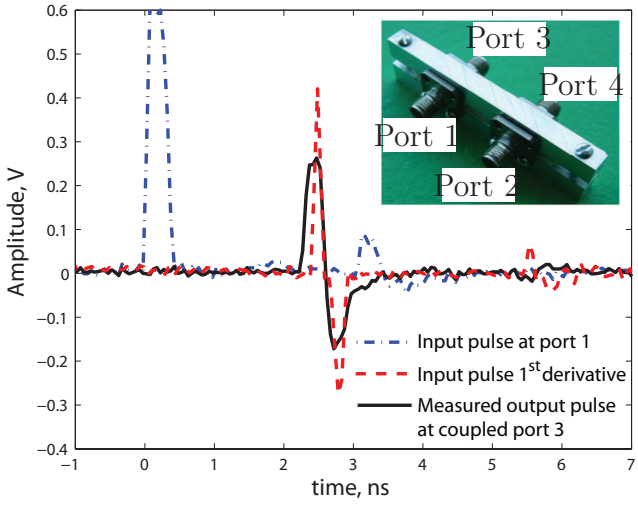

(a)

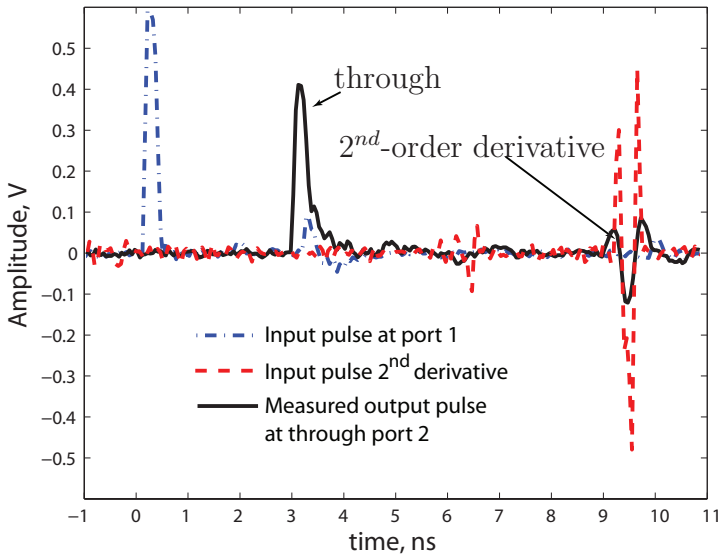

(b)

Figure 4.4 Measured results with a broadside coupled-line coupler prototype (shown in the inset) excited by a short pulse. All the parameters are the same as in Figs. 4.2 and 4.3. The coupler is fabricated in multilayer PCB technology using two Rogers substrates with a dielectric permittivity of 3.38 and a thickness of 1.52 mm. The TL width is 0.2 mm and the broadside spacing between the lines is 0.025 mm. (a) First-order time derivative. (b) Second-order time derivative.

4.2 Article 5: CRLH Delay Line Pulse Position Modulation Transmitter

The previous section presented a passive time differentiator suitable for periodic impulse signal generation which can be used in radar or UWB communication systems. In a pulsed communication system, the two common methods for pulse modulation are *shape-based* and *time delay-based* approaches. In the former case, techniques such as bi-phase modulation, on-off keying modulation or pulse amplitude modulation modulate the shape of the pulse at a fixed time position. In the latter case, PPM scheme modulates the time delay of the pulse within the duration of a clock period. PPM, where the time delay is imposed either by active delay lines (logic gate inverters) [67], [19], [68], or passive delay lines using switches [21] is a popular method due to its simplicity and potential for multiple order modulation capability [69]. However, the delay lines in these approaches consume power, add noise to the signal and are restricted to discrete time steps.

This section presents, for the first time, a CRLH delay line-based PPM transmitter. This transmitter exploits an inherent dispersive property of the CRLH TL and exhibits a simple design, continous tunable time delay and multiple-order PPM capability. The PPM transmitter is validated with both circuit simulation and measurement.

4.2.1 PPM Transmitter System: Principle of Operation and Advantages

Fig. 4.5 shows the block diagram of the proposed CRLH dispersive delay line-based PPM transmitter. This transmitter operates as follows for an M-ary modulation scheme. A frequency source generates 2^M carrier frequencies $\omega_{c,s}$ ($s = 0 \ldots 2^M - 1$) to code the 2^M states. For example, if $M = 1$ (binary PPM), two frequencies are generated to code the symbols 0 and 1, while if $M = 2$ (quaternary PPM), four frequencies are generated to code the symbols 00, 01, 10 and 11. These 2^M frequencies are mixed with a Gaussian pulse signal $a(t)$ from a pulse generator by a mixer. The resulting frequency-modulated Gaussian pulse signal $c(t)$ at the output of the mixer enters a dispersive CRLH TL. The line delays this signal $c(t)$ proportionally to the various carrier frequencies. As a result, the modulated Gaussian pulse signal $d(t)$ at

the output of the line exhibits different time delays (i.e., a different pulse position in time) for different data bits. This is the basis of PPM. Finally, the time-encoded Gaussian pulse signal $d(t)$ is transmitted by a wide-band antenna.

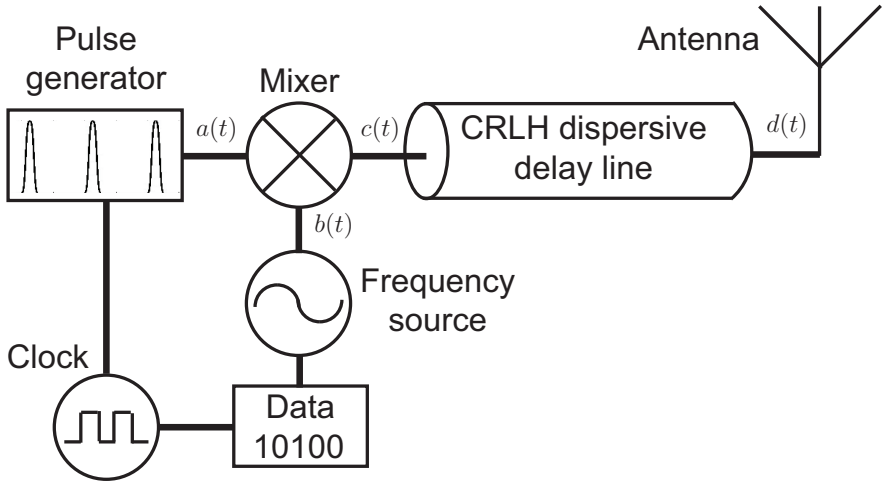

Figure 4.5 Block diagram of the proposed CRLH dispersive delay line pulse position modulation (PPM) transmitter.

In this PPM transmitter, the dispersive CRLH TL comprised of unit cells containing L_R, C_R, and L_L, C_L [4] provides the tunable delay required to code the information. The propagation constant of this line is obtained by the application of Bloch-Floquet's theorem [refering to (1.7)] as

$$\beta(\omega) = \frac{1}{p}\cos^{-1}\left(1 + \frac{\chi}{2}\right), \tag{4.6}$$

where $\chi = (\omega/\omega_R)^2 + (\omega_L/\omega)^2 - \kappa\omega_L^2$, $\omega_R = 1/\sqrt{C_R L_R}$, $\omega_L = 1/\sqrt{C_L L_L}$, $\kappa = L_R C_L + L_L C_R$, and p is the size of each unit cell. The group velocity of a modulated signal propagating along a balanced ($L_R C_L = L_L C_R$) CRLH TL is obtained by taking the inverse derivative with respect to frequency of the propagation constant given in (4.6) evaluated at the carrier frequency ω_c. The corresponding group delay for the modulated signal is

$$\tau_g(\omega_c) = \frac{N}{\sin(\beta p)}\left(\frac{\omega_c}{\omega_R^2} - \frac{\omega_L^2}{\omega_c^3}\right), \tag{4.7}$$

where N represents the number of unit cells of the CRLH TL. Thus, the time delay τ_g of the modulated signal across the balanced CRLH TL depends on the carrier

frequency ω_c and may therefore be tuned by varying ω_c [24].

Utilizing a train of pulses with a predefined shape, the PPM transmitter modulates the data by the time delay τ_g. Here, the Gaussian function has been selected for the pulse shape. The Gaussian pulse train, which reads $a(t) = \sum_{n=0}^{\infty} p(t - nT_f)$, where $p(t) = a_0 e^{-t^2/(2\sigma^2)}$, is a time domain Gaussian pulse with full-width half maximum $2\sqrt{2\ln(2)}\sigma$, and T_f is the pulse repetition period. The mixer modulates the Gaussian pulse train $a(t)$ with the carrier signal $b(t) = B\cos(\omega_c t)$ ($\omega_c = \omega_{c,s}$ with $s = 0 \ldots 2^M - 1$) and provides the frequency modulated Gaussian pulse train to the input of the CRLH dispersive delay line. At the output of this line, the time-encoded and frequency-modulated Gaussian pulse train is given as

$$d(t, \omega_c) = B\cos(\omega_c t) \sum_{n=0}^{\infty} p\left[t - nT_f - \tau_g(\omega_c)\right]. \tag{4.8}$$

The proposed PPM transmitter exhibits three important advantages. First, in comparison to [67], [19], and [68], the CRLH dispersive delay line, being constituted of purely passive L and C elements, does not consume any DC power and also does not generate any active noise. Moreover, it may be easily scaled to any frequency, allowing virtually no limitation in the operating frequency range of the overall system. Second, in contrast to discrete delay achieved by logic inverters or switches, this line provides a continuously tunable time delay as shown by (4.8), where ω_c may be continuously varied. Third, as consequence of its continuous delay, the proposed system has an inherent capability to support arbitrary M-ary PPM, where required time delays are achieved by simply mapping each data bit to a single carrier frequency within the continuous operating frequency range.

4.2.2 Circuit Simulation for Binary and Quaternary Modulations

The PPM transmitter of Fig. 4.5 is implemented in Agilent's ADS circuit simulator. The CRLH's unit cell is implemented using ideal passive L, C elements with the following values of $L_L = 1.9$ nH, $C_L = 0.9$ pF, $L_R = 3.8$ nH, and $C_R = 1.8$ pF, with $N = 30$ and $N = 60$ unit cells for binary and quaternary PPM cases, respectively. The Gaussian pulse train has 10 ns pulse width and 40 ns pulse repetition rate. The input Gaussian pulse train is position-modulated by $2^1 = 2$ and $2^2 = 4$ possible time delays

for the binary and quaternary PPM, respectively. Table 4.1 summarizes the mapping between the data bits and their carrier frequencies, as well as the corresponding time delays computed from (4.7) for the above mentioned parameters.

Table 4.1 Mapping between data bits and carrier frequencies for binary ($M = 1, N = 30$) and quaternary ($M = 2, N = 60$) PPM

State	Binary PPM			Quaternary PPM			
	bit	f_c	τ_g	bits		f_c	τ_g
s	b_0	(GHz)	(ns)	b_1	b_0	(GHz)	(ns)
0	0	2.500	5.47	0	0	2.500	10.95
1	1	1.725	11.89	0	1	2.050	15.34
2	–	–	–	1	0	1.850	19.53
3	–	–	–	1	1	1.725	23.77

Binary Modulation ($M = 1$)

Fig. 4.6(a) shows the random test data stream b_0 and Fig. 4.6(b) shows the input Gaussian pulse signal $a(t)$ and its modulated output signal $d(t)$. It is clearly apparent from Fig. 4.6(b) that the pulse positions (i.e. the peaks of the pulse) have been properly delayed according to the test data stream.

The time interval between pulses experiencing a transition from state k to state l, $(k, l = 0, 1)$, reads

$$\tau_{kl} = \tau_{g,l} - \tau_{g,k} + T_f. \tag{4.9}$$

Equation (4.9) reveals the exact time interval τ_{kl}, which unambiguously informs on the two states involved in this transition. This shows that PPM is a *non-coherent* modulation scheme, which does not require any synchronization between the transmitter and the receiver. Equation (4.9) holds for any arbitrary M-ary PPM, where the total number of possible transitions is $2^M(2^M - 1)$.

Quaternary Modulation ($M = 2$)

Fig. 4.6(a) shows the random test data streams b_1 and b_0 while Fig. 4.6(c) shows the input and modulated output Gaussian pulse signal $a(t)$ and $d(t)$, respectively. The pulses with greater delays (10 and 11) have a wider width and a lower amplitude than

the other two pulses (00 and 01) due to the fact that their carrier frequencies are closer to the LH cutoff frequency of the CRLH delay line where dispersion is maximum. This effect is more profound in the quaternary modulation than in the binary modulation because the CRLH dispersive delay line is twice longer in the former case. Here, in reference with (4.9), $k, l = 0, 1, 2, 3$ and $2^2(2^2 - 1) = 12$ transitions are possible. The situation of Fig. 4.6(c) shows only some of these transitions.

4.2.3 Transmitter Implementation and Experimental Results

The proposed PPM transmitter is demonstrated for both binary and quaternary modulation schemes with the pulse repetition rate of 20 MHz. Fig. 4.7(a) shows the setup implementation of the block diagram illustrated in Fig. 4.5. The wireless link is completed by standard transmitting and receiving wideband bow-tie antennas. The receiving antenna is directly connected to an oscilloscope to monitor and record the received modulated Gaussian pulse signal. Fig. 4.7(b) shows a zoomed-view of the prototype, showing the CRLH dispersive delay line implemented in MIM configuration with a unit cell size of $p = 15$ mm. Commercial switches and a mixer are used to select and modulate the Gaussian pulses with the carrier frequencies and generate a loss of 8dB in addition to the loss in the CRLH line (2dB) and propagation path loss between antennas.

Fig. 4.8(a) shows the result measured by the oscilloscope for binary PPM. The lower trace is a replica of the random transmitted test data stream from the data generator and is used to compare the transmitted and received signals. The upper trace is the modulated Gaussian pulse signal received at the receiving antenna. The received pulse signal corresponding to a data bit 1 has a longer time delay than that of a data bit 0, in agreement with the theoretical prediction (4.7) and the circuit simulation shown in Fig. 4.6(b). Fig. 4.8(b) shows the corresponding measured results quaternary PPM. Again, the experimental results validate the theory and circuit simulations.

4.2.4 Conclusions

This section has presented the first PPM transmitter application exploiting the dispersive property of CRLH TLs. It was shown that a frequency modulated pulse propagating through CRLH TLs has a continuous and tunable time delay as a function

of the modulating (carrier) frequencies ω_c. The tunable time-delay property was applied to build the PPM transmitter, which supports both binary and quaternary pulse modulation schemes. The PPM transmitter has been demonstrated by circuital simulation and experimental measurement in an actual wireless link. In comparison to conventional PPM transmitters, the CRLH delay line PPM transmitter exhibits the advantages of simple design, continuously tunable time delay and multiple order PPM capability.

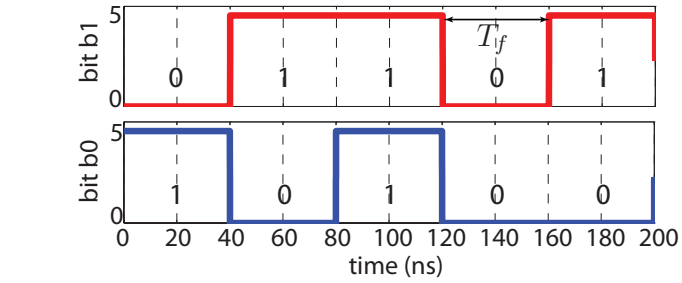

(a)

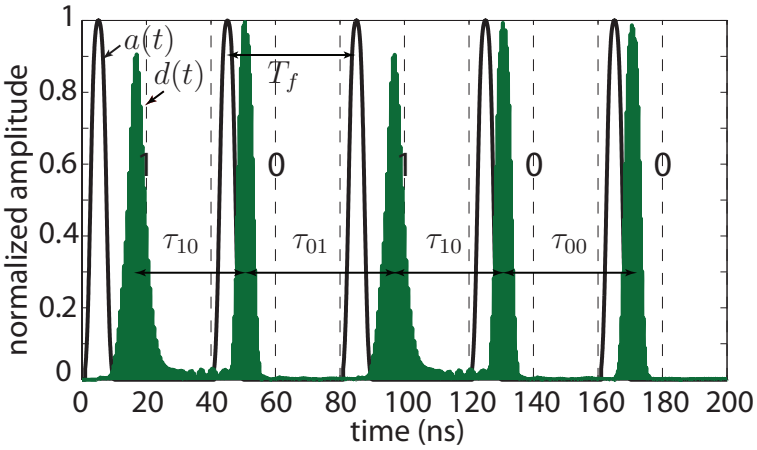

(b)

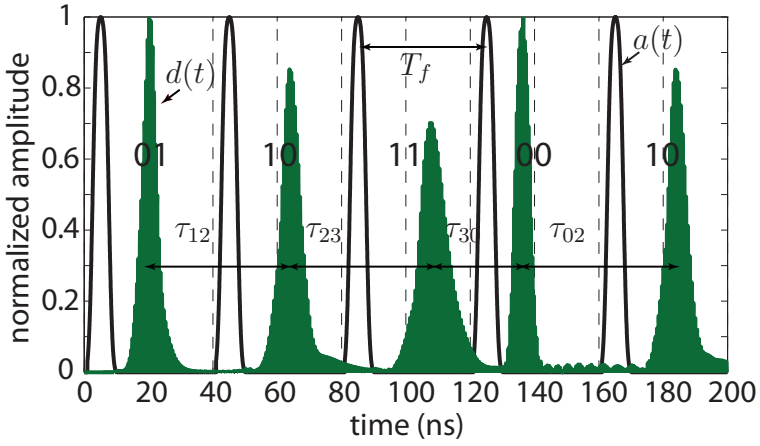

(c)

Figure 4.6 Circuit simulation results for binary and quaternary PPM. (a) Test information data stream b_1 and b_0. Normalized amplitude of the input Gaussian pulse signal $a(t)$ and the output modulated Gaussian pulse signal $d(t)$ [(4.8)]. (b) Binary PPM with time intervals of transition between states $\tau_{01} = 46.41$ ns and $\tau_{10} = 33.59$ ns from (4.9). (c) Quaternary PPM with time intervals of transition between states $\tau_{12} = 44.19$ ns, $\tau_{23} = 44.24$ ns, $\tau_{30} = 27.18$ ns and $\tau_{02} = 48.58$ ns from (4.9).

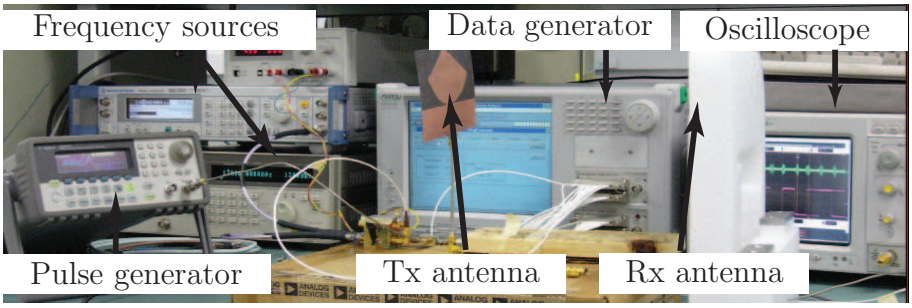

(a)

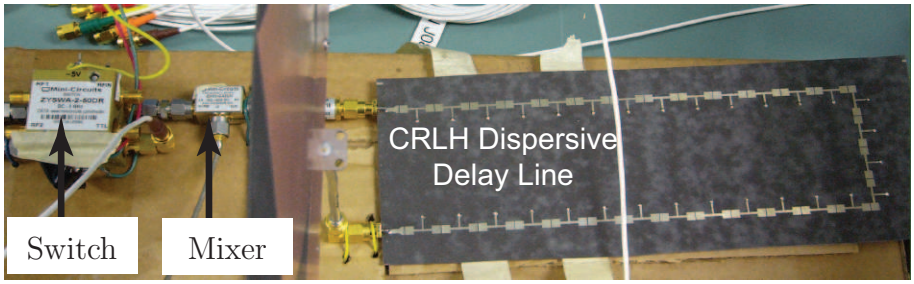

(b)

Figure 4.7 CRLH dispersive delay line-based PPM transmitter experimental setup. (a) Global view. (b) Zoomed view of the fabricated hardware.

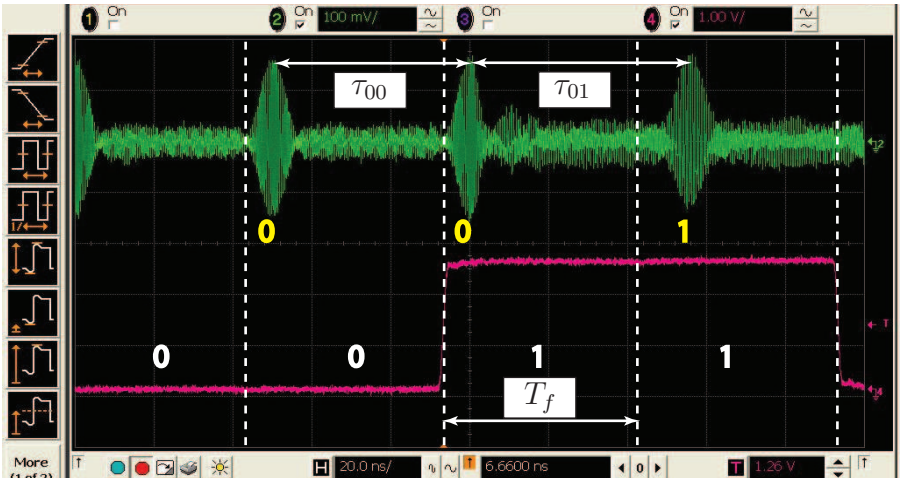

(a)

(b)

Figure 4.8 Measured results. (a) Binary PPM transmission for the parameter of Table 4.1. The measured pulse delay times of the CRLH line for bit 0 and 1 are 5.6ns and 12.1ns, respectively. (b) Quaternary PPM transmission for the parameter of Table 4.1. The measured pulse delay times of the CRLH line for states 0, 1, 2, and 3 are 11.2ns, 15.7ns, 19.3ns and 24.2ns, respectively.

Chapter 5

Radiated-wave Components and Systems

Unlike guided-wave components and systems presented in the preceding two chapters, where the applied electromagnetic energy is confined to the components and is prohibited from radiation, radiated-wave components and systems in this chapter harness the leaky-wave radiating property of the CRLH TLs. Leaky-wave antennas (LWAs) are an example of radiated-wave application of CRLH TLs and constitute the main topic of the present chapter.

The LWAs presented in this chapter are excited by a sinusoidal source and therefore radiate a monochromatic signal having a propagating direction as a function of the applied frequency. Impulse time-domain signals such as Gaussian or monocycle pulses can also be applied to the LWA to create multiple beams at the same time. Impulse-driven LWAs find applications in optic-inspired microwave devices such as real-time spectrum analyzer [70], frequency resolved electrical gating (FREG) and pulse generators [71]. Impulse-driven LWAs will not be presented in this chapter as it is not within the scope of this dissertation.

Traveling LWAs have important advantages of low-cost and small size due to the absence of a feeding network, while also being more directive due to their travelling-wave nature. However, being a travelling-wave antenna is also disadvantageous in terms of efficiency, requiring that most of the power has leaked out before reaching the termination. One approach to improve the radiation efficiency is to increase the antenna's length. However, for 90% efficiency, the LWA's length is required to be in the order of ten of λ_0, which is impractical at low frequencies [72].

This chapter presents two novel approaches to enhance the radiation efficiency of LWAs without increasing the antenna's length. Section 5.1 presents a power-recycling concept based using a series feeding network to improve the radiation efficiency of a conventional 2D LWA array. This is achieved by effectively *cross-recycling* the

remaining power at the end of one antenna element to the neighboring element. This approach allows a significant amount of input power to leak out before reaching the terminated loads and therefore increases the radiation efficiency.

Section 5.2 further extends the power-recycling concept, however uses only a single LWA having arbitrary radiation efficiency and a rat-race coupler. This novel *self-recycling* technique maximizes the LWA's radiation efficiency by feeding back the non-radiated power at the end of the LWA into its input via the rat-race coupler. The rat-race coupler combines this feedback power with the applied input power and produces a larger sum power to the input of the LWA, hereby increases the radiated power and the radiation efficiency.

5.1 Article 6: Highly-Efficient Leaky-wave Antenna Array using a Power-Recycling Series Feeding Network

This section presents a solution to improve the efficiency of a 2D LWA array, where the power reaching the end of a LWA element is cross-recycled into the adjacent LWAs instead of being simply dumped into a terminated load. This approach maintains a narrow radiation pattern while dramatically improving the radiation efficiency as well as the array's gain. In this work, a planar CRLH TL LWA array was selected to demonstrate the proposed concept. However, this concept is equally applied to any other two-port 2D LWA array such as waveguide slot arrays. Previous works on CRLH TL 2D LWA arrays for full-space pencil-beam scanning have been reported in [73], [74], and [75]. However, this is the first work that addresses the efficiency improvement of a CRLH TL 2D LWA array.

This section is organized as follows. Subsection 5.1.1 discusses the concept of cross-recycling to improve the radiation efficiency and gain of LWA array. Subsection 5.1.2 presents the design and simulation results of the proposed high-efficiency LWA array. Subsection 5.1.3 shows the prototype and measured results. Conclusion and future perspective are outlined in subsection 5.1.4.

5.1.1 Concept of Cross Power-Recycling

Principle and Advantages

Fig. 5.1 presents a perspective view of the *cross-recycling* leaky-wave antenna array using series feeding network. The array consists of five CRLH LWA elements, each having a length of ℓ and spacing of d between adjacent elements. The input signal i_0 is applied to the central element of the LWA array at $(x, y) = (0, 0)$ and progressively leaks out as it propagates along the CRLH LWA with a leakage factor α. At the end of the central element $(x, y) = (\ell, 0)$, the remaining power of the input signal is equally divided into two signals i_{+1} and i_{-1} which are fed into adjacent array elements at $(x, y) = (0, d)$ and $(x, y) = (0, -d)$, respectively. Similar to the input signal i_0, the two signals i_{+1} and i_{-1} propagate along the CRLH LWA and radiate with the same leakage factor rate of α. Any power remaining from signals i_{+1} and

i_{-1} at the end of the two array elements is directly recycled into signals i_{+2} and i_{-2} of the adjacent array elements at $(x, y) = (0, 2d)$ and $(x, y) = (0, -2d)$, respectively. The number of array elements N in the y-direction can be extended until most of the input signal power has leaked out before being terminated with matched loads. Alternatively, the array can be made larger both along the x- and y- directions by using power regenerating active elements [76].

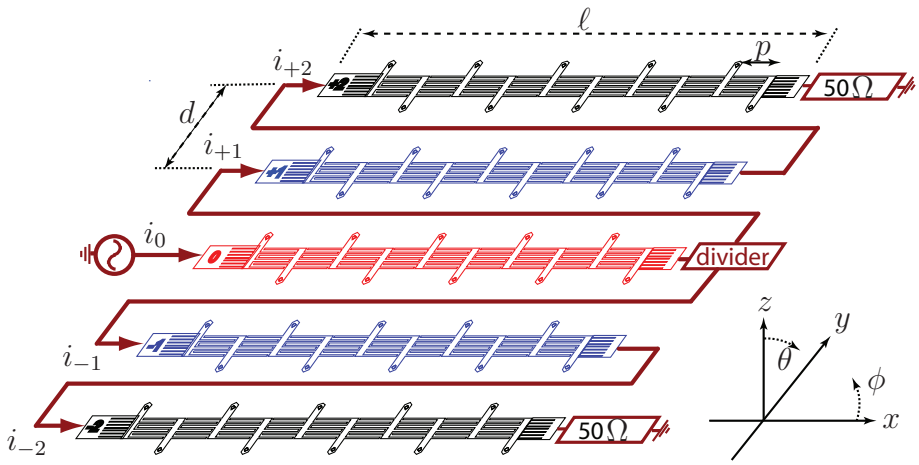

(a) Perspective view.

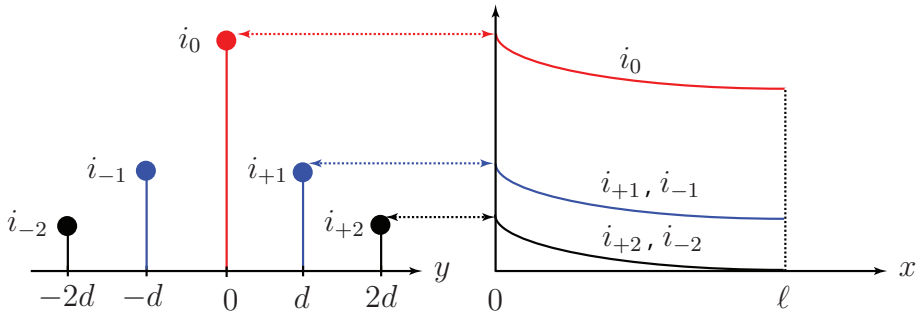

(b) Currents distribution.

Figure 5.1 Proposed CRLH TL LWA array with improved efficiency using a series feeding network for power recycling. (a) Perspective view. (b) Current distribution in x- and y-directions.

Since the LWA is a travelling, two-port antenna, any portion of the input power which does not radiate is dumped into the output load. This is the main cause of low radiation efficiency of conventional LWAs. The proposed power recycling concept used in LWA array provides a remedy to this problem and offers the following three

advantages:

1. High Radiation Efficiency and Gain: As input signal power is efficiently recycled within N elements of the array, a higher level of radiated power (P_{rad}) is achieved for a given input power (P_i). Consequently, high radiation efficiency and gain are obtained. This is in contrast to conventional 2D arrays where increasing the number of array elements *does not* ehance the efficiency or gain [53]
2. Beamwidth control: The half power beamwidth (HPBW) in both the $zx-$ and $zy-$ planes can be conveniently and independently controlled by adjusting the length (ℓ) of each array element and the number (N) of array elements.
3. Simple feeding network: Comparing with a conventional $2D$ array, the series feeding network has a low loss and simple planar design.

Efficiency Approximation

Assuming negligible (compared to radiation) substrate and conductor losses, the radiation efficiency η_{array} can be approximated by taking the ratio of P_{rad}/P_i. The radiated power can be approximated from the currents in the array, which have the following distributions

$$i_0(0,0) = i_0, \tag{5.1a}$$

$$i_{-1}(0,-d) = i_{+1}(0,d) = \frac{i_0(\ell,0)}{2}, \tag{5.1b}$$

$$i_{-2}(0,-2d) = i_{-1}(\ell,-d) = i_{+1}(\ell,d) = i_{+2}(0,+2d), \tag{5.1c}$$

$$i_n(\ell,nd) = i_n(0,nd)e^{-\alpha\ell}, \tag{5.1d}$$

where $n = 0, \pm 1, \pm N$. From (5.1), the current reaching the matched loads can be related to the input current as $i_n(\ell, \pm Nd) = (i_0/2)e^{-(N+1)\alpha\ell}$. The radiation efficiency of the cross-recycling LWA array can then be approximated as

$$\eta_{array} = \frac{P_i - P_L}{P_i} = \frac{i_0^2 - i_{\pm n}^2(\ell, \pm Nd)}{i_0^2} = 1 - \frac{e^{-2(N+1)\alpha\ell}}{2}. \tag{5.2}$$

It can be seen that radiation efficiency can be increased by increasing the length (ℓ) of the CRLH LWA and/or the number of array elements (N). This is demonstrated in the following section.

5.1.2 Design and Simulation

The LWA array is formed by placing 5 CRLH LWAs in the y-direction with an element-to-element spacing of $d = 28$ mm. Each CRLH TL has 14 unit cells with $p = 8.34$ mm. An ideal 3-dB Wilkinson power divider is used to equally divide the power from the central element to the adjacent elements. Ansoft Designer, a MoM software, is used to simulate the design and validate the proposed concept. The simulated radiation patterns and the 2D LWA array performance are illustrated in Fig. 5.2 and summarized in Tab. 5.1. Fig. 5.2(a) shows the zx-plane cut of normalized gain radiation patterns at three frequencies 3.4 GHz, 3.75 GHz and 4.3 GHz illustrating beam-scanning from backward through broadside to forward direction of the LWA with $N = 1$ element. Figs. 5.2(b) and 5.2(c) show the zy-plane cut of normalized gain radiation patterns and the $3D$ plot of input gain at broadside frequency of 3.75 GHz for an array of $N = 1$, 3 and 5 LWA elements.

It can be seen from Tab. 5.1 that the gain and efficiency increase significantly from a single LWA element to LWA array of 3 and 5 elements. Moreover, as the physical array aperture increases from 1 to 5 array elements, the directivity increases by 60% (linear scale) and HPBW reduces substantially by 53% as the beam becomes more directive in the vertical zy-plane. The beamwidth in the horizontal zx-plane remains unchanged.

Table 5.1 Simulated (Ansoft Designer) Gain (G), Directivity (D), Half-Power Beam Width (HPBW) and Efficiency (η_{array}) of the CRLH LWA Array

Number of array elements	G	D	HPBW		η_{array}
			zx-plane	zy-plane	
1	6.84 dB	11.15 dB	30^o	96^o	37.60%
3	10.72 dB	12.53 dB	31^o	62^o	65.89%
5	12.45 dB	13.51 dB	31^o	45^o	78.29%

5.1.3 Experimental Demonstration

Fig. 5.3 shows the fabricated prototype of the array consisting of 5 CRLH LWA elements. The array is fabricated on a Rogers RO3003 substrate with a thickness

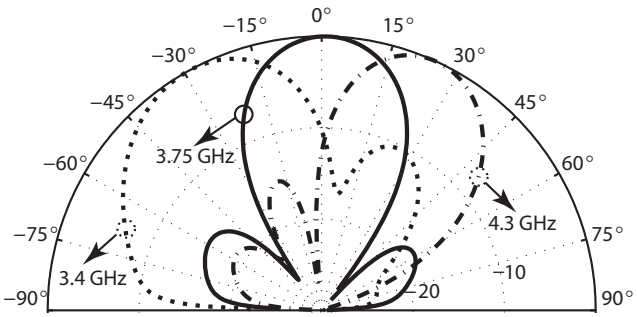

(a) zx-plane cut.

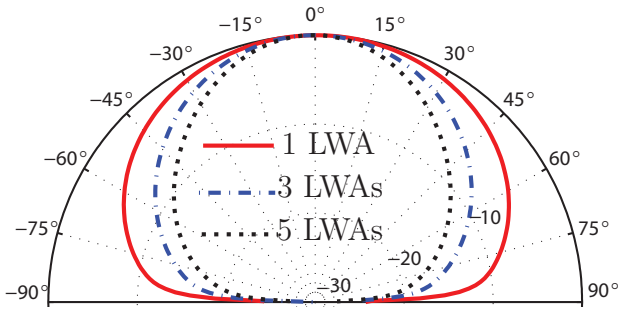

(b) zy-plane cut.

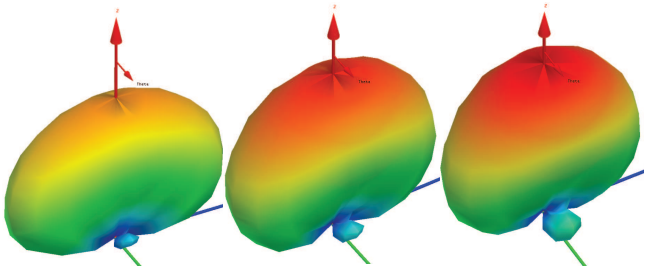

(c) $3D$ Gain Pattern.

Figure 5.2 Simulated radiation patterns using Ansoft Designer software. (a) zx-plane cut of normalized gain radiation patterns at the three frequencies 3.4 GHz, 3.75 GHz and 4.3 GHz illustrating beam-scanning from backward through broadside to forward directions of the CRLH TL LWA with $N = 1$ element. (b) zy-plane cut of normalized gain radiation patterns at broadside frequency of 3.75 GHz for an array of $N = 1$, 3 and 5 TL LWA elements. (c) $3D$ plot of gain radiation pattern for an array of $N =$ 1, 3 and 5 TL LWA elements (from left to right).

of 1.52 mm. A Minicircuit 3-dB power splitter (model ZX10-2-71) is used as the divider. To ensure the input of one CRLH LWA element is in phase with that of the

next section, the phase delay of the coaxial cable connecting these elements is adjusted to be a multiple of 2π at the operating frequency. The two last array elements are terminated with matched 50 Ω loads. The LWA array physical area is 13.6 cm x 16.6 cm = 225.76 cm^2.

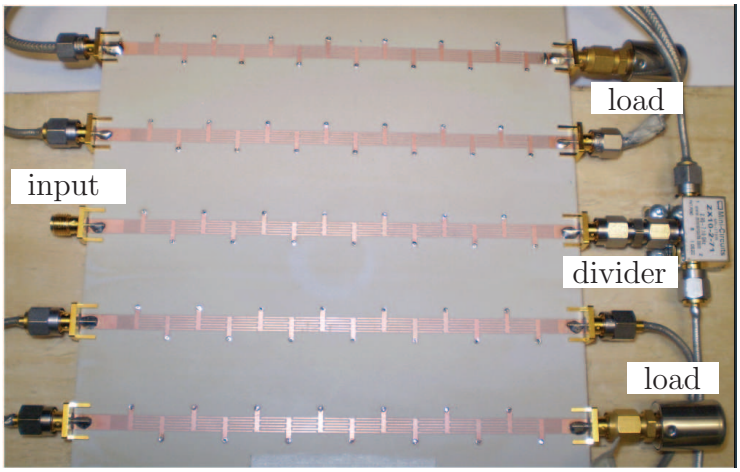

Figure 5.3 Prototype of the CRLH LWA array with improved efficiency using a series feeding network for power recycling.

Fig. 5.4 shows measured insertion loss and return loss of the antenna prototype for $N = 1$, 3, and 5 elements. The monotonic decrease in the insertion loss level within the leaky-wave passband of 3 - 4.5 GHz indicates less input power reaching the loads, and therefore more radiated power. The return loss remains below -15 dB within the passband but increases slightly as the array elements grow from $N = 1$ to 5. This is possibly due to the mismatch and reflection from the power divider and cables connecting adjacent elements.

The measured radiation patterns are shown in Fig. 5.5 and the array's performances are summarized in Tab. 5.2 along with simulated results. Fig. 5.5(a) shows the horizontal zx-plane cut of normalized radiation patterns at three frequencies 3.4 GHz, 3.75 GHz and 4.3 GHz illustrating beam-scanning from backward through broadside to forward direction. In comparison with Fig. 5.2(a), the measured patterns match well with the full-wave simulated results.

Figs. 5.5(b) and 5.5(c) show the measured (red and dashed line) and simulated (black and solid line) radiation patterns at the broadside frequency of 3.75 GHz. In the horizontal zx-plane, Fig. 5.5(b) indicates an excellent agreement between mea-

surement and simulation. The slight shift of the peak observed in the measured pattern is most likely caused by measurement error in antenna alignment.

Fig. 5.5(c) shows the results in the vertical zy-plane. The measured beam has a narrower HPBW of 36.42^o compared to the full-wave simulation of 45^o. In addition, the measured beam does not have a symmetrical pattern as seen in the full-wave simulation. Due to the narrower HPBW in the vertical zy-plane, the measured directivity, approximated as $32,400/(\text{HPBW}_{zx}\text{HPBW}_{zy})$ [53], is 14.57 dB and is higher than the simulated directivity of 13.51 dB. As a consequence, the measured radiation efficiency, approximated by $\eta = G/D$, reduces to 60.06% instead of 78.29% observed in full-wave simulation. This discrepancy is most likely contributed by unequal cable losses and unbalanced output ports' magnitude and phase of the discrete power divider. The effective area, given as $G\lambda^2/4\pi$ [53], computed at the broadside frequency of 3.75 GHz is 87.50 cm^2. The aperture efficiency of the LWA array, computed by taking the ratio of effective area to physical area, is 87.50/225.76 = 38.75%. This aperture efficiency can be used to compute the total efficiency when the 2D LWA array operates in the receiving mode.

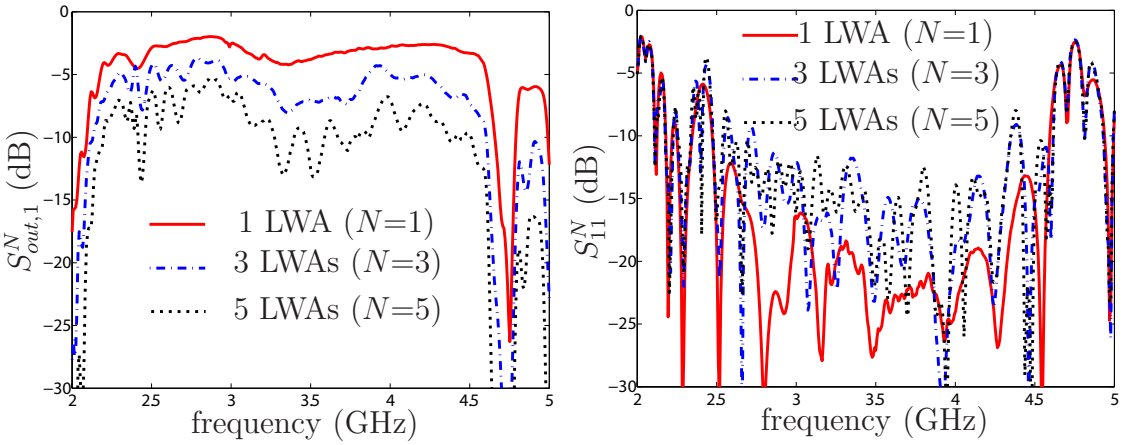

(a) Insertion loss.

(b) Return loss.

Figure 5.4 Measured S-parameters of the CRLH TL LWA array with 1, 3, and 5 elements. (a) Insertion loss $S^N_{out,1}$. (b) Return loss S^N_{11}.

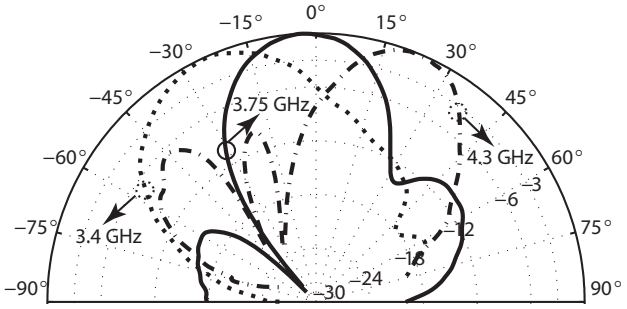

(a) zx-plane cut.

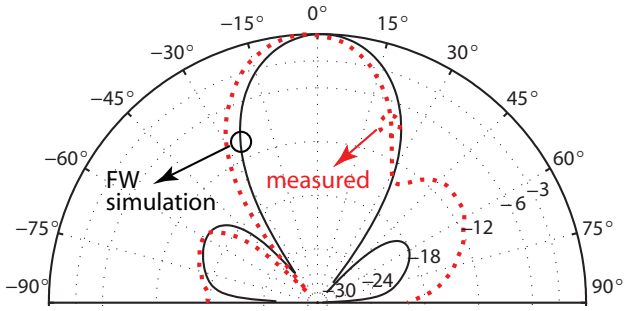

(b) zx-plane cut at broadside frequency.

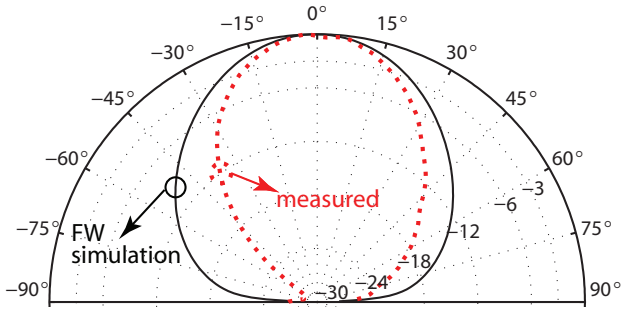

(c) zy-plane cut at broadside frequency.

Figure 5.5 Measured radiation pattern of the LWA array prototype of Fig. 5.3. (a) zx-plane cut of normalized gain radiation patterns at three frequencies 3.4 GHz, 3.75 GHz and 4.3 GHz illustrating beam-scanning from backward through broadside to forward direction. (b) zx-plane cut at broadside frequency 3.75 GHz superimposed with Ansoft Designer simulated result. (c) zy-plane cut at broadside frequency 3.75 GHz superimposed with Ansoft Designer simulated result.

5.1.4 Conclusions

The cross power-recycling concept using a series feeding network has been introduced and applied to a CRLH TL 2D LWA array to enhance its radiation efficiency. The proposed concept efficiently recycles power between array's elements and enhances both the antenna's radiation efficiency and directivity as a function of the number of array's elements N. As the result, the array's gain, which is the product of the radiation efficiency and directivity, is enhanced significantly. In comparison with a single CRLH TL LWA, the fabricated 5-element CRLH TL 2D LWA array provides a twofold and fourfold enhancement in radiation efficiency and gain, respectively. The CRLH TL 2D LWA array provides a frequency-scanning main beam in the horizontal plane. This array can be conveniently extended to provide vertical scanning capability by adding phase shifters between array elements.

Table 5.2 Gain, Directivity, Half-Power Beam Width (HPBW) and Efficiency of the CRLH TL LWA array with $N = 5$ elements operating at 3.75 GHz.

	Simulation	Measurement
G	12.45 dB	12.35 dB
D	13.51 dB	14.57 dB
HPBW in zx-plane	31.00^o	31.06^o
HPBW in zy-plane	45.00^o	36.42^o
η_{array}	78.29%	60.06%

5.2 Article 7: Power-recycling Feedback System for Maximization of Leaky-wave Antennas Radiation Efficiency

The previous section presented a high efficiency CRLH LWA array using a power-recycling series feeding network. This antenna was a 2D array, which cross-recycled the power left at the output of the center element into the input of the neighboring elements and then further recycling the power left at the output of these neighbors into the next adjacent elements. Using this *cross-recycling* mechanism, the overall antenna with five elements reached a radiation efficiency more than twice that of a single antenna element. However, this approach for efficiency enhancement is applicable only to an 2D LWA array and not to a single LWA.

The present section introduces a novel power-recycling scheme which maximizes the radiation efficiency of any single LWA, by using a *self-recycling* mechanism, where the non-radiated power at the end of the LWA is fed back into the input of the antenna itself. Such a power-recycling system may enhance the radiation efficiency of any LWA to 100% in a lossless system. Although a 100% efficiency cannot be achieved in a practical lossy system, the proposed mechanism provides a significant radiation efficiency enhancement.

A similar power-recycling technique was reported in an optical system for a gravitational-wave antenna in [77]. In this antenna, a partially transmitting mirror is used to recycle the light power back into the main interferometer in order to increase the effective power and hence enhance the power-gain of the system. At microwaves, a LWA having its output connected back to its input, so as to form a self-oscillating antenna, was reported in [78]. However, this system, as an oscillator, does not have any input port and therefore cannot transmit a modulated signal. Moreover, the amount of radiated power cannot be controlled and no attempt was made to enhance the radiation efficiency in this self-oscillating antenna.

Thus, the proposed power-recycling LWA system constitutes a unique solution for efficiency enhancement of LWAs. Using this system, a LWA may provide an optimal solution for applications where a trade-off between directivity and size exists. For instance, a LWA of the length in the order of $1 - 3\lambda_0$ may exhibit a directivity and gain significantly larger than that of a $\lambda_0/2$ resonant antenna, while avoiding the

complexity of a conventional antenna array.

This work considers only the case of fixed broadside radiation, where the main benefit of the power-recycling system is radiation efficiency enhancement. However, the structure may be refined and incorporate real-time tuning phase shifters in order to provide beam scanning in addition.

5.2.1 Concept of Self Power-Recycling

Fig. 5.6 shows the schematic of a conventional LWA of length ℓ terminated with a matched load Z_L. This antenna has a propagation constant β and an attenuation constant α, which includes in general both leakage and ohmic/dielectric/mismatch loss. We consider here a harmonic excitation with voltage V_i. The input wave propagates along the LWA structure and, when it is faster than light (i.e. at frequencies where $\beta < k_0$), it progressively leaks out to the free space to build up a radiating beam at the angle $\theta = \sin^{-1}(\beta/k_0)$. The remaining power at the end of the LWA is absorbed by the matched load Z_L, and may be related to the input power P_i as $P_L = P_i e^{-2\alpha\ell}$. Therefore, the radiation efficiency of the LWA reads [72]

$$\eta_0 = \frac{P_{rad}}{P_i} = \frac{P_i - P_L - P_{loss}}{P_i} = 1 - e^{-2\alpha\ell}, \tag{5.3}$$

where a lossless structure has been assumed in the second equality, i.e. $P_{loss} = 0$, for the sake of simplicity. In this case, the attenuation constant α is solely due to leakage and reduces exactly to the leakage factor.

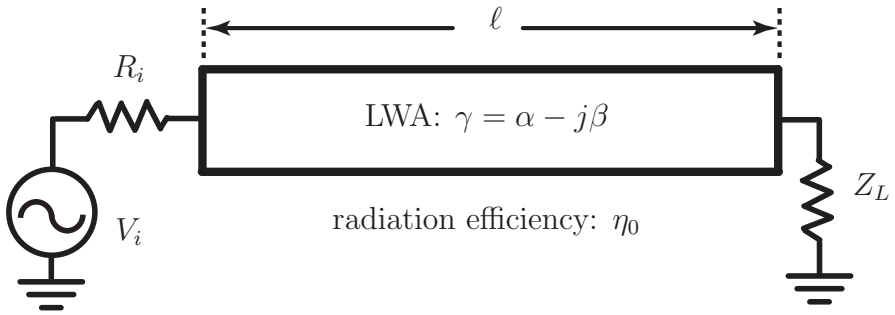

Figure 5.6 Schematic of a conventional leaky-wave antenna (LWA) terminated with a matched load Z_L.

According to (5.3), in order to increase the radiation efficiency of a LWA to a maximum level, one needs to increase its length until almost all of the input power [typically 90% [72]] has been radiated. This results in enhanced directivity, due to increased radiation aperture, but may also imply an excessively large size, which is generally prohibitive toward low frequencies. Consequently, LWAs are typically designed with lengths for which a substantial fraction of the input power reaches its output and is lost in the load, leading to a low radiation efficiency.

Fig. 5.7 shows the proposed power-recycling LWA system, which provides a remedy to this fundamental efficiency problem, by recycling the non-radiated power at the end of the antenna back into its input. This system incorporates an ideal adder in a feedback loop of the LWA, which sums the applied input and recycled signals. The resulting signal that appears at the input of the LWA has a larger amplitude than the applied input signal for a non-zero recycled signal. As a result, the radiated power of the power-recycling LWA system is increased compared to the case of the open-loop LWA, and hence the radiation efficiency of the feedback system, η_s, is superior to that of the open-loop (isolated) LWA, $\eta_s > \eta_0$.

The adder in Fig. 5.7 may be realized by a Wilkinson combiner (a three-port network) or by a 180° hybrid coupler (a four-port network) under the form of a rat-race, a tapered coupled-line coupler, or a magic-T [42]. As will be seen in subsection 5.2.2, the adder will need to accommodate different power combining ratios depending on the open-loop LWA efficiency η_0. In the case of the Wilkinson combiner, this would require impedance transformers for matching to a system of impedance Z_0 at two output ports [42]. Therefore, the 180° hybrid option was preferred in this work. Specifically, we chose the rat-race, because the conventional magic-T is non-planar and the tapered coupled-line coupler is harder to design and suffers from limited coupling levels.

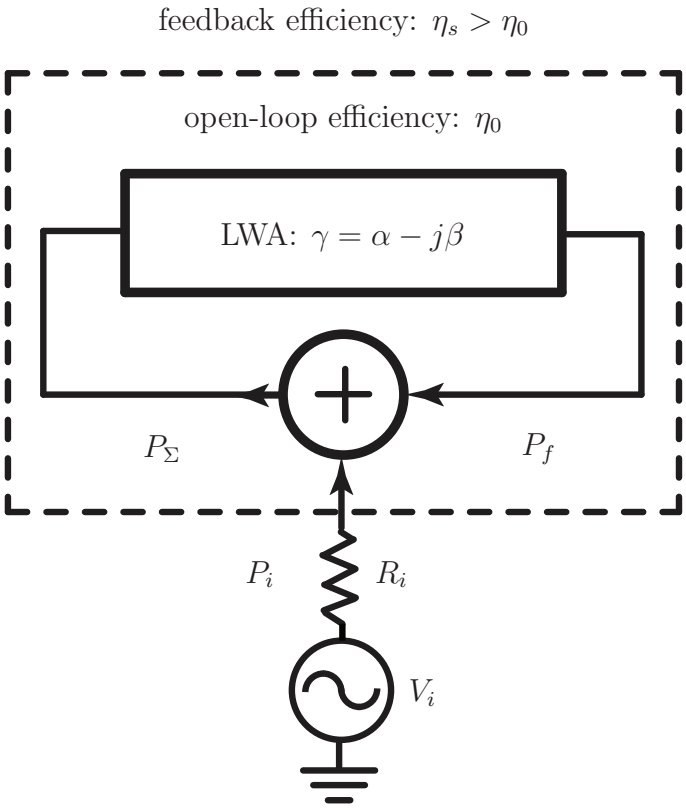

Figure 5.7 Proposed power-recycling LWA system.

5.2.2 System Configuration and Theoretical Demonstration

This section demonstrates and characterizes the rat-race based power-recycling LWA system using a scattering parameter approach, first for a LWA of arbitrary radiation efficiency η_0 and then specifically for the case of a 3-dB LWA system, corresponding to a LWA efficiency of $\eta_0 = 0.5$.

Rat-race System Implementation and Principle of Operation

Fig. 5.8 shows the rat-race based implementation of the power-recycling LWA system of Fig. 5.7, along with the port and wave voltage notations that will be used in this forthcoming analysis. Two TLs, ℓ_{45} and ℓ_{63}, have been added in the feedback loop to provide the proper phase condition for maximal system efficiency η_s. The difference port is terminated by a matched load Z_L.

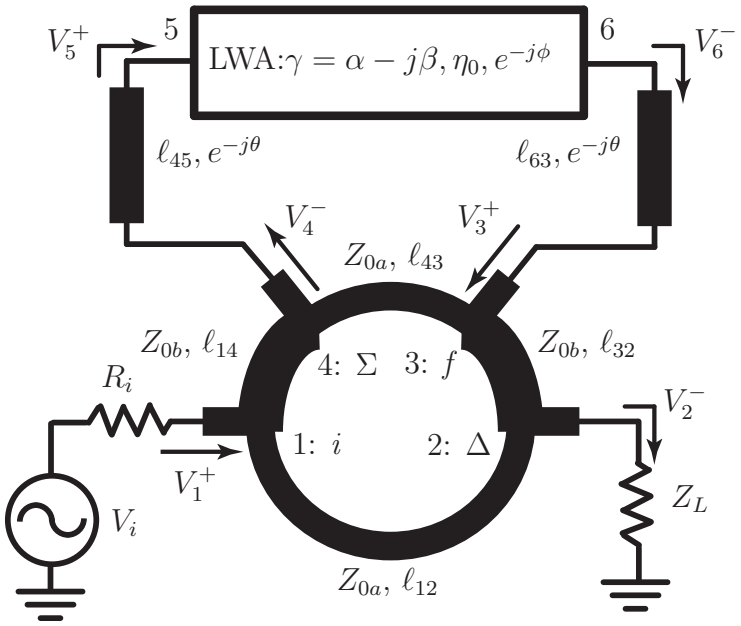

Figure 5.8 Rat-race based implementation of the power-recycling LWA system shown in Fig. 5.7. In general, the rat-race exhibits different power combining ratios, corresponding to two sets of impedances (Z_{0a} and Z_{0b}), depending on the open loop-efficiency η_0 of the LWA. Notation for the 180^o hybrid ports: i: input, f: feedback, Σ: sum, and Δ: difference.

In order to provide arbitrary power combining ratios, the rat-race includes two sets of TL sections, with respective impedances $Z_{0a} = Z_0/a$ and $Z_{0b} = Z_0/b$, as shown in Fig. 5.8, where a and b are positive real numbers satisfying the relation $a^2 + b^2 = 1$ for perfect isolation between the two coupled ports (ports 1 and 3) [79]. The resulting scattering matrix [S] reads

$$\begin{bmatrix} V_1^- \\ V_2^- \\ V_3^- \\ V_4^- \end{bmatrix} = \begin{bmatrix} 0 & ja & 0 & -jb \\ ja & 0 & -jb & 0 \\ 0 & -jb & 0 & -ja \\ -jb & 0 & -ja & 0 \end{bmatrix} \begin{bmatrix} V_1^+ \\ V_2^+ \\ V_3^+ \\ V_4^+ \end{bmatrix}, \tag{5.4}$$

where V_i^+ and V_i^- $(i = 1, 2, 3, 4)$ represent the incident and reflected voltages of port i, respectively.

The power-recycling LWA system operates as follows. The rat-race coupler constructively adds the input (i, port 1) and recycled or feedback (f, port 3) signals

at its sum port (Σ, port 4), toward the input of the LWA, while using its difference port (Δ, port 2) for matching in the steady-state regime and for power regulation in the transient regime, as will be shown later. In addition, it provides perfect isolation between the input and feedback ports, which ensures complete decoupling between the corresponding signals. Via this *positive* (i.e. *additive*) feedback mechanism, the power appearing at the input of the LWA progressively increases during the transient regime until it reaches its steady-state level, leading to a theoretical system radiation efficiency of 100%, as will be demonstrated next.

Demonstration of Radiation Efficiency Enhancement

Let us consider again throughout this section, without loss of generality, the case of a lossless system (no ohmic, dielectric and mismatch losses). The actual losses will be automatically taken into account and will be discussed in the experimental demonstration (subsection 5.2.4). It will be shown that in such a lossless system, the efficiency of the system, η_s, can be enhanced to 100%. Essentially, assuming that the rat-race within the system is matched at the input (source) port, this will be achieved when the rat-race is designed so as to nullify the power at the difference (load) port, i.e. $V_2^- = 0$.

We may then write

$$V_2^- = S_{21}V_1^+ + S_{23}V_3^+ = 0. \tag{5.5}$$

This expression can be transformed as follows

$$\begin{aligned} 0 &= S_{21}V_1^+ + S_{23}V_3^+ \\ &= S_{21}V_1^+ + S_{23}e^{-j2\theta}e^{-j\phi}\sqrt{1-\eta_0}V_4^- \\ &= S_{21}V_1^+ + S_{23}e^{-j(2\theta+\phi)}\sqrt{1-\eta_0}(S_{41}V_1^+ + S_{43}V_3^+). \end{aligned} \tag{5.6}$$

In the last expression, V_3^+ may be expressed as a function of V_1^+ using (5.5), i.e. $V_3^+ = -S_{21}/S_{23}V_1^+$, which yields, with $V_1^+ \neq 0$,

$$S_{21} + S_{23}e^{-j(2\theta+\phi)}\sqrt{1-\eta_0}\left(S_{41} - \frac{S_{21}}{S_{23}}S_{43}\right) = 0. \tag{5.7}$$

Substituting the scattering parameters of the rat-race, given by (5.4), into this relation yields

$$ja = \sqrt{1-\eta_0}e^{-j(2\theta+\phi)}, \tag{5.8}$$

which finally provides the sought conditions for $\eta_s = 100\%$, taking into account the rat-race relation $a^2 + b^2 = 1$,

$$a = \sqrt{1-\eta_0} \quad \text{and} \quad b = \sqrt{\eta_0}, \tag{5.9a}$$

$$\theta = -\frac{\phi}{2} + \frac{3\pi}{4} + m\pi, \quad (m \in \mathbb{N}). \tag{5.9b}$$

Equation (5.9a) gives the impedances of the TL sections building the rat-race, while (5.9b) gives the required length of the two TLs building the feedback loop (Fig. 5.8). Fig. 5.9(a) plots the values of a and b with respect to the open-loop LWA radiation efficiency η_0. When $\eta_0 = 0.5$, corresponding to 50% efficiency, $a = b = 1/\sqrt{2} = 0.707$, which corresponds to a 3-dB (equal power combining) rat-race. This particular case will be demonstrated by circuital, full-wave and experimental results in the next two subsections.

When the conditions of (5.9a) and (5.9b), which are the conditions for $V_2^- = 0$ (5.5), are met, the radiation efficiency of the power-recycling LWA system reads, following (5.3),

$$\begin{aligned} \eta_s &= \frac{P_{rad}}{P_i} = \frac{P_i - P_L}{P_i} = \frac{P_1 - P_2}{P_1} = 1 - \frac{P_2}{P_1} \\ &= 1 - \left(\frac{V_2^-}{V_1^+}\right)^2 = 1 - \left(\frac{0}{V_1^+}\right)^2 = 1 \quad \text{or} \quad 100\%. \end{aligned} \tag{5.10}$$

It is useful to relate the radiation efficiency of the system to that of the open-loop LWA. For this purpose, let define here a system *power-recycling gain* G_s as $G_s = P_4/P_1$, or

$$\begin{aligned} \sqrt{G_s} &= \frac{V_4^-}{V_1^+} = \frac{S_{41}V_1^+ + S_{43}V_3^+}{V_1^+} \\ &= S_{41} + S_{43}\frac{V_3^+}{V_1^+} = S_{41} - S_{43}\frac{S_{21}}{S_{23}}. \end{aligned} \tag{5.11}$$

From this equation, the relation between η_s and η_0 is found to be

$$\begin{aligned}\eta_s &= \frac{P_{rad}}{P_i} = \frac{P_{rad}}{P_5}\frac{P_5}{P_4}\frac{P_4}{P_i} \\ &= \eta_0 \left(\frac{V_5^+}{V_4^-}\right)^2 \left(\frac{V_4^-}{V_1^+}\right)^2 = \eta_0 \cdot 1 \cdot G_s = \eta_0 G_s.\end{aligned} \tag{5.12}$$

Inversely, the power-recycling gain can be expressed as a function of the open-loop and system efficiencies

$$G_s = \frac{\eta_s}{\eta_0} > 1, \tag{5.13}$$

which reduces to $G_s = 1/\eta_0$ for 100% system radiation efficiency in the lossless case. This relation expresses the fact that, to reach a given overall efficiency η_s, the system must provide a gain G_s inversely proportional to the open-loop LWA and exactly equals to η_s/η_0. In other words, as $\eta_s = G_s\eta_0$, the efficiency of the open-loop (isolated) LWA has been increased by a factor G_s in the power-recycling system. Equation (5.13) is plotted in Fig. 5.9(b) for $\eta_s = 1$.

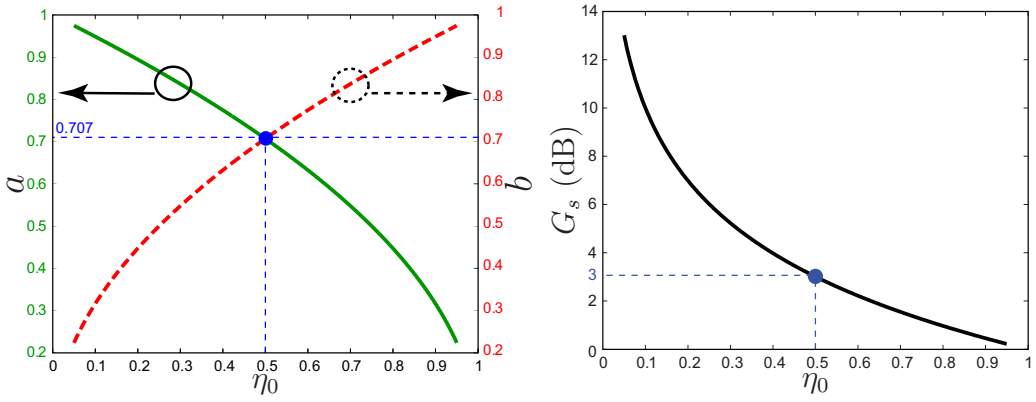

(a) (b)

Figure 5.9 Design and performance of the power-recycling system versus the open-loop (isolated) LWA radiation efficiency η_0 for 100% (lossless) LWA system efficiency ($\eta_s = 1$). a) Normalized impedances a and b of the rat-race (see Fig. 5.8) computed by (5.9a). b) Power-recycling gain G_s computed by (5.13).

It may seem shocking at the first glance that "gain" is produced by a purely passive system. However, this "gain" is not a gain in the sense of an active amplifier

gain, where energy is added into the system by an external DC source, resulting in a system output power P_{out} larger than the input power P_i, $P_{out} = GP_i > P_i$. Here, the role of the "external source" is contributed by the feedback loop, but this source is external only with respect to the rat-race, which effectively sees two power sources (ports 1 and 3). *From the view point of the rat-race*, this leads to a larger power at the input of the LWA (P_Σ) compared to the power at the input of the system (P_i), $P_\Sigma = G_s P_i > P_i$, hence the analogy with an active system. However, no energy has been added to the *overall system* and no more power is radiated than the power provided by the source, as seen in (5.10), where the maximum radiated power P_{rad} cannot exceed the source power P_i, but at best equals it in the case of a perfectly lossless power-recycling system. Exact insight into the the power-recycling mechanism will be automatically gained in the specific results presented in subsections 5.2.3 and 5.2.4.

Particular Case of a 3-dB Broadside System

According to (5.9a), a 3-dB power-recycling LWA system corresponds to a 3-dB (equal power combining) rat-race, $a = b = 1/\sqrt{2}$, and a LWA having an open-loop radiation efficiency of 50% (i.e. $\eta_0 = 0.5$). In addition, we consider here the case of broadside radiation, which corresponds to $\phi = 0$ in (5.9b). In order to demonstrate the radiation efficiency enhancement in a practical implementation, an open-loop LWA and a 3-dB power-recycling system were designed and simulated using MoM (Ansoft Designer).

Fig. 5.10(a) shows the transmission parameter S_{21} of both the open-loop LWA and the power-recycling LWA system. The antenna is an interdigital/stub CRLH LWA with the design parameters given in the caption of the figure. The transmission level has been reduced from -3 dB for the open-loop LWA to -18 dB for the power-recycling LWA system. This indicates that the power at port 2, which is usually wasted in the load in the conventional open-loop LWA, has been nullified in the power-recycling LWA system. This conventionally lost power is now recycled back into the input of the LWA to increase the overall system radiation efficiency. The transient role of the matched load at the Δ port will be explicated in the time domain analysis of subsection 5.2.3.

Fig. 5.10(b) shows the radiation efficiency of the open-loop LWA and the power-recycling LWA. The open-loop (or isolated) LWA has an efficiency close to 50%,

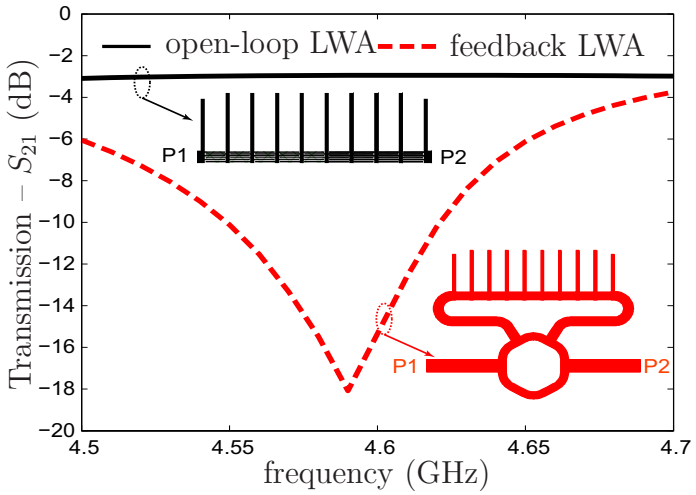

(a)

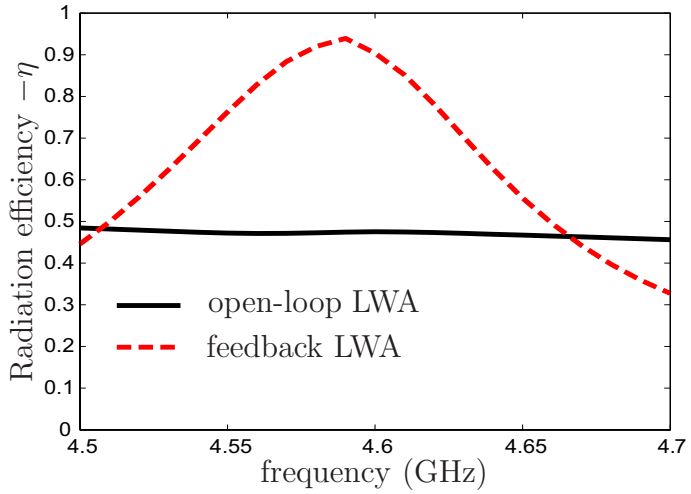

(b)

Figure 5.10 Full-wave (MoM, Ansoft Designer) demonstration of a 3-dB power-recycling LWA system designed at 4.58 GHz in the lossless case (neither ohmic nor dielectric losses), comparing the open loop LWA (Fig. 5.6) and the power-recycling LWA (Fig. 5.8). The LWA is an interdigital/stub CRLH LWA [4] with the parameters: number of unit cells: $N = 10$, unit cell length: $p = 208$ mils, number of fingers: $N_f = 6$ (3 pairs), finger width: $w = 15$ mils, inter-finger gap: $g = 6$ mils (everywhere), stub width: $w_{stub,1} = 39$ mils, length of first and last stubs: $L_{stub,2} = 580$ mils, length of other stubs: $L_{stub} = 644$ mils, substrate thickness: $h = 62$ mils, substrate permittivity: $\varepsilon_r = 2.2$. a) S-parameters. b) Radiation efficiency.

resulting typically from a tradeoff between directivity or gain and size. With the power-recycling system, the efficiency of the LWA has been enhanced to a value of 95%, very close to the ideal case of 100%. Further matching optimization, would certainly further increase this performance. In this simulation, ohmic and dielectric have been set to zero, in order to validate the fundamental theory of this section, and the difference from 95% to 100% is therefore due exclusively to minor mismatches across the system. These results provide an idea of the maximum possible efficiency enhancement, using high-quality substrates. The actual enhancement attainable in practical implementation with a commercial substrate will be demonstrated experimentally in subsection 5.2.4.

Finally, Tab. 5.3 quantifies the impact of deviations from the conditions of (5.9) in terms of sum-port power, P_Σ, and system efficiency, η_s, for a 3-dB power-recycling system, with an input power of $P_i = 0$ dBm. The center of the table indicates the optimal case considered above where the LWA exhibits exactly 3 dB attenuation (which may also include all possible losses), yielding $\eta_s = 100\%$, and also $P_\Sigma = 3$ dBm, which is twice the power at the input port, consistently with $P_\Sigma = G_s P_i$, where G_s is given by (5.11) and shown to be equal to 3 dB in Fig. 5.9(b) for $\eta_0 = 0.5$. Moving horizontally the table from this point shows the effect of a deviation from a 3 dB attenuation in the LWA, which is a reduction of both P_Σ and η_s, as may have been expected since conditions (5.9) are not exactly satisfied any more. Ohmic, dielectric and mismatch losses would naturally tend to increase the attenuation, toward the right side of the table. Moving vertically in the table from the center row shows the effect of a deviation from a $3\pi/4 + m\pi$ phase in feedback loop TLs, which is again a reduction of both P_Σ and η_s. What is most important to note is that deviations do *not* ruin the performances of the power-recycling LWA system but only degrade them progressively as they increase.

5.2.3 Build-up of the Waveforms from the Transient to the Steady-state Regimes

The transient operation of the power-recycling LWA system may not be obvious from the previous descriptions. For instance, it is not clear how the power can build up to produce of power at the sum port which becomes twice that of the input port. It is the purpose of the present section to clarify and illustrate the transition of the

Table 5.3 Harmonic balance (Agilent ADS) sensitivity analysis for a 3-dB power-recycling LWA (Fig. 5.8) using an ideal rat-race, ideal TLs of length θ, and modeling the LWA by an attenuator. $\Delta\theta$ is the deviation from the desired feedback phase θ, given in (5.9b). The input power is $P_i = 0$ dBm and the power P_Σ is given in dBm.

	2.7-dB LWA	3.0-dB LWA	3.3-dB LWA
$\Delta\theta = -15^o$	$P_\sum = 3.18$ $\eta_s = 96.3\%$	$P_\sum = 2.87$ $\eta_s = 97.0\%$	$P_\sum = 2.59$ $\eta_s = 96.6\%$
$\Delta\theta = 0^o$	$P_\sum = 3.33$ $\eta_s = 99.7\%$	$P_\sum = 3$ $\eta_s = 100\%$	$P_\sum = 2.73$ $\eta_s = 99.8\%$
$\Delta\theta = +15^o$	$P_\sum = 3.17$ $\eta_s = 96.1\%$	$P_\sum = 2.87$ $\eta_s = 97.0\%$	$P_\sum = 2.59$ $\eta_s = 96.6\%$

system from the transient to the steady-state regimes. It will be seen that power is irreversibly dissipated in the load of the Δ port in the transient regime. However, the proposed system is intended to operate in the steady-state regime, where the switch-on transient regime is safely considered a negligible ratio of the operation duration of the antenna system. The efficiencies of subsection. 5.2.2 naturally refer to the steady-state regime. Without loss of generality, this section considers the particular case of a 3-dB power-recycling LWA system.

Mathematical Calculation of Powers

To first gain a quick and basic intuitive perception of the transient response, let us consider a simplified mathematical model of the system, neglecting frequency and exact propagation delay consideration. In reference to Fig. 5.8, we excite the system by an input signal $P_i = 0$ dBm $= 1$ mW, which corresponds to the initialization $V_i = \sqrt{2Z_0P_i} = 0.316$ V and $V_f = 0$ V. From this point, the voltages V_Σ, V_Δ and V_f may be computed versus the number of passes of the signal across the feedback loop using the following algorithm:

$$
\begin{aligned}
V_\Sigma &= \frac{V_i + V_f}{\sqrt{2}} \\
V_\Delta &= \frac{V_i - V_f}{\sqrt{2}} \\
V_f &= \frac{V_\Sigma}{\sqrt{2}}.
\end{aligned}
\tag{5.14}
$$

The resulting powers are listed in Tab. 5.4. Initially, before the signal had time to penetrate into the feedback loop (so that the loop is invisible to the rat-race), the input power equally splits between the Σ and Δ ports. After the first pass, the signal appears at the feedback (f) port, thereby more than doubling P_Σ slightly beyond P_i. At this time, a significant amount of power (around -9 dB $= 0.125$ mW) is still present at the Δ port, since P_i and P_f are still very different. As the number of passes increases, we have $P_f \to P_i$, $P_\Sigma \to 2P_i$ (as predicted in the steady-state analysis of subsection 5.2.2) and $P_\Delta \to 0$ mW. This shows that the Δ port act as a power regulator. Initially, its load Z_L absorbs the excess power $P_i - P_f$, until P_f has reached the level of P_i, which corresponds to the steady-state regime, where it serves only for matching.

Circuit Simulation of Instantaneous Power Waveforms

The algorithm of the previous section was an oversimplified model of the actual power-recycling LWA system. Let us now perform rigorous circuit simulation, exactly taking into account frequency and propagation delays across the rat-race and the feedback loop. In this simulation, the only simplifications will be the modeling of the LWA by an attenuator, the utilization of an ideal model for the rat-race, and the absence of loss. The excitation frequency is arbitrarily chosen as 1 GHz, corresponding to harmonic period of $T = 1/f = 1$ ns, and the source power was set to 1 mW.

Fig. 5.11 shows the transient evolution of the *instantaneous powers* at the ports i, Σ, f and Δ. The source is switched on at $t = 0$. Therefore, at this time, the corresponding power P_i is immediately present, whereas it did not have time to reach the other ports. Next the wave splits into two waves toward the left and the right of the input port along the rat-race. The times for the waves to reach the Σ, f

Table 5.4 Transient behavior of the ideal (no loss, no delays) 3-dB power-recycling LWA system of Fig. 5.8, computed by (5.14). Passes refer to passes of the wave across the LWA from the onset of the system. The power levels are in dBm and $P_i = 0$ dBm.

Time	P_i	$P_\sum$	P_f	P_Δ
Pass 0	0	-3.01	—	-3.01
Pass 1	0	0.51	-6.02	-9.03
Pass 2	0	1.85	-2.50	-15.05
Pass 3	0	2.45	-1.16	-21.07
Pass 4	0	2.73	-0.56	-27.09
Pass 5	0	2.87	-0.28	-33.11
Pass 6	0	2.94	-0.14	-39.13
Pass 7	0	2.98	-0.07	-45.15
Pass 8	0	2.99	-0.03	-51.18
Pass 9	0	3.00	-0.02	-57.20

and Δ ports are $t_\Sigma = T/4 = 0.25$ ns, $t_f = T/2 = 0.5$ ns, and $t_\Delta = 3T/4 = 0.75$ ns, respectively. After these times, the exact transient behavior of the signal, which lasts here for around 5 ns, can be observed on the curves, in agreement with the prediction of Tab. 5.4. Initially, P_i is slightly varying, and stabilizes to its nominal value of 1 mW only after the steady-state regime has been reached. This is because, at early times, the wave entering into the system does not see the other ports. Matching, as defined by scattering parameters, is valid only in the steady-state regime. P_Σ increases progressively to finally reach $2P_i$ =2 mW. P_f starts with a negative cycle. This is due to the fact that during this time, $t_f < t < T$, the wave traveling in the lower arm of the rat-race toward the f port has not reached this port yet so as to cancel out with the wave traveling in the upper arm; in fact, the lower-arm wave is reaching the f port only at time T. From that time, P_f grows to stabilize at the same level of the input power, $P_i = 1$ mW, in the steady-state regime. Finally, P_Δ quickly decays from t_Δ to fully vanish, as expected from satisfaction of the system's conditions (5.9).

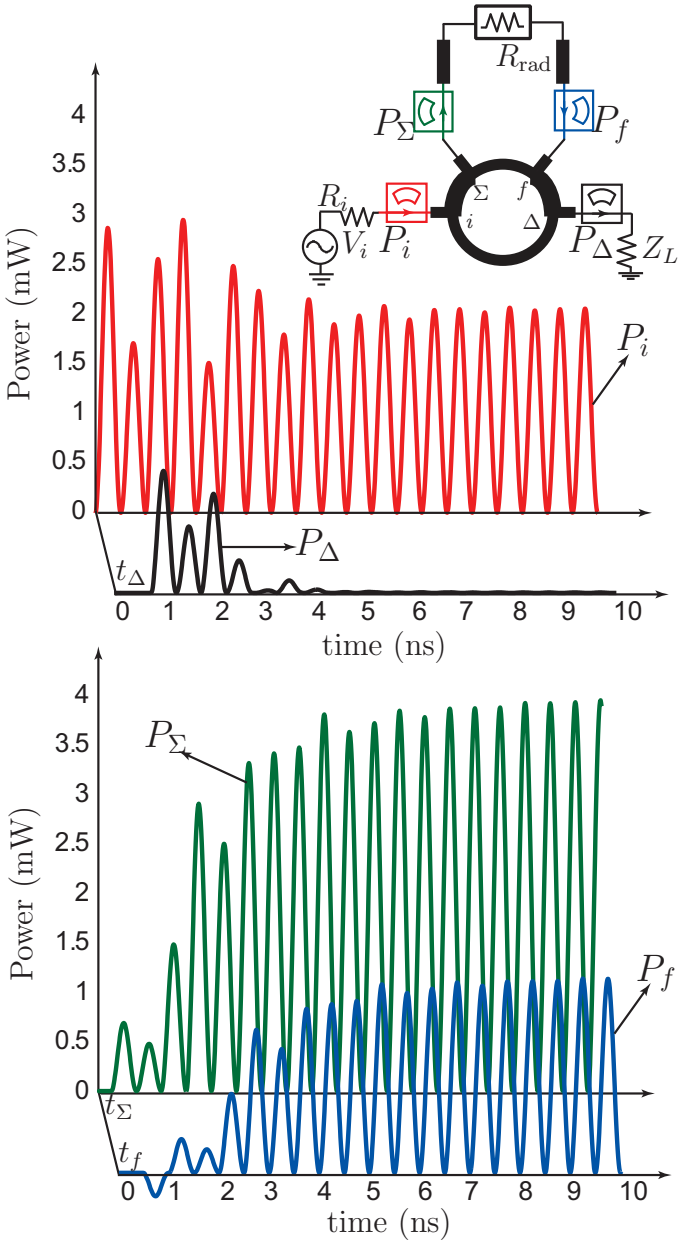

Figure 5.11 Transient response (Agilent ADS) of the 3-dB power-recycling LWA system of Fig. 5.8, using an ideal rat-race coupler, ideal feeding TLs of length $\ell_{45} = \ell_{63} = 3\pi/4$, and a 3-dB resistive attenuator. The system is excited by a 1 GHz harmonic source of peak voltage $V_i = 0.316$ V (0 dBm in a 50 Ω system).

Full-wave Simulation of Electromagnetic Fields

The transient electromagnetic field distributions are plotted in Fig. 5.12 for the 3-dB power-recycling LWA system of Fig. 5.8 with parameters of Fig. 5.10. These

results are self-explanatory. The evolution of the system from the transient to the steady-state regime can be followed step by step by using the same description the previous paragraph (ignoring the numerics). Optimal understanding of the system's operation may be gained by considering in parallel the results of Figs. 5.11 and 5.12.

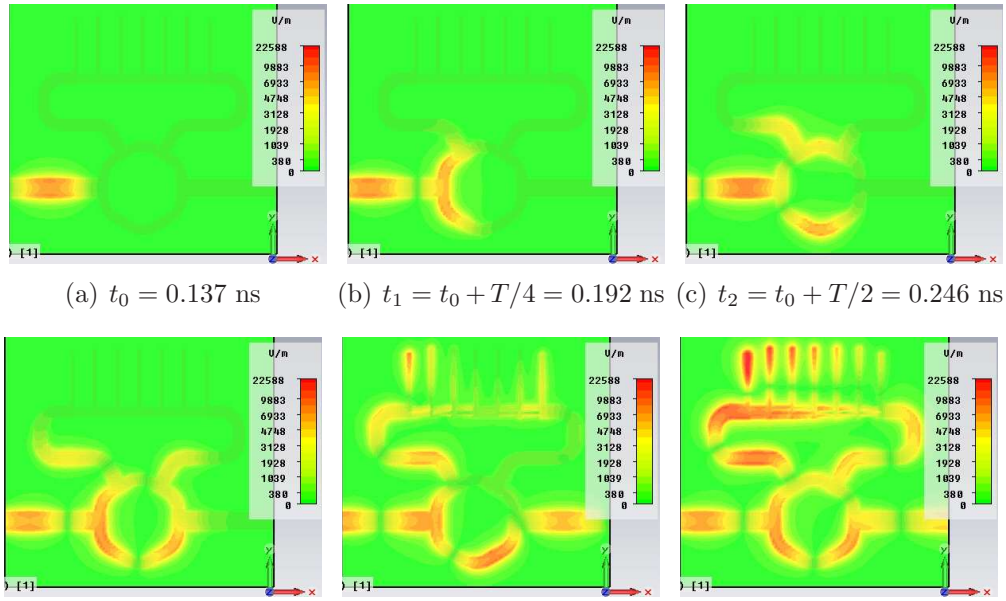

(a) $t_0 = 0.137$ ns (b) $t_1 = t_0 + T/4 = 0.192$ ns (c) $t_2 = t_0 + T/2 = 0.246$ ns

(d) $t_3 = t_0 + 3T/4 = 0.30$ ns (e) $t_4 = t_0 + T = 0.519$ ns (f) $t_5 = t_0 + 8T = 1.884$ ns

Figure 5.12 Full-wave simulated (FIT, CST Microwave Studio) transient electric field distributions for the power-recycling 3-dB LWA system of Fig. 5.8 with parameters of Fig. 5.10 at different instants. The excitation frequency is $f = 4.58$ GHz, corresponding to the harmonic period of $T = 1/f = 0.218$ ns.

5.2.4 Experimental Demonstration

This section presents the experimental performance of the proposed power-recycling LWA system, again for the 3-dB case, by comparing the open-loop and feedback system responses. Real ohmic and dielectric losses are naturally present in this case, and therefore the results of this section provide a realistic assessment of the efficiency enhancement capability of the system.

Open-loop (isolated) LWA

Fig. 5.13(a) shows the scattering parameters for the isolated (open-loop) CRLH LWA shown in the inset of Fig. 5.13(b). This antenna was designed to dissipate a combined radiation and loss power, computed by $1 - S_{11}^2 - S_{21}^2$ and shown in Fig. 5.13(b), close to 3 dB for a 3-dB power-recycling system. The gain, directivity, and efficiency performances of this antenna are listed in the left-hand side of Tab. 5.5. The radiation efficiency is of only $\eta_0 = 38\%$, a poor performance largely imputable to the ohmic/dielectric loss and the 50% power loss in the load.

Table 5.5 Gain, directivity, and efficiency for the open loop LWA of Fig. 5.13 and for the power-recycling LWA system of Fig. 5.14.

	Open-loop LWA ($\eta = \eta_0$)		Feedback LWA ($\eta = \eta_s$)	
	Full-wave	Measured	Full-wave	Measured
G	3.68 dB	3.70 dB	6.73 dB	5.77 dB
D	7.84 dB	7.88 dB	7.85 dB	7.42 dB
η	38.36%	38.00%	77.27%	68.45%

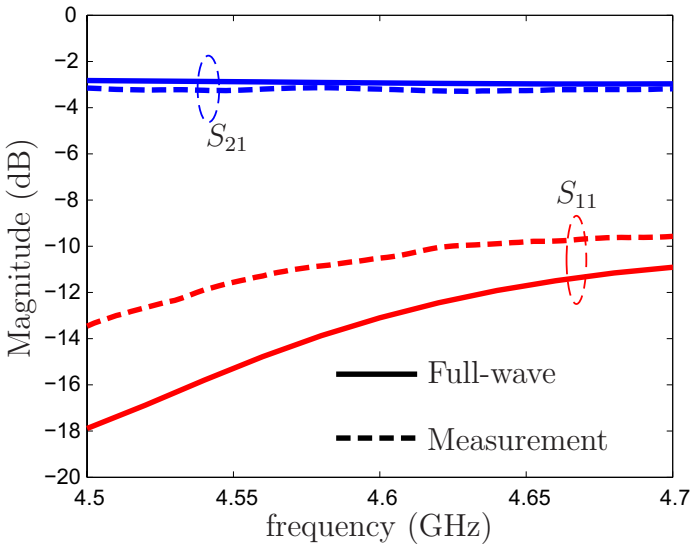

(a)

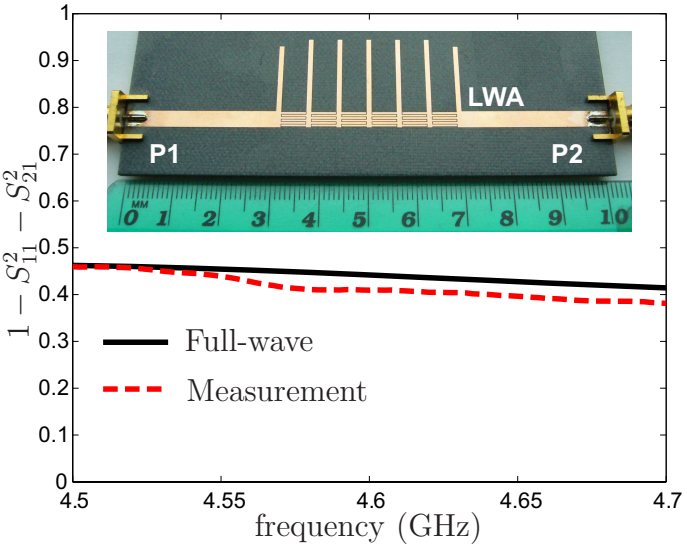

(b)

Figure 5.13 Full-wave simulated (MoM, Ansoft Designer) and measured scattering parameters for the 3-dB CRLH LWA prototype shown in the inset, which has the parameters given in Fig. 5.10, except for the number of unit cells which is here $N = 7$. (a) Return and insertion losses. (b) Dissipated power ratio, including radiation and loss power.

Power-recycling LWA System

The antenna of Fig. 5.13 is now inserted into a 3-dB power-recycling system, as shown in Fig. 5.14. The corresponding scattering parameters and dissipated power

are shown in Fig. 5.15. In the full-wave simulation, essentially all of the power has been dissipated ($S_{21} = S_{11} = 0$), while around 94% of the power has been dissipated in the experimental case.

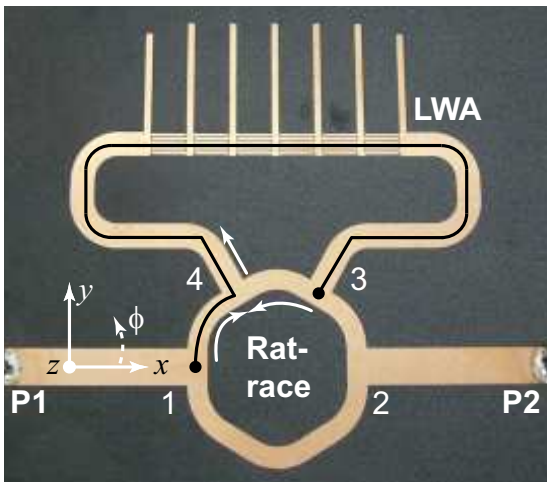

Figure 5.14 Power-recycling 3-dB LWA prototype using the same antenna as in Fig. 5.15 with relevant phase shifts and power flow indications. The total phase shift from port 1 to port 3 along the solid line is: $\ell_{14} + \ell_{45} + \ell_{LWA} + \ell_{63} = \pi/2 + 7\pi/4 + 0 + 7\pi/4 = 4\pi$ ($\ell_{LWA} = 0$ since the CRLH LWA is operated here at broadside).

The gain, directivity, and efficiency performances are given in the right-hand side of Tab. 5.5. The full-wave and experimental radiation efficiencies are of 77% and 68%, respectively. This represents enhancements by factors of 2.01 and 1.80, respectively, fairly well corresponding to the system gain of $G_s = 2$ expected from (5.11) and Fig. 5.9 for a 3-dB system. The deviation from a 100% system efficiency is explained by a threefold reason: i) ohmic and dielectric losses (not considered in previous sections), ii) imperfect design of the rat-race (in measurement, $S_{21} \approx -18$ dB in Fig. 5.15(b), while it should ideally be $-\infty$, meaning that a small amount of power is still dissipated in the load in the steady-state regime), iii) the LWA is not perfectly matched to the 50 Ω impedance of the rat-race (in measurement, $S_{11} \approx -11$ dB in Fig. 5.13(a), while it should ideally be $-\infty$).

Finally, the radiation patterns of the structure are plotted in Fig. 5.16. The asymmetry in the E-plane [Fig. 5.16(a)] may first appear surprising, since the system's topology is perfectly symmetric with respect to the zy-plane. The reason for

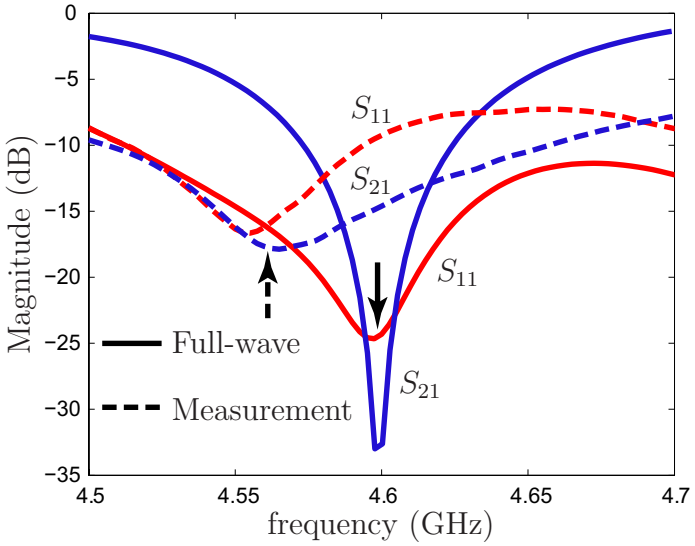

(a)

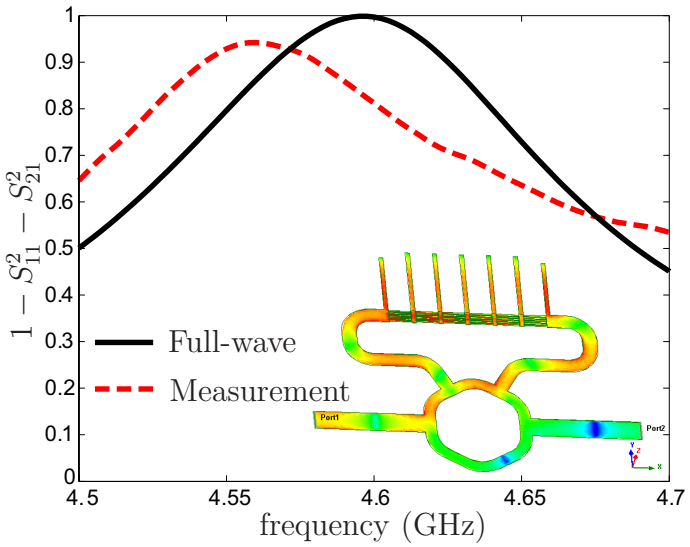

(b)

Figure 5.15 Full-wave simulated (MoM, Ansoft Designer) and measured scattering parameters for the power-recycling 3-dB LWA system shown in Fig. 5.14. (a) Return and insertion losses. (b) Dissipated power ratio, including radiation and loss power. The inset shows the steady-state regime simulated electric field distribution.

this asymmetry is that the structure *electromagnetically asymmetric*, since the Δ port is cold, as clearly visible in the inset of Fig. 5.15(b).

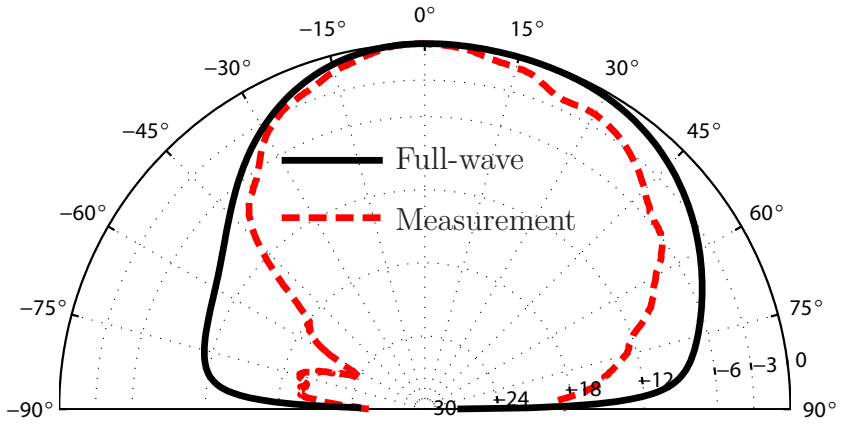

(a) $\phi = 0^o$ plane

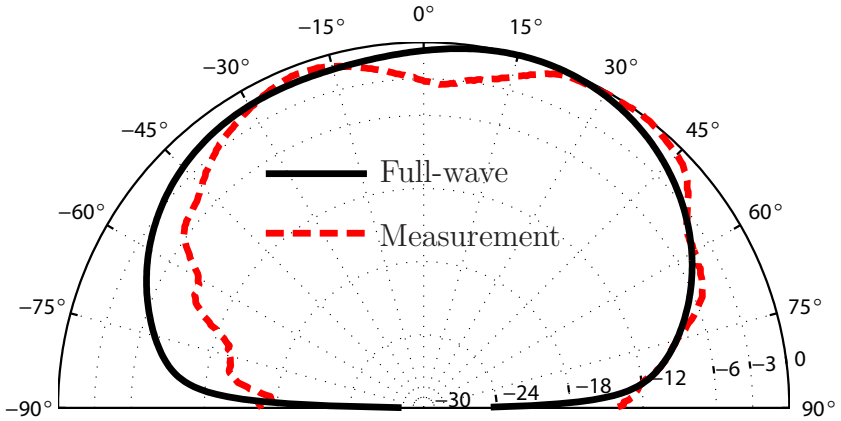

(b) $\phi = 90^o$ plane

Figure 5.16 Full-wave simulated (MoM, Ansoft Designer) and measured radiation patterns for the power-recycling LWA of Fig. 5.14. a) $\phi = 0^o$ plane (E-plane). b) $\phi = 90^o$ plane (H-plane).

5.2.5 Conclusions

Conventional LWAs provide high directivity while featuring a simple architecture, but suffer from low radiation efficiency, often prohibitive in practical applications with size restriction, since all the power that has not been radiated when reaching their end is dumped into the load. This work has proposed a general solution to this fundamental problem: a novel power-recycling feedback system, which feeds back the non-radiated power to the input of the LWA through a power combining system. This power combining system is a rat-rate coupler, which constructively adds the input

and feedback powers while ensuring perfect matching and isolation of the two signals, thereby dramatically enhancing the antenna's efficiency. Specifically, the radiation efficiency of the isolated (or open-loop) LWA, η_0, is enhanced by the system's gain factor G_s ($G_s > 1$) to the overall radiation efficiency of $\eta_s = G_s\eta_0$, which may reach 100% for any value of η_0 in a lossless system.

The design conditions of the power-recycling system, depending on η_0, has been derived for a rat-race based implementation, under the form of rat-race impedance ratios and feedback phase conditions. The build-up of the steady-state regime from the transient regime at the onset of the system has been explicated by transient circuit and electromagnetic simulations, and an experimental power-recycling LWA system has been demonstrated, where the isolated antenna efficiency η_0 is enhanced from 38% to 68%, corresponding to a system efficiency enhancement of $G_s = 1.8$. The proposed power-recycling feedback scheme applies to all LWAs and solves their fundamental efficiency problem in practical applications involving a trade-off between relatively high directivity (higher than half-wavelength resonant antennas) and small size (smaller than open-loop LWAs or complex phased arrays).

In this work, the power-recycling feedback system was designed for fixed CRLH LWA broadside radiation. This design is currently being extended for frequency [80] and electronic [81], [82] full-space scanning capabilities, by incorporating phase shifting elements in both the feedback loop and the power combiner. This will lead to a LWA structure with both maximal efficiency and full-space scanning capabilities.

Chapter 6

Assessment of the Thesis's Contributions

The thesis focuses primarily on the development of novel planar practical microwave components, antennas and systems using the CRLH TL concept [4]. This work has generated 15 peer-reviewed journal papers (8 as a first author), 22 conference articles (9 as a first author), 2 patents, and 1 trade show presentation (refer to Appendix D for a complete list). The seven journal papers presented in this dissertation are a subset of the Ph.D. work's publications and represent approximately 60% of the overall work. The selected topics present the most recent advances of CRLH TL MTMs in three distinct classes of applications: harmonic regime guided-wave, impulse regime guided-wave and radiated-wave applications. The following sections assess the contributions in each of the three categories.

6.1 Harmonic Regime Guided-wave Components

MIM capacitors have removed the spurious transverse resonances of interdigital capacitors and have been employed in all 3 CRLH TL harmonic regime components: the BPF, the infinite-wavelength series power divider and the coupled-line couplers. These components possess clear advantages and also some drawbacks. They are assessed in the following.

Contribution 1: Implementation of CRLH TLs using MIM capacitors

- **Advantages**
  1. Wide bandwidth: Because transverse resonances are completely eliminated in MIM capacitors, the MIM capacitor CRLH TL implementation has a wide frequency bandwidth between the lower LH cutoff ω_{CL} and the upper RH cutoff ω_{CR}.

2. Small size: The high capacitance per unit area of MIM capacitors results in a compact LH capacitor and hence a small size for CRLH TL structures.
3. Symmetric structure: The MIM capacitor CRLH TL structure is physically and therefore also electrically symmetric ($Z/2$ - Y - $Z/2$). A symmetry is a desirable property which leads to equal Bloch impedances seen at both ends of the CRLH TL structure.

– **Drawback and possible solution**

1. Multi-layer circuit: An additional metallic layer is required to fabricate MIM capacitor CRLH TL structures and therefore necessitates multi-metallic-layer dielectric substrates. Fortunately, multi-layer PCB fabrication process is routinely available and provides a remedy to the multi-layer circuit drawback of MIM capacitor CRLH TL structures.

Contribution 2: Wide-band BPF using MIM capacitor CRLH TL structure

– **Advantages**

1. Ultrawide bandwidth: The BPF has an optimum FBW of 141% (arithmetic) or 200% (geometric) and is well suitable for ultrawide band applications.
2. Sharp rejection: The sharp rejection at low frequency is due to the slow-wave effect of CRLH TL, while the sharp rejection at high frequency is due to the presence of tapered coupled resonators.

– **Limitation**

1. Non-optimum design: The BPF uses CRLH TL periodic structure and its design is based on the phase response (dispersion) rather than the amplitude response. In addition, the CRLH TL has its Bloch impedance seen at the ports varied with frequency. As a result, the BPF is a non-optimum filter design in terms of pass-band ripple and return loss.

Contribution 3: Infinite-wavelength tunable series feeding network

– **Advantages**

1. Arbitrary port spacing: Because the CRLH TL operates in its infinite-wavelength regime, all the UCs have the same phase and magnitude. As a result, output ports can be placed arbitrary at the locations of UC along the series feeding network.

2. Arbitrary number of ports: The input L-matching network can be dynamically tuned with the shunt varactor diode to match different input impedance values resulting from adding or removing the output ports. Therefore, the series feeding network can support an arbitrary number of output ports.

– **Limitation**

1. Beam squinting: At frequencies other than the infinite-wavelength frequency, the output ports have phase imbalances due to phase shift across the UCs. For antenna array applications, a consequence of the phase imbalances is that the main beam squints when a finite bandwidth signal is applied to the series feeding network. However, this limitation is also true in all series feeds.

– **Comparison**

1. In contrast to the conventional series traveling-wave feeds where the port spacing required for a broadside radiation is either one half-wavelength or one wavelength [83], the infinite-wavelength CRLH TL series feed has the port spacing *independent* of wavelength.

Contribution 4: Generalized CMT analysis

– **Advantages**

1. Coupling explanations: The CMT analysis explains the complex coupling phenomena of both symmetric and asymmetric CRLH TL couplers. The CMT analysis also shows that, for both types of CRLH TL couplers, the coupling is proportional to the coupler's length. Therefore, a high coupling level, theoretically up to 0 dB, can be achieved.
2. Universal application: Since the CMT analysis utilizes the generalized CRLH TL circuit model, it is capable of handling symmetric (RH and LH) and asymmetric (RH and LH) couplers.

– **Limitation and possible solution**

1. Port matching assumption: In both TEM and quasi-TEM approximation of the CMT analysis, it is assumed that all ports are matched. While this reasonable assumption provides simplified expressions for the coupling and the through, it does not properly model the return loss and isolation. The

possible solution to this limitation is to model the mismatch and multiple reflection at all ports in the CMT analysis. It might lead to complicated expressions which provides little insight into the complex coupling nature of the CRLH TL coupled-line couplers.

– **Comparison**

1. In direction comparison with previous analyses for the symmetric coupler [14] and the asymmetric coupler [13], the CMT analysis using generalized CRLH TL circuit model is an unified approach that explains the complex coupling phenomenon, the high coupling level, and the coupling range of the symmetric and asymmetric coupled-line couplers.

6.2 Impulse Regime Guided-wave Components and Systems

While conventional coupled-line couplers, which can be seen as a particular case of CRLH TL coupled-line couplers with LH elements approaching infinite, i.e. $L_L = C_L = \infty$, have been extensively employed in many harmonic-regime narrow-band systems, they are rarely used in impulse-regime applications. The coupler-based time differentiator represents an unique impulse-regime component that is well suitable for analog pulse generation circuits found in pulse radar and pulse communication systems. On the other hand, the PPM transmitter is the first impulse-regime system that demonstrates the pulse modulation capability of CRLH dispersive delay line. Advantages and limitations of these components and systems follow.

Contribution 5: Time differentiation using coupled-line couplers

– **Advantages**

1. Multiple-order differentiations: Both first- and second-order differentiations can be obtained simultaneously with a passive coupled-line coupler.
2. No DC power and low noise: A coupled-line coupler is a passive device which does not consume any DC power and does not generate any noise as oppose to an implementation using operational amplifier and discrete capacitor.

– **Limitation and possible solution**

1. Limited pulse width: Only signal with a certain pulse width ΔT that satisfies the condition $\Delta T \gg 1/(4f_0)$ can be correctly differentiated by a pre-designed coupler operating at the coupling center frequency f_0. For signals with a narrower pulse width, new couplers operating at higher frequencies are required. Since directional coupled-line couplers are simple, a set of couplers with various coupling center frequencies can be pre-fabricated in order to accommodate signals having different pulse widths.

Contribution 6: PPM transmitter

- **Advantages**
  1. Arbitrary M-ary modulation: Continuous and tunable time delay properties of CRLH dispersive delay line allow multiple M-ary modulation schemes.
  2. No DC power and noise: Because CRLH dispersive delay line is a passive circuit comprised of inductor and capacitor passive elements, it does not consume any DC power and do not generate any noise as oppose to digital delay line implemented in CMOS technology or analog delay line using diode switches.
- **Limitations and possible solutions**
  1. Pulse widening: Because the CRLH dispersive delay line has a group velocity varying as a function of frequency, each frequency component of the modulated pulses propagates at a different velocity (dispersion). As a result, the envelope of the modulated pulses spreads after propagating through the CRLH dispersive delay line. A consequence of this pulse widening is interference between successive pulses. The pulse interference places a limit on the maximum pulse data rate that can be supported by the PPM transmitter.
  2. Large size: The CRLH dispersive delay line features an inherent large size, mainly due to the limitation of current PCB fabrication. This technological limitation can be overcome by a multi-layer PCB or a microwave integrated circuit fabrication process.

6.3 Radiated-wave Components and Systems

The two novel power-recycling concepts have greatly enhanced the low radiation efficiency of any 2-port LWAs. Both concepts recycle non-radiated power at the output termination of a LWA back to its input via either a series feeding network in the case of the cross power-recycling 2D LWA array or a rat-race coupler in the case of the self power-recycling feedback LWA system. To the best of the author's knowledge, these power-recycling concepts for enhancing LWA's radiation efficiency have not been reported previously in the literature. Advantages, limitations and possible solutions of these two concepts are listed in the following.

Contribution 7: Cross power-recycling method

- **Advantages**
  1. High radiation efficiency: A high radiation efficiency η is achieved by increasing the number of array elements N while keeping the length of each array element ℓ constant.
  2. High gain: As N increases, the directivity D increases because the physical aperture of the LWA array is larger. As a result, the LWA array's gain, computed as $G = \eta D$, increases rapidly.
  3. Universal application: The method is based on an external circuit approach and therefore can be applied to enhance radiation efficiency of any array consisting of 2-port LWAs.
- **Limitation and possible solution**
  1. Array application: Since the power is cross-recycled between LWA elements, this method is only applicable to enhance radiation efficiency of a LWA array with $N > 1$. The solution for a single LWA is a self power-recycling feedback system.
- **Comparison**
  1. In direct comparison with a series fed array of resonant patches arranging in a 2D configuration, the cross power-recycling array is superior because its radiation efficiency is proportional to the array's size (the number of array's elements or the length of each element). In contrast, the radiation efficiency of the series fed array is not proportional to its size and therefore cannot be enhanced.

Contribution 8: Self power-recycling feedback system

- **Advantages**
  1. Efficient power utilization: The non-radiated RF power is completely recycled and fed back to the input as oppose to being wasted as heat in the termination load.
  2. Maximum system's radiation efficiency: As power available to the LWA is enhanced by the feedback power, the LWA radiates more power for the same amount of input power applied to the LWA feedback system. As a result, the LWA's radiation efficiency is maximized (theoretically) to 100%.
  3. Universal application: The method is based on an external circuit approach and therefore can be applied to enhance radiation efficiency of any 2-port LWA.
- **Limitations and possible solutions**
  1. Frequency scanning: While the LWA itself has the frequency-scanning capability, the power-recycling feedback LWA system loses the frequency-scanning advantage due to the phase condition around the feedback loop. However, this limitation can be overcome by introducing a phase shifter inside the loop. The phase shifter allows the power-recycling feedback LWA system to operate at other frequencies and therefore permits frequency scanning.
  2. Bandwidth limitation: The bandwidth of the power-recycling feedback LWA system is limited by the three-quarter wavelength TL of the rat-race coupler. Simple bandwidth enhancement techniques such as phase reversal [84], [85] provide a practical solution to this bandwidth limitation.
- **Comparisons**
  1. In comparison with resonant-type antennas such as microstrip patches or dipoles, the self power-recycling feedback LWA system provides an extra flexibility in designing LWAs with a comparable size but a superior radiation efficiency and directivity.
  2. In order to reach a maximum radiation efficiency of 100%, a conventional LWA with a finite leakage factor requires an *infinite length* so that all input power leaks out completely. It should be noted that the signal travels only

one time through the LWA. In contrast, the feedback loop of the self power-recycling feedback LWA system re-directs the signal and makes it travels an *infinite time* around a *finite length* LWA until all input power leaks out completely.

Chapter 7

Conclusions and Future Works

7.1 Conclusions

This thesis consists of a collection of published articles related to recent advances of microwave MTMs in three specific application areas: harmonic regime guided-wave, impulse regime guided-wave, and radiated-wave. The CRLH TLs have been exclusively employed in all guiding and radiating applications and offer the benefits of planar implementation, non-resonant structure, and wide bandwidth. The selected articles represent novel CRLH TL components, antennas, and systems belong to the three aforementioned applications.

Harmonic regime has been one of the main guided-wave applications of CRLH TL MTMs. This regime is of particular interest because CRLH TL-based components have superior characteristics such as dual/triple/quad-band, enhanced bandwidth, and enhanced coupling compared to conventional components. In this work, CRLH TLs implemented in the new MIM capacitor configuration which results in a compact, symmetric and transverse resonant-free design are further extended to cover filter, power divider/combiner and coupler applications. A wideband BPF is realized using tapered coupled-resonator MIM capacitor CRLH TL structure, verified experimentally, and compared with conventional BPF having the same order. A tunable infinite-wavelength N-port series power divider implemented in a shielded MIM capacitor CRLH TL configuration is demonstrated to support an arbitrary number of output ports as well as ports' location. This arbitrary N-port series power divider finds applications in phased-array antenna and space power combining. CRLH TL coupled-line couplers are studied analytical using the generalized CMT approach and verified experimentally. Furthermore, the coupled-mode theory allows the exact complex coupling mechanism of both symmetric and asymmetric CRLH TL coupled-line couplers.

In contrast to harmonic regime, impulse regime application of CRLH TL is a

new research topic that has recently been introduced. Earlier work conducted by researchers in our group [24] has laid the foundation for dispersion engineering research and impulse regime guided-wave components. In this work, two impulse regime components are proposed for pulse generating and transmitting applications. The first- and second-order differentiators exploits the time derivative characteristic of conventional coupled-line couplers to generate time-domain pulse signals. Built upon the dispersion characteristic of CRLH TLs and its ability to provide a tunable time delay of modulated pulses, the first CRLH TL dispersive delay line PPM transmitter is proposed and verified analytically and experimentally. A proof-of-concept of such transmitter is built and evaluated in an indoor environment and demonstrates the multiple order PPM capability.

Radiated-wave components such as LWAs represent another important application of CRLH TL MTMs. The traveling-wave nature of LWAs is advantageous because it permits highly directive antennas but also disadvantageous in terms of radiation efficiency, requiring that most of the power has leaked out before reaching the termination. In this work, two novel power-recycling concepts are introduced to remedy this efficiency drawback. The first cross-recycling concept recycles the power between LWA elements via a series feeding network and enhances both the radiation efficiency and directivity of 2D LWA arrays. The second self-recycling concept recycles the non-radiated power back to the LWA's input via a rat-race coupler which serves as a positive feedback network. Both concepts are studied analytically, verified numerically using electromagnetic simulation softwares, and demonstrated experimentally.

7.2 Future Works

This section presents some possible direct extensions of this work in three application categories.

7.2.1 Harmonic Regime Guided-wave Applications

In this work, the CRLH TL structures are periodic, patterned and discontinuous TLs which are constructed by patterning printed series MIM capacitors and shunt shorted-stub inductors on an isotropic dielectric substrate to form the appropriate LC equivalent circuit. The series capacitors C_L and shunt inductors L_L can be designed to synthesize the effective permeability μ_{eff} and permittivity ε_{eff} parameters of the CRLH TL structures. Intuitively, one would expect to synthesize similar effective parameters by printing an uniform and continuous TL on a substrate loaded with capacitor and inductor elements. This is the basic idea of a 'meta-substrate' concept, which is illustrated in Fig. 7.1 [86]. The meta-substrate is an anisotropic artificial dielectric substrate made of sub-wavelength series capacitors (triangular shape, MIM configuration shown in Fig. 7.1) and shunt inductors (thin, vertical metallic poles). It was shown that a z-directed microstrip TL printed on this anisotropic substrate is capable of supporting a quasi-TEM wave along the z direction. A leaky-wave application of such microstrip TL on meta-substrate has been demonstrated experimentally in [86]. However, detail theoretical analysis had not been done for this meta-substrate as well as the microstrip TL on the meta-substrate which is seen as a uniform-trace meta-substrate CRLH TL structure. It is expected that the meta-substrate CRLH TL structure can be used in many harmonic regime guided-wave applications such as filters, power dividers/combiners, and couplers. This work is currently being investigated by a Ph.D. student in the author's group, Ms. A. Shahvarpour, in her work related to the electromagnetic analysis of an uniaxial and anisotropic meta-substrates.

7.2.2 Impulse Regime Guided-wave Applications

The coupler-based time differentiator is an unique device for pulse shaping and pulse generating applications. However, both first and second-order pulse differentiators require an input periodic pulse signal for their operations. In the case of the second-order pulse differentiator, a train of decaying pulses is observed at the output

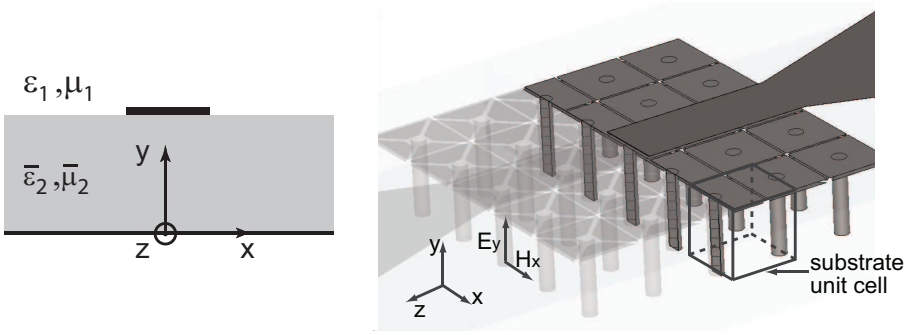

Figure 7.1 Proposed meta-substrate CRLH TL structure comprised of MIM capacitors and thin vertical poles as inductors.

port as shown in Fig. 7.2(a) for an input step pulse. The pulse train is formed because only part of the energy of the first-order derivative pulse in the upper loop is coupled out as the output's second-order derivative pulse due to a finite coupling of the coupled-line coupler. The remaining energy is circulated inside the upper loop and coupled out again after a delay of τ until no energy remains in the pulse. The delay τ is the pulse train's period which is equal to the sum of the propagation delay of the coupler and the delay of the time delay circuit, while the decaying amplitudes is proportional to the losses of the coupler (coupling, metallic and dielectric losses).

Based on this observation, it is then expected that by introducing an amplifier in the upper loop so as to compensate for the losses, the decaying pulse train will turn into a self-sustained, constant amplitude pulse train. The self-sustained pulse generator concept is illustrated in Fig. 7.2(b). A low pass filter is added to suppress high-frequency resonances of the loop. The self-sustained pulse generator is currently being investigated.

7.2.3 Radiated-wave Applications

As mentioned earlier, the self power-recycling feedback LWA system loses the frequency-scanning capability of LWAs due to the phase condition around the loop and has a narrow bandwidth due to the presence of the three-quarter wavelength TL in the rat-race coupler. The possible solution to the frequency-scanning limitation is to replace the two transmission lines ℓ_{45} and ℓ_{63} with a phase shifter whose phase shift satisfies the phase condition set out in (5.9b). The phase shifter will allow the power-recycling feedback LWA system operating at frequencies other than the transition fre-

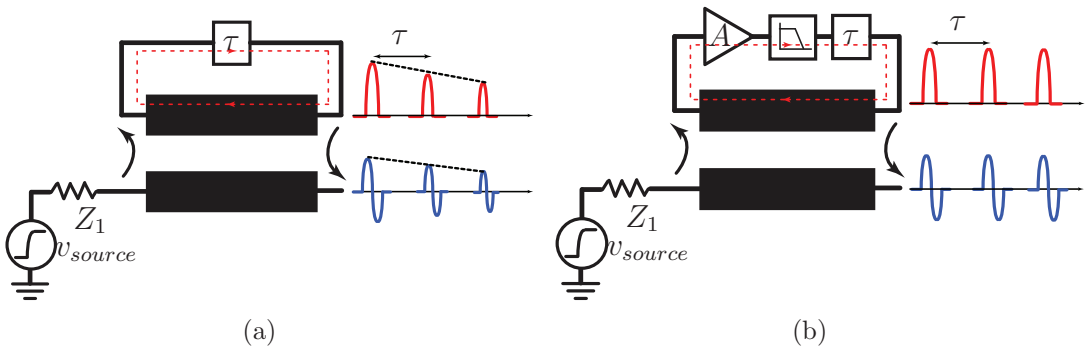

(a) (b)

Figure 7.2 Coupler-based pulse generator. (a) Decayed pulse generator. (b) Self-sustained pulse generator with an amplifier and a lowpass filter.

quency as demonstrated in this work and hence permit beam scanning. The solution to the bandwidth limitation of the rat-race is to replace the three-quarter wavelength TL with a TL having the same characteristic impedance, but whose electrical length is realized by a quarter wavelength TL plus an ideal phase reversing network [84]. It is thus expected that, by applying these solutions, the current power-recycling feedback LWA system will have a frequency-scanning capability over a wide bandwidth in addition to high radiation efficiency.

While frequency-scanning capability is an important advantage of LWAs for scanning applications, it is a disadvantage for applications such as point-to-point communication systems as it limits the maximum pattern bandwidth of the antenna. In both power-recycling concepts introduced in this work, the LWAs scans with frequency in the longitudinal plane. In order to operate the LWAs at a *fixed* frequency while providing beam-scanning capability, varactors diode can be introduced in the UCs of LWAs as suggested by Lim *et. al* [82]. However, previous work on electronically scanned LWAs has a drawback of poor input impedance matching versus scanned angle. Recent collaboration work of Mr. R. Sigarusa, a Ph.D. student at the Laboratoire de Conception de d'Integration des Systèmes, Valence, France and the author has investigated an alternative implementation with two tuning voltages for varactor diodes to simultaneously allow beam scanning and impedance matching [87]. It is thus expected that electronically scanned LWAs can be utilized in the power-recycling concepts for applications requiring beam-scanning capability at a fixed frequency in addition to high radiation efficiency.

References

[1] V. G. Veselago, "The electrodynamics of substances with simultaneously negative value of ϵ and μ," *Soviet Physics Uspekhi*, vol. 10, no. 4, pp. 509 – 514, 1968.

[2] D. R. Smith, W. J. Padilla, D. C. Vier, S. C. Nemat-Nasser, and S. Schultz, "Composite medium with simultaneously negative permeability and permittivity," *Physics Review Letters*, vol. 84, no. 8, pp. 4148 – 4187, May 2000.

[3] Y. Hao and R. Mittra, *FDTD Modelling of Metamaterials: Theory and Applications*. Norwood, MA: Artech House, 2009.

[4] C. Caloz and T. Itoh, *Electromagnetic Metamaterials : Transmission line Theory and Microwave Applications*. New Jersey: Wiley-Interscience. IEEE Press., 2005.

[5] G. V. Eleftheriades and K. G. Balmain, Eds., *Negative-Refraction Metamaterials: Fundamental Principles and Applications*. New Jersey: Wiley-Interscience. IEEE Press., 2005.

[6] N. Engheta and R. W. Ziolkowski, Eds., *Electromagnetic Metamaterials: Physics and Engineering Explorations*. New Jersey: Wiley-Interscience. IEEE Press., 2006.

[7] W. Cai and V. Shalaev, *Optical Metamaterials: Fundamentals and Applications*. Springer, 2009.

[8] V.-H. Nguyen and C. Caloz, "Simple-design and compact MIM CRLH microstrip 3-db coupled-line coupler," in *Proc. IEEE MTT-S International Microwave Symposium Digest (IMS)*, San Francisco, CA, USA, June 2006, pp. 1733–1736.

[9] C. Caloz and T. Itoh, "Application of the transmission line theory of left-handed (lh) materials to the realization of a microstrip lh transmission line," in *Proc. IEEE AP-S International Symposium and USNC/URSI National Radio Science Meeting*, vol. 1, San Antonio, TX, USA, June 2002, pp. 412– 415.

[10] A. K. Iyer and G. V. Eleftheriades, "Negative refractive index metamaterials supporting 2-d waves," in *Proc. IEEE MTT-S International Microwave Symposium Digest, (IMS)*, vol. 2, Seattle, WA, USA, June 2002, pp. 412 – 415.

[11] A. A. Oliner, "A periodic-structure negative-refractive-index medium without resonant elements," in *Proc. IEEE AP-S International Symposium and USNC/URSI National Radio Science Meeting, URSI Digest*, San Antonio, TX, USA, June 2002, p. 41.

[12] F. P. Casares-Miranda, P. Otero, E. Marquez-Segura, and C. Camacho-Penalosa, "Wire bonded interdigital capacitor," *IEEE Microwave and Wireless Components Letters*, vol. 15, no. 10, pp. 700 – 702, October 2005.

[13] C. Caloz and T. Itoh, "A novel mixed conventional microstrip and composite right/left-handed backward-wave directional coupler with broadband and tight coupling characteristics," *IEEE Microwave and Wireless Components Letters*, vol. 14, no. 1, pp. 31 – 33, January 2004.

[14] C. Caloz, A. Sanada, and T. Itoh, "A novel composite right-/left-handed coupled-line directional coupler with arbitrary coupling level and broad bandwidth," *IEEE Transactions on Microwave Theory and Techniques*, vol. 52, no. 3, pp. 980 – 992, March 2004.

[15] M. I. Skolnik, *Introduction to Radar Systems*, 3rd ed. New York: McGraw-Hill, 2002.

[16] B. P. Lathi, *Modern digital and analog communication systems*, 3rd ed. New York: Oxford-University Press., 1998.

[17] K. Siwiak and D. McKeown, *Ultra-wideband Radio Technology.* New Jersey: Wiley, 2004.

[18] M. Miao and C. Nguyen, "On the development of an integrated cmos-based uwb tunable-pulse transmit module," *IEEE Transactions on Microwave Theory and Techniques*, vol. 54, no. 10, pp. 3681–3687, Oct. 2006.

[19] T. Buchegger, G. Ossberger, A. Reisenzahn, A. Stelzer, and A. Springer, "Pulse delay techniques for ppm impulse radio transmitters," in *Proc. IEEE International Conference on Ultra Wideband Systems and Technologies, (ICUWB)*, Reston, Virginia, USA, November 2003, pp. 37 – 41.

[20] J. R. Andrews. (2000, May) Picosecond pulse generators for uwb radars. Picosecond Pulse Labs, Application note AN-9. [Online]. Available: http://www.picosecond.com/objects/AN-09.pdf

[21] J. Wang, W. Wang, D. Wang, and G. Lu, "A modulation circuit for impulse radio ultra-wideband communications," in *Proc. IEEE Asia-Pacific Microwave Conference (APMC)*, vol. 5, December 2005.

[22] M. Laso, T. Lopetegi, M. Erro, D. Benito, M. Garde, M. Muriel, M. Sorolla, and M. Guglielmi, "Real-time spectrum analysis in microstrip technology," *Microwave Theory and Techniques, IEEE Transactions on*, vol. 51, no. 3, pp. 705–717, Mar 2003.

[23] S. Abielmona, S. Gupta, V.-H. Nguyen, and C. Caloz, "Dispersion-engineered metamaterial devices for impulse-regime," in *Proc. XXIXth Assembly of Union of Radio Science International (URSI)*, Chicago, IL, USA, August 2008.

[24] S. Abielmona, S. Gupta, and C. Caloz, "Experimental demonstration and characterization of a tunable crlh delay line system for impulse/continuous wave," *IEEE Microwave and Wireless Components Letters*, vol. 17, no. 12, pp. 864 – 866, December 2007.

[25] V.-H. Nguyen, S. Abielmona, and C. Caloz, "Analog dispersive time delayer for beam-scanning phased array without beam-squinting," in *Proc. IEEE AP-S International Symposium*, San Diego, CA, USA, July 2008, pp. 1 – 4.

[26] S. Abielmona, S. Gupta, and C. Caloz, "Compressive receiver using a crlh-based dispersive delay line for analog signal processing," *IEEE Transactions on Microwave Theory and Techniques*, to be published.

[27] S. Gupta, S. Abielmona, and C. Caloz, "Microwave analog real-time spectrum analyzer (rtsa) based on the spatial-spectral decomposition property of leaky-wave structures," *IEEE Transactions on Microwave Theory and Techniques*, to be published.

[28] V. Dolat and R. Williamson, "A continuously variable delay-line system," in *1976 Ultrasonics Symposium*, 1976, pp. 419–423.

[29] W. Ishak, "Magnetostatic wave technology: a review," *Proceedings of the IEEE*, vol. 76, no. 2, pp. 171–187, Feb 1988.

[30] R. Withers, A. Anderson, J. Green, and S. Reible, "Superconductive delay-line technology and applications," *Magnetics, IEEE Transactions on*, vol. 21, no. 2, pp. 186–192, Mar 1985.

[31] T. Kodera and C. Caloz, "Uniform ferrite-loaded open waveguide structure with crlh response and its application to a novel backfire-to-endfire leaky-wave an-

tenna," *IEEE Transactions on Microwave Theory and Techniques*, vol. 57, no. 4, pp. 784–795, April 2009.

[32] S. Paulotto, P. Baccarelli, F. Frezza, and D. Jackson, "A novel technique for open-stopband suppression in 1-d periodic printed leaky-wave antennas," *IEEE Transactions on Antennas and Propagation*, vol. 57, no. 7, pp. 1894–1906, July 2009.

[33] J. D. Jackson, *Classical Electrodynamics*, 3rd ed. New York: J. Wiley, 1999.

[34] J. Gomez-Tornero, D. Caete-Rebenaque, and A. Alvarez-Melcon, "Microstrip leaky-wave antenna with control of leakage rate and only one main beam in the azimuthal plane," *IEEE Transactions on Antennas and Propagation*, vol. 56, no. 2, pp. 335–344, Feb. 2008.

[35] V.-H. Nguyen and C. Caloz, "Broadband highly selective bandpass filter based on a tapered coupled-resonator (tcr) crlh structure," *Proceedings of the European Microwave Association*, vol. 2, no. 5, pp. 44 – 51, March 2006.

[36] ——, "Tunable arbitrary n-port crlh infinitewavelength series power divider," *Electronics Letters*, vol. 43, no. 23, January 2007.

[37] ——, "Generalized coupled-mode approach of metamaterial coupled-line couplers: Coupling theory, phenomenological explanation, and experimental demonstration," *IEEE Transactions on Microwave Theory and Techniques*, vol. 55, no. 5, pp. 1029 – 1039, May 2007.

[38] ——, "First- and second-order differentiators based on coupled-line directional couplers," *IEEE Microwave and Wireless Components Letters*, vol. 18, no. 12, pp. 791 – 793, December 2008.

[39] ——, "Crlh delay line pulse position modulation transmitter," *IEEE Microwave and Wireless Components Letters*, vol. 18, no. 8, pp. 527 – 529, August 2008.

[40] V.-H. Nguyen, S. Abielmona, and C. Caloz, "Highly efficient leaky-wave antenna array using a power-recycling series feeding network," *IEEE Antennas and Wireless Propagation Letters*, vol. 8, pp. 441 – 444, June 2009.

[41] V.-H. Nguyen, A. Parsa, and C. Caloz, "Power-recycling feedback system for maximization of leaky-wave antennas radiation efficiency," *IEEE Transactions on Microwave Theory and Techniques*, submitted for publication.

[42] D. M. Pozar, *Microwave Engineering*, 2nd ed. New York: John Wiley, 2005.

[43] C. Nguyen, "Development of new miniaturised bandpass filter having ultrawide bandwidth," *Electronics Letters*, vol. 30, no. 10, pp. 767 – 768, May 1994.

[44] L.-H. Hsieh and K. Chang, "Compact, low insertion-loss, sharp-rejection, and wide-band microstrip bandpass filters," *IEEE Transactions on Microwave Theory and Techniques*, vol. 51, no. 4, pp. 1241 – 1246, Apr 2003.

[45] H. Ishida and K. Araki, "Design and analysis of uwb band pass filter with ring filter," in *Proc. IEEE MTT-S International Microwave Symposium Digest (IMS)*, vol. 3, Fort Worth, TX, USA, May 2004, pp. 1307 – 1310.

[46] J. Bonache, I. Gil, J. Garcia-Garcia, F. Martin, R. Marques, and M. Sorolla, "Band pass filters for ultra wideband systems," in *Proc. IEEE AP-S International Symposium*, vol. 2A, June 2005, pp. 639 – 642.

[47] C.-L. Hsu, F.-C. Hsu, and J. Kuo, "Microstrip bandpass filters for ultra-wideband (uwb) wireless communications," in *Proc. IEEE MTT-S International Microwave Symposium Digest (IMS)*, Long Beach, CA, USA, June 2005, pp. 679 – 682.

[48] L. Zhu, H. Bu, and K. Wu;, "Aperture compensation technique for innovative design of ultra-broadband microstrip bandpass filter," in *Proc. IEEE MTT-S International Microwave Symposium Digest (IMS)*, vol. 1, Boston, MA, USA, June 2000, pp. 315 – 318.

[49] G. Matthaei, E. M. T. Jones, and L. Young, *Microwave filters: impedance-matching networks, and coupling structures.* Norwood, MA: Artech House, 1980.

[50] M. Kang, C. Caloz, and T. Itoh, "Miniaturized mim crlh transmission line structure and application to backfire-to-endfire leaky-wave antenna," in *Proc. IEEE AP-S International Symposium and USNC/URSI National Radio Science Meeting*, vol. 1, Monterey, CA, USA, June 2004, pp. 827 – 830.

[51] K. C. Gupta, R. Garg, I. J. Bahl, and R. Bhartia, *Microstrip Lines and Slotlines*, 2nd ed. Norwood, MA: Artech House, 1996.

[52] R. Mongia, I. Bahl, P. Bhartia, and J. Hong, *RF and Microwave Coupled-Line Circuits*, 2nd ed. Norwood, MA: Artech House, 2007.

[53] C. A. Balanis, *Antenna Theory: Analysis and Design*, 3rd ed. New Jersey: Wiley, 2005.

[54] M. A. Antoniades and G. V. Eleftheriades, "A broadband series power divider using zero-degree metamaterial phase-shifting lines," *IEEE Microwave and Wireless Components Letters*, vol. 15, no. 11, pp. 808 – 810, November 2005.

[55] A. Lai, K. M. K. H. Leong, and T. Itoh, "A novel n-port series divider using infinite wavelength phenomena," in *Proc. IEEE MTT-S International Microwave Symposium Digest (IMS)*, Long Beach, CA, USA, June 2005, pp. 1001 – 1004.

[56] J. Pollak, M. Moisan, Z. Zakrzewski, J. Pelletier, Y. Arnal, A. Lacoste, and T. Lagarde, "Compact waveguide-based power divider feeding independently any number of coaxial lines," *IEEE Transactions on Microwave Theory and Techniques*, vol. 55, no. 5, pp. 951 – 957, May 2007.

[57] T. H. Lee, *The design of CMOS radio-frequency integrated circuits*, 2nd ed. Cambridge, United Kingdom: Cambridge University Press, 2004.

[58] N. Yang, C. Caloz, V.-H. Nguyen, and K. Wu, "Non-radiative crlh boxed stripline structure with high q performances," in *Proc. International Symposium on Electromagnetic Theory (EMTS)*, Ottawa, Canada, July 2007.

[59] R. Islam, F. Elek, and G. V. Eleftheriades, "Coupled-line metamaterial coupler having co-directional phase but contra-directional power flow," *Electronics Letters*, vol. 40, no. 5, pp. 315 – 317, Febuary 2004.

[60] R. Islam and G. V. Eleftheriades, "Printed high-directivity metamaterial ms/nri coupled-line coupler for signal monitoring applications," *IEEE Microwave and Wireless Components Letters*, vol. 16, no. 4, pp. 164 – 166, April 2006.

[61] B. M. Oliver, "Directional electromagnetic couplers," *Proceedings of the IRE*, vol. 42, no. 11, pp. 1686 – 1692, November 1954.

[62] B. M. Louisell, *Coupled Mode and Parametric Electronics*. New York: Wiley, 1960.

[63] M. K. Krage and G. I. Haddad, "Characteristics of coupled microstrip transmission lines-i: coupled-mode formulation of inhomogeneous lines," *IEEE Transactions on Microwave Theory and Techniques*, vol. 18, no. 4, pp. 217 – 222, January 1970.

[64] L. Young, *Parallel Coupled Lines and Directional Couplers*. Norwood, MA: Artech House, 1972.

[65] P. Gray, P. Hurst, S. Lewis, and R. G. Meyer, *Analysis and Design of Analog Integrated Circuits*, 4th ed. New York: Wiley, 2001.

[66] C. R. Paul, *Analysis of multiconductor transmission lines*, 2nd ed. New Jersey: J. Wiley, 2008.

[67] D. Wentzloff and A. Chandrakasan, "Delay-based bpsk for pulsed-uwb communication," in *Proc. IEEE International Conference on Acoustics, Speech and Signal Processing (ICASSP)*, vol. 3, March 2007, pp. 561 –564.

[68] L. W. Fullerton and I. A. Cowie, "Ultrawide-band communication system and method," U.S. Patent 5 677 927, October 14, 1997.

[69] M. Ghavami, L. B. Michael, and R. Kohno, *Ultra wideband Signals and Systems in Communication Engineering*. New Jersey: Wiley, 2007.

[70] S. Gupta, C. Caloz, and S. Abielmona, "Crlh leaky-wave real-time spectrum analyzer (rtsa) with unrestricted time-frequency resolution," in *Proc. IEEE MTT-S International Microwave Symposium Digest, (IMS)*, Atlanta, GA, USA, June 2008, pp. 807–810.

[71] J.-S. Gómez-Díaz, S. Gupta, A. Alvarez-Melcon, and C. Caloz, "Impulse-regime crlh resonator and its application to a tunable pulse rate multiplicator," *Radio Science*, vol. 44, pp. 1 – 9, July 2009.

[72] A. A. Oliner and D. R. Jackson, "Leaky-wave antenna," in *Antenna Engineering Handbook*, 4th ed., J. L. Volakis, Ed. McGraw-Hill, 2007, ch. 11.

[73] C. A. Allen, K. M. K. H. Leong, and T. Itoh, "2-d frequency-controlled beam-steering by a leaky/guided wave transmission line array," in *Proc. IEEE MTT-S International Microwave Symposium Digest (IMS)*, San Francisco, CA, USA, June 2006, pp. 457 – 460.

[74] A. Lai, K. M. Leong, and T. Itoh, "Leaky-wave steering in a two-dimensional metamaterial structure using wave interaction excitation," in *Proc. IEEE MTT-S International Microwave Symposium Digest (IMS)*, San Francisco, CA, USA, June 2006, pp. 1643 – 1646.

[75] T. Kaneda, A. Sanada, and H. Kubo, "2d beam scanning planar antenna array using composite right/left-handed leaky wave antennas," *IEICE Transaction on Electronics*, vol. E89, no. 12, pp. 1904 – 1911, December 2006.

[76] F. P. Casares-Miranda, C. C.-P. nalosa, and C. Caloz, "High-gain active composite right/left-handed leaky-wave antenna," *IEEE Transactions on Antenna and Propagation*, vol. 54, no. 8, pp. 2292 – 2300, August 2006.

[77] S. S., M. Ohashi, M.-K. Fujimoto, M. Fukushima, K. Waseda, S. Miyoki, N. Mavalvala, and H. Yamamoto, "High-gain power recycling of a fabry-perot michelson interferometer," *Applied Optics*, vol. 39, no. 25, pp. 4616 – 4620, September 2000.

[78] W. Fu, Y. Qian, and T. Itoh, "A ring-laser type quasi-optical oscillator using leaky-wave antenna," *Proc. IEEE 27th European Microwave Conference and Exhibition*, pp. 181 – 184, September 1997.

[79] C. Y. Pon, "Hybrid-ring directional coupler for arbitrary power divisions," *IRE Transactions on Microwave Theory and Techniques*, vol. 9, no. 6, pp. 529 – 535, November 1961.

[80] L. Liu, C. Caloz, and T. Itoh, "Dominant mode (dm) leaky-wave antenna with backfire-to-endfire scanning capability," *Electronics Letters*, vol. 38, no. 23, pp. 1414 – 1416, October 2002.

[81] S. Lim, C. Caloz, and T. Itoh, "Electronically-scanned composite right/left-handed microstrip leaky-wave antenna," *IEEE Microwave and Wireless Components Letters*, vol. 14, no. 6, pp. 277 – 279, June 2004.

[82] ——, "Metamaterial-based electronically controlled transmission line structure as a novel leaky-wave antenna with tunable angle and beamwidth," *IEEE Transactions on Microwave Theory and Techniques*, vol. 53, no. 1, pp. 161 – 173, January 2005.

[83] R. P. Owens, "Microstrip antenna feeds," in *Handbook of Microstrip Antennas*, J. R. James and P. S. Hall, Eds. Peter Peregrinus Ltd., 1989, vol. 2, ch. 14.

[84] S. March, "A wideband stripline hybrid ring (correspondence)," *Microwave Theory and Techniques, IEEE Transactions on*, vol. 16, no. 6, pp. 361–361, Jun 1968.

[85] C.-Y. Chang and C.-C. Yang, "A novel broad-band chebyshev-response rat-race ring coupler," *Microwave Theory and Techniques, IEEE Transactions on*, vol. 47, no. 4, pp. 455–462, Apr 1999.

[86] V.-H. Nguyen and C. Caloz, "Anisotropic backward-wave meta-susbtrate and its application to a microstrip leaky-wave antenna," in *Proc. CNC/USNC URSI National Radio Science Meeting*, Ottawa, ON, Canada, July 2007.

[87] R. Sigarusa, V.-H. Nguyen, C. Caloz, and S. Tedjini, "Efficient electronically scanned crlh leaky-wave antenna using independent double tuning for impedance

equalization," in *Proc. of CNC/USNC URSI National Radio Science Meeting*, San Diego, CA, USA, July 2008.

[88] S. Ramo, J. R. Whinnery, and T. V. Duzer, *Fields and Waves in Communication Electronics*, 3rd ed. New York: Wiley, 1994.

Appendix A

Amplitude Coefficients Derivation used in the Generalized Coupled-Mode Theory

By superposition, the coupled forward and backward waves propagating on line 1 are given from (3.28) as

$$a_1^+(z) = Ae^{-j\beta_I z} + Be^{-j\beta_{II} z} \tag{A.1a}$$

$$a_1^-(z) = Ce^{+j\beta_I z} + De^{+j\beta_{II} z} \tag{A.1b}$$

where $\beta_{I,II}$ are given by (1.7) and A, B, C and D are unknown amplitudes to be determined. The coupled forward and backward waves propagating on line 2 are obtained by substituting (A.1a) and (A.1b) into (3.26a) and (3.26b), which yields

$$a_2^+(z) = \frac{X \cdot K_{FW} + Y \cdot K_{BW}}{K_{BW}^2 - K_{FW}^2} \tag{A.2a}$$

$$a_2^-(z) = \frac{X \cdot K_{BW} + Y \cdot K_{FW}}{K_{BW}^2 - K_{FW}^2}, \text{where} \tag{A.2b}$$

$$X = Ae^{-j\beta_I z}(\beta_{CRLH1} - \beta_I) + Be^{-j\beta_{II} z}(\beta_{CRLH1} - \beta_{II}) \tag{A.2c}$$

$$Y = Ce^{+j\beta_I z}(\beta_{CRLH1} - \beta_I) + De^{+j\beta_{II} z}(\beta_{CRLH1} - \beta_{II}) \tag{A.2d}$$

The coefficients A, B, C and D can now be determined by applying the following boundary conditions at the ports of the coupled-line structure, which yields with reference to Fig. A.1

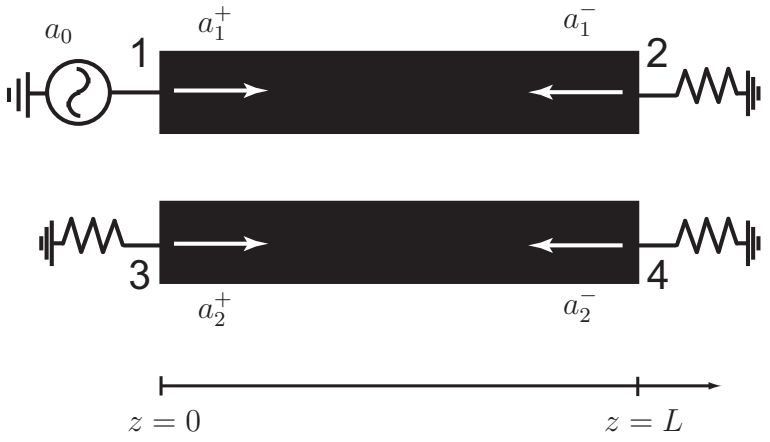

Figure A.1 Coupled-line structure description with appropriate source and terminations for the application of boundary condition in the CMT.

$$a_1^+(z=0) = A + B = a_0 \tag{A.3a}$$

$$a_1^-(z=L) = Ce^{+j\beta_I L} + De^{+j\beta_{II} L} = 0 \tag{A.3b}$$

$$a_2^+(z=0) = \left(\frac{X \cdot K_{FW} + Y \cdot K_{BW}}{K_{BW}^2 - K_{FW}^2}\right)_{z=0} \tag{A.3c}$$

$$a_2^-(z=L) = \left(\frac{X \cdot K_{BW} + Y \cdot K_{FW}}{K_{BW}^2 - K_{FW}^2}\right)_{z=L} \tag{A.3d}$$

This represents an algebraic system of four equations with four unknowns A, B, C, D. After lengthy but straightforward algebraic manipulations, these coefficients are

found to be

$$A = a_0 \frac{m\{[me^{j2\beta_I L} - ne^{j(\beta_I+\beta_{II})L}]K_{BW}^2 + (\beta_{II}-\beta_I)e^{j2(\beta_I+\beta_{II})L}K_{FW}^2\}}{[me^{j\beta_I L} - ne^{j\beta_{II}L}]^2 K_{BW}^2 - (\beta_{II}-\beta_I)^2 e^{j2(\beta_I+\beta_{II})L}K_{FW}^2} \quad \text{(A.4a)}$$

$$B = a_0 \frac{-n\{[me^{j(\beta_I+\beta_{II})L} - ne^{j2\beta_{II}L}]K_{BW}^2 + (\beta_{II}-\beta_I)e^{j2(\beta_I+\beta_{II})L}K_{FW}^2\}}{[me^{j\beta_I L} - ne^{j\beta_{II}L}]^2 K_{BW}^2 - (\beta_{II}-\beta_I)^2 e^{j2(\beta_I+\beta_{II})L}K_{FW}^2} \quad \text{(A.4b)}$$

$$C = \frac{nme^{j\beta_{II}L}(e^{j\beta_I L} - e^{j\beta_{II}}L)K_{FW}K_{BW}}{[me^{j\beta_I L} - ne^{j\beta_{II}L}]^2 K_{BW}^2 - (\beta_{II}-\beta_I)^2 e^{j2(\beta_I+\beta_{II})L}K_{FW}^2} \quad \text{(A.4c)}$$

$$D = \frac{-nme^{j\beta_I L}(e^{j\beta_I L} - e^{j\beta_{II}}L)K_{FW}K_{BW}}{[me^{j\beta_I L} - ne^{j\beta_{II}L}]^2 K_{BW}^2 - (\beta_{II}-\beta_I)^2 e^{j2(\beta_I+\beta_{II})L}K_{FW}^2} \quad \text{(A.4d)}$$

where

$$m = \beta_{CRLH1} - \beta_{II}$$

$$n = \beta_{CRLH1} - \beta_I$$

Appendix B

Amplitude Coefficients Derivation used in the Quasi-TEM Coupled-Mode Theory

By superposition, the coupled forward wave propagating on line 1 are given from (3.28) as

$$a_1^+(z) = Ae^{-j\beta_I z} + Be^{-j\beta_{II} z}, \tag{B.1}$$

where $\beta_{I,II}$ are given by (3.35) and A, B are unknown amplitudes to be determined. The coupled forward and backward waves propagating on line 2 are obtained by substituting (B.1) into (3.26a), which yields

$$a_2^-(z) = Ae^{-j\beta_I z}\frac{\beta_{CRLH1} - \beta_I}{K_{BW}} + Be^{-j\beta_{II} z}\frac{\beta_{CRLH1} - \beta_{II}}{K_{BW}}, \tag{B.2}$$

The coefficients A and B can now be determined by applying the following boundary conditions at the ports of the coupled-line structure, which yields with reference to Fig. B.1

$$a_1^+(z=0) = A + B = 0 \tag{B.3a}$$

$$a_2^-(z=L) = Ae^{-j\beta_I z}\frac{\beta_{CRLH1} - \beta_I}{K_{BW}} + Be^{-j\beta_{II} z}\frac{\beta_{CRLH1} - \beta_{II}}{K_{BW}} = 0. \tag{B.3b}$$

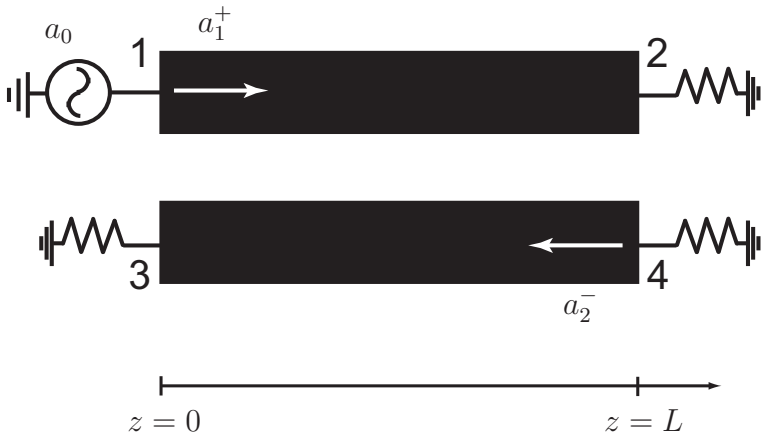

Figure B.1 Coupled-line structure description with appropriate source and terminations for the application of boundary condition in the quasi-TEM approximation.

This represents an algebraic system of two equations with two unknowns A, B. After some algebraic manipulations, these coefficients are found to be

$$A = B\frac{\beta_r + \beta_a}{\beta_r - \beta_a}e^{j2\beta_r L}, \tag{B.4a}$$

$$B = \frac{a_0}{1 + \frac{\beta_r+\beta_a}{\beta_r-\beta_a}e^{j2\beta_r L}}. \tag{B.4b}$$

Appendix C

Electromagnetic Coupling of Coupled-Line Couplers

C.1 Electric coupling and displacement current

In this section, a displacement current $\triangle i_2$ flowing from the excited TL (TL 1) to the coupled TL (TL 2) due to the electric coupling between two coupled TLs is derived as a function of the mutual coupling capacitor C_{12} and the input voltage v_1 on TL 1. The function is obtained by first applying the conservation of charge equation (Kirchhoff's current law) to an infinitesimal cube of size $\triangle z$ enclosing TL 1 as shown in Fig. C.1(a) and then using Ohm's law to an equivalent circuit model of two coupled TLs (only electric coupling being considered) as shown in Fig. C.1(b).

The conservation of charge equation which can be derived by applying the divergence to the Ampère's law and combining with Gauss's law [88], states that $\nabla \cdot \mathbf{J} = -\partial\rho/\partial t$. By applying a volume integration over the infinitesimal cube of size $\triangle z$ on both side of this equation, we obtain

$$\begin{aligned} \int_V (\nabla \cdot \mathbf{J})\, dV &= -\tfrac{\partial}{\partial t} \textstyle\int_V \triangle\rho dV \\ \oint_S \mathbf{J} \cdot d\mathbf{S} &= -\tfrac{\partial \triangle Q_1(t)}{\partial t}, \end{aligned} \tag{C.1}$$

where the divergence theorem has been applied to the left-hand-side of the last integral equation. Equation (C.1) is essentially the Kirchhoff's current law, which states that the total current (conduction and displacement) flowing out of a closed volume is zero. This can be seen from Fig. C.1 where the input conduction current density $J_{1,in}$ is parallel but in opposite direction with the normal vector d_{S1} of surface $S1$, whereas the output conduction current density $J_{2,in}$ is parallel and in the same direction with the normal vector d_{S2} of surface $S2$. The charge $\triangle Q_1$ inside the cube of size $\triangle z$ is

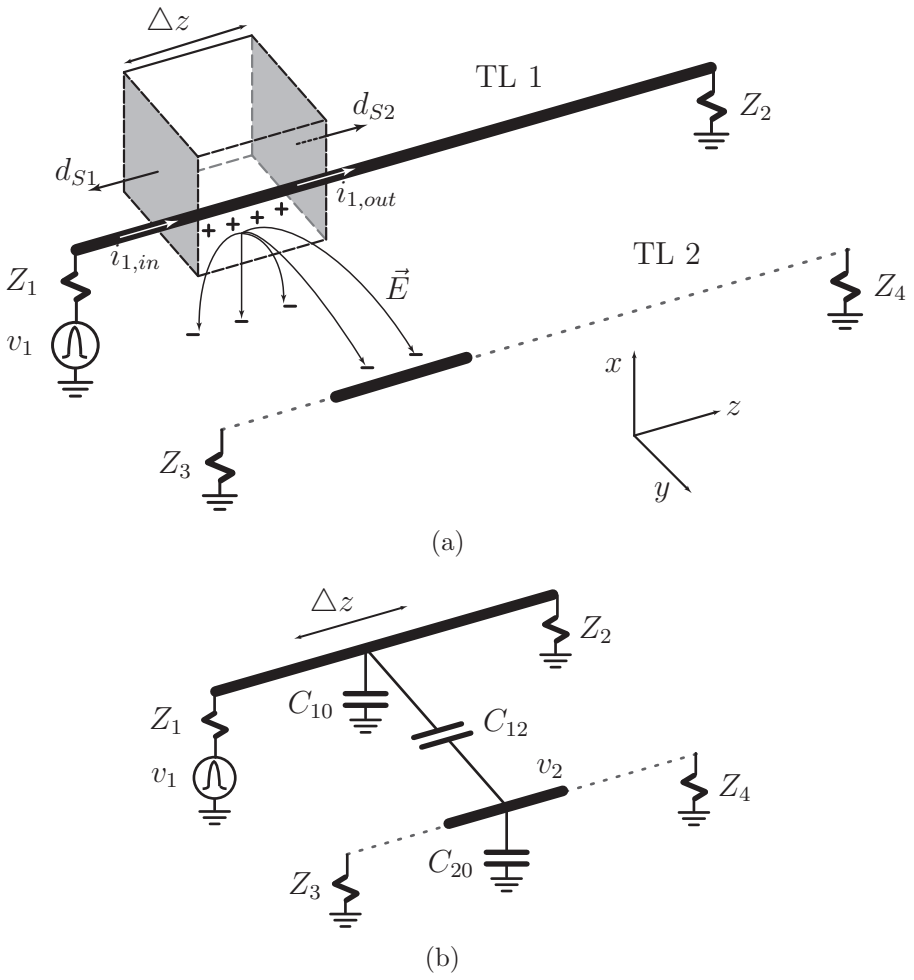

Figure C.1 Electric coupling of coupled-line couplers. (a) A coupled-line coupler with an input TL 1 and an infinitesimal $\triangle z$ coupled output TL 2 section. An infinitesimal cube of size $\triangle z$ enclosing TL1 is used in the electric coupling analysis. (b) An equivalent circuit model of the coupled-line coupler considering only electric coupling. Capacitors C_{10}, C_{20}, and C_{12} have per-unit-length values $[F/m]$ and model the self- and mutual capacitance of two TLs.

the sum of the self-charge on TL 1 and the coupled-charge between TL 1 and TL 2, i.e. $\triangle Q_1 = (C_{10}\triangle z)v_1 + (C_{12}\triangle z)(v_1 - v_2)$, where v_2 is the voltage on TL 2. Applying these relations into (C.1) gives

$$\begin{aligned} \oint_{S1} -\mathbf{J_{1,in}} dS1 + \oint_{S2} \mathbf{J_{2,out}} dS2 \quad &= -\tfrac{\partial[(C_{10}\triangle z)v_1 + (C_{12}\triangle z)(v_1 - v_2)]}{\partial t} \\ -i_{1,in} + i_{1,out} = -(\triangle i_{10} + \triangle i_{12}) \quad &= -(C_{10}\triangle z)\tfrac{\partial v_1}{\partial t} - (C_{12}\triangle z)\tfrac{\partial (v_1 - v_2)}{\partial t}, \end{aligned} \tag{C.2}$$

where the difference between output and input conduction currents on TL 1 is the sum of displacement currents $\triangle i_{10}$ and $\triangle i_{12}$ of per-unit-length capacitors C_{10} and C_{12}, respectively. The displacement current of interest $\triangle i_{12}$, which forms part of the current flowing on TL 2 is

$$\triangle i_2 = \triangle i_{12} = (C_{12}\triangle z)\frac{\partial (v_1 - v_2)}{\partial t}. \tag{C.3}$$

If we consider a harmonic regime operation $e^{j\omega t}$, (C.3) can be expressed as

$$\triangle \tilde{I}_2 = j\omega (C_{12}\triangle z)(\tilde{V}_1 - \tilde{V}_2), \tag{C.4}$$

where $\tilde{I}_2$, $\tilde{V}_1$, and $\tilde{V}_2$ are the phasors of current i_2 and voltages v_1 and v_2, respectively. Applying Ohm's law to the equivalent circuit of an infinitesimal section of a coupled-line coupler as shown in Fig. C.1(b), the voltage on TL 2 can be expressed as the function of the voltage on TL 1 and circuit parameters as

$$\tilde{V}_2 = \tilde{V}_1 \left(\frac{j\omega C_{12}\triangle z Z}{1 + j\omega C_{12}\triangle z Z} \right), \tag{C.5}$$

where

$$Z = \frac{R_{//}}{1 + j\omega C_{20}\triangle z R_{//}} \quad \text{and} \quad R_{//} = \frac{Z_3 Z_4}{Z_3 + Z_4}.$$

Substitute (C.5) into (C.4), we get

$$\triangle \tilde{I}_2 = j\omega (C_{12}\triangle z)\tilde{V}_1 \left[\frac{1 + j\omega C_{20}\triangle z R_{//}}{1 + j\omega (C_{12} + C_{20})\triangle z R_{//}} \right]. \tag{C.6}$$

At the operating frequency of coupled-line couplers, $R_{//}$ has a much lower impedance than the impedance of $(C_{12}+C_{20})\triangle z$ and hence (C.6) can be reduced to the following:

$$\triangle \tilde{I}_2 \approx j\omega (C_{12}\triangle z)\tilde{V}_1. \tag{C.7}$$

Equivalently, (C.7) can be written in time domain as

$$\triangle i_2 = (C_{12}\triangle z)\frac{dv_1}{dt}. \tag{C.8}$$

Equation (C.8) reveals that a change in voltage on TL 1 results in a current on TL 2 due to electric coupling between two coupled TLs. Hence, electric coupling through the capacitor C_{12} from TL 1 to TL 2 can be modelled as a current source in a shunt connection with TL 2 as shown in Fig. C.2.

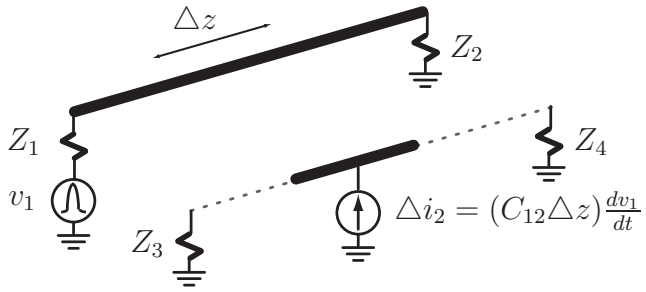

Figure C.2 An equivalent model of electric coupling in coupled-line couplers as a displacement current source in shunt with TL 2.

C.2 Magnetic coupling and electromotive force (emf) voltage

In this section, an electromotive force (emf) voltage $\triangle v_2$ arising on the coupled TL 2 due to the magnetic coupling between two coupled TLs is derived as a function of the mutual coupling inductor L_{12} and the excited current i_1 on TL 1. The function is obtained by applying the Faraday's law to the closed surface S_2 as shown in Fig. C.3(a) and then using the mutual inductance of equivalent circuit model of two coupled TLs (only magnetic coupling being considered) as shown in Fig. C.3(b).

The time-varying current i_1 of TL 1 creates a changing magnetic flux density $\vec{B_1}$ flowing thru a surface S_2 formed between an infinitesimal section $\triangle z$ of TL 2 and the ground plane. The resulting time-varying magnetic flux density produces a circulating electric field according to Faraday's law, which states that $\triangledown \times \mathbf{E} = -\partial\vec{B_1}/\partial t$. By applying a surface integration over the closed surface S_2 on both side of this equation,

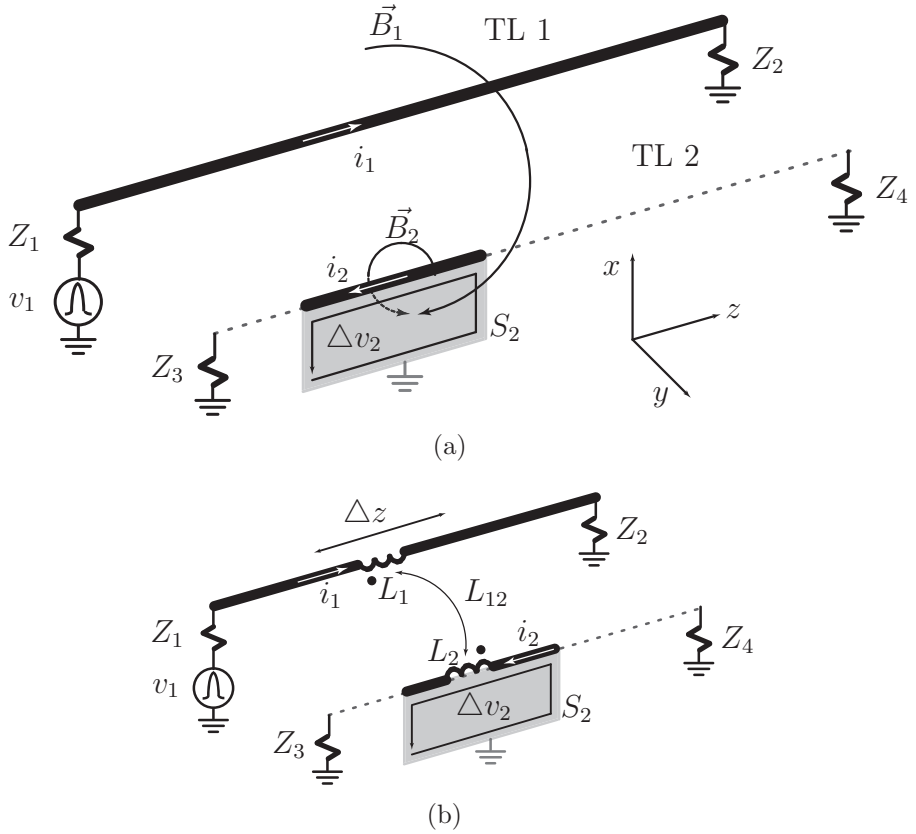

Figure C.3 Magnetic coupling of coupled-line couplers. (a) A coupled-line coupler with an input TL 1 and an infinitesimal $\triangle z$ coupled output TL 2 section. A surface S_2 between TL 2 and the ground plane is used in the magnetic coupling analysis. (b) An equivalent circuit model of the coupled-line coupler considering only magnetic coupling. Inductors L_1, L_2, and L_{12} have per-unit-length values $[H/m]$ and model the self- and mutual inductance of two TLs.

we obtain

$$\int_{S_2} (\nabla \times \mathbf{E}) \cdot \mathbf{dS_2} = \int_{S_2} \left(-\partial \vec{B}_1 / \partial t \right) \cdot \mathbf{dS_2},$$
$$\oint_{C2} \mathbf{E} \cdot \mathbf{dl} = \triangle v_2 = -\frac{\partial}{\partial t} \int_{S_2} \vec{B}_1 \cdot \mathbf{dS_2}, \tag{C.9}$$

where the Stoke's theorem has been applied to the left-handed-side of the last equation and C_2 is the closed boundary of the surface S_2. Equation C.9 is essentially Faraday's

law of induction and $\triangle v_2$ is the induced emf voltage.

The induced voltage in line 2 due to current flowing in line 1 is commonly known as the mutual inductance L_{12} between line 1 and line 2. This mutual inductance is defined as the ratio of the varying magnetic density $\vec{B_1}$ of current i_1 through the closed surface S_2 of TL 2 and the current i_1. For an infinitesimal $\triangle z$ section, the mutual inductance is written as

$$L_{12}\triangle z = -\frac{\int_{S2} \vec{B_1} \cdot \mathbf{dS_2}}{i_1}. \tag{C.10}$$

Substitute (C.10) into (C.9), we get

$$\triangle v_2 = \frac{\partial(L_{12}\triangle z i_1)}{\partial t} = (L_{12}\triangle z)\frac{di_1}{dt}. \tag{C.11}$$

Equation (C.11) reveals that a changes in current on TL 1 results in an emf voltage on TL 2 due to magnetic coupling between two coupled TLs. Hence, magnetic coupling through the inductor L_{12} from TL 1 to TL 2 can be modelled as a voltage source in series with TL 2 as shown in Fig. C.4.

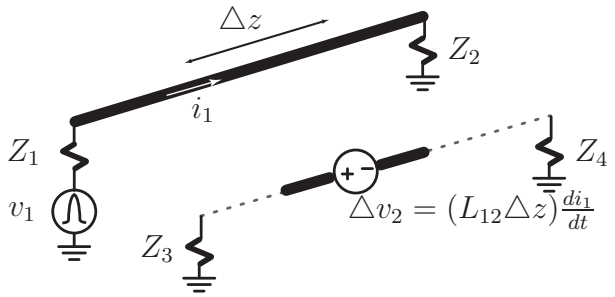

Figure C.4 An equivalent model of magnetic coupling in coupled-line couplers as an emf voltage source in series with TL 2.

Appendix D

List of Publications and Awards

D.1 Peer-reviewed journal publications

1^{st} author

1. H. V. Nguyen, A. Parsa and C. Caloz, "Power-recycling leaky-wave antenna for efficiency maximization," *IEEE Transactions on Microwave Theory and Techniques*, submitted for publication.
2. H. V. Nguyen, S. Abielmona and C. Caloz, "Highly efficient leaky-wave antenna array using a power recycling series feeding network," *IEEE Antennas and Wireless Propagation Letters*, vol. 8, pp. 441- 444, March 2009.
3. H. V. Nguyen and C. Caloz, "First- and second-order differentiators based on coupled-line directional couplers," *IEEE Microwave and Wireless Components Letters,* vol. 18, no. 12, pp. 791-793, December 2008.
4. H. V. Nguyen and C. Caloz, "CRLH delay line pulse position modulation transmitter," *IEEE Microwave and Wireless Components Letters,* vol. 18, no. 8, pp. 527-529, August 2008.
5. H. V. Nguyen and C. Caloz, "Tunable arbitrary N-port CRLH infinite-wavelength series power divider," *Electronic Letters*, vol. 43, no. 23, November 2007.
6. H. V. Nguyen and C. Caloz, "Generalized coupled-mode approach of metamaterial coupled-line couplers: coupling theory, phenomenological explanation and experimental demonstration," *IEEE Transactions on Microwave Theory and Techniques*, vol. 55, no. 5, pp.1029-1039, May 2007.
7. H. V. Nguyen and C. Caloz, "Dual-band CRLH Branch-line coupler in MIM technology," *IEEE Microwave and Optical Technology Letters*, vol. 48, no. 11, pp. 2331-2333, November 2006.
8. H. V. Nguyen and C. Caloz, "Broadband highly selective bandpass filter based on a Tapered Coupled-Resonator (TCR) CRLH structure," *Proceedings of the*

European Microwave Association, vol. 2, pp. 44-51, March 2006.

Others

1. C. Caloz, H. V. Nguyen, and T. Itoh, "Recent advances in metamaterial applications," *Proceedings of the IEEE* , Invited. In preparation.
2. S. Abielmona, H. V. Nguyen, and C. Caloz, "Direction of arrival estimation using an electronically-scanned CRLH leaky-wave antenna based on peak power detection," *IEEE Transactions on Antennas and Propagation*, submitted for publication.
3. R. Siragusa, H. V. Nguyen, P. Lemaître-Auger, S. Tedjini, and C. Caloz, "Modeling and synthesis of the interdigital/stub composite right/left-handed artificial transmission line," *Int. J. RF Microwave Computer-Aided Eng.*, vol. 19, no. 5, pp. 1 - 12, September 2009.
4. M. Coulombe, H. V. Nguyen, and C. Caloz, "Substrate integrated artificial dielectric (SIAD) structure for miniaturized microstrip circuits," *IEEE Antenna Wireless Propagation Letters*, vol. 6, pp. 575-579, December 2007.
5. S. Abielmona, H. V. Nguyen, C. Caloz, K. Wu and R. G. Bosisio, "Compact multilayer ultra-wideband Six-port device for modulation/demodulation," *IEE Electronics Letters*, vol. 43, no. 15, July 2007.
6. C. Caloz and H. V. Nguyen, "Novel broadband conventional- and dual-composite right/left-handed (C/D-CRLH) metamaterials: properties, implementation and double-band coupler application," *Journal of Applied Physics-A,* vol. 87, no. 2, pp. 309-316, May 2007.
7. C. Caloz, S. Abielmona, H. V. Nguyen, and A. Rennings, "Dual Composite Right/Left-Handed (D-CRLH) leaky-wave antenna with low beam squinting and tunable group velocity," *Journal of Physica Status Solidi (b)*, vol. 244, no. 4, pp. 1219 - 1226, April 2007.

D.2 Conference publications

1^{st} author

1. H. V. Nguyen, S. Abielmona, A. Parsa and C. Caloz, "Novel power recycling schemes for enhanced radiation efficiency in leaky-wave antennas," in *Proc. of IEEE Asia-Pacific Microwave Conference (APMC),* Singapore, December 2009.

2. H. V. Nguyen, S. Abielmona and C. Caloz, "Analog dispersive time delayer for beam-scanning phased array without beam-squinting," in *Proc. of IEEE AP-S International Symposium*, San Diego, CA, USA, July 2008.

3. H. V. Nguyen, N. Yang, and C. Caloz, "Differential bi-directional CRLH Leaky-wave antenna in CPS technology," in *Proc. of IEEE Asia-Pacific Microwave Conference (APMC)*, Bangkok, Thailand, December 2007.

4. H. V. Nguyen, S. Abielmona, A. Rennings, and C. Caloz, "Pencil-beam, 2D scanning leaky-wave antenna array," in *Proc. of International Symposium on Signals, Systems and Electronics (ISSSE)*, Montréal, QC, Canada, August 2007, pp. 139-142 (CD-ROM).

5. H. V. Nguyen and C. Caloz, "Anisotropic backward-wave meta-susbtrate and its application to a microstrip leaky-wave antenna," in *Proc. of CNC/USNC URSI National Radio Science Meeting*, Ottawa, ON, Canada, July 2007.

6. H. V. Nguyen, J. Gauthier, J. M. Fernandez, M. Sierra-Castaner, and C. Caloz, "Metallic wire substrate (MWS) for miniaturization in planar microwave applications," in *Proc. of IEEE Asia-Pacific Microwave Conference (APMC)*, Yokohama, Japan, December 2006.

7. H. V. Nguyen and C. Caloz, "Dual-band CRLH six-port front-end in MIM technology," in *Proc. of IEEE 36th European Microwave Conference (EuMC)*, Manchester, UK, September 2006, pp. 122-124.

8. H. V. Nguyen and C. Caloz, "Simple-design and compact MIM CRLH microstrip 3-dB coupled-Line coupler," in *Proc. IEEE MTT-S International Microwave Symposium Digest (IMS)*, San Francisco, CA, USA, June 2006, pp. 1733-1736.

9. H. V. Nguyen and C. Caloz, "Metamaterial-based dual-band six-port front-end for direct digital QPSK transceiver," in *Proc. of the 13th IEEE Mediterranean Electrotechnical Conference (MELECON)*. Málaga, Spain, May 2006, pp. 363-366.

Others

1. S. Gupta, H. V. Nguyen, T. Kodera, S. Abielmona, and C. Caloz, "CRLH leaky-wave antenna based frequency division diplexing transceiver," in *Proc. of IEEE Asia-Pacific Microwave Conference (APMC)*, Singapore, December 2009.

2. R. Sigarusa, H. V. Nguyen, E. Perret, P. Lemaître-Auger, S. Tedjini, and C. Caloz, "Automated design of CRLH structures using co-design synthesis computational approach," in *Proc. of IEEE Asia-Pacific Microwave Conference (APMC)*, Singapore, December 2009.

3. R. Sigarusa, H. V. Nguyen, E. Perret, P. Lemaître-Auger, S. Tedjini, and C. Caloz, "Méthode de conception automatisée appliquée aux lignes composites main gauche/droite," in *Proc. of 16èmes Journées Nationales Micro-ondes*, Grenoble, France, 27-29 May 2009.

4. S. Abielmona, H. V. Nguyen, and C. Caloz, "Direction of arrival estimation using an electronically-scanned CRLH leaky-wave antenna," in *Proc. of CNC/USNC URSI National Radio Science Meeting*, North Charleston, SC, USA, June 2009.

5. R. Sigarusa, H. V. Nguyen, C. Caloz, and S. Tedjini, "Efficient electronically scanned CRLH leaky-wave antenna using independent double tuning for impedance equalization," in *Proc. of CNC/USNC URSI National Radio Science Meeting*, San Diego, CA, USA, July 2008.

6. N. Yang, C. Caloz, H. V. Nguyen, S. Abielmona, and K. Wu, "Non-radiative CRLH boxed stripline structure with high Q performances," in *Proc. of International Symposium on Electromagnetic Theory (EMTS)*, Ottawa, ON, Canada, July 2007.

7. S. Abielmona, H. V. Nguyen, F. Casares-Miranda, C. Camacho-Peñalosa, and C. Caloz, "Real-time digital beam-forming active leaky-wave antenna," in *Proc. IEEE AP-S International Symposium*, Honolulu, HI, USA, June 2007, pp. 5593-5596.

8. W. Tong, H. V. Nguyen, Z. Hu, and C. Caloz, "Dual composite right/left-handed (D-CRLH) transmission line in GaAs MMIC technology," in *Proc. of IEEE International Workshop on Antenna Technology (IWAT)*, Cambridge, UK, March 2007, pp. 105-108.

9. C. Caloz, H. V. Nguyen, and Y. Zhang, "Novel metamaterial coupled-line couplers: theory and implementations," in *Proc. of Progress in Electromagnetics Research Symposium (PIERS)*, Beijing, China, March 2007.

10. S. Abielmona, H. V. Nguyen and C. Caloz, "CRLH zeroth order resonator (ZOR): Experimental demonstration of insensitivity to losses and to size," in

Proc. of IEEE Asia-Pacific Microwave Conference (APMC), Yokohama, Japan, December 2006.

11. F. P. Casares-Miranda, A. Piche, H. V. Nguyen, C. Camacho Peñalosa, and C. Caloz, "Antenas leaky-wave activas basadas en metamateriales composite right/left-handed," in *Proc. of XXI Simposium Nacional de la URSI*, Oviedo, Spain, September 2006.
12. C. Caloz, H. V. Nguyen, and A. Sanada, "Novel ultra wideband (UWB) metamaterial (MTM) passive components," in *Proc. of Progress in Electromagnetics Research Symposium (PIERS)*, Tokyo, Japan, August 2006, pp. 26.
13. J.-F. Jobin Lepine, H. V. Nguyen, and C. Caloz, "Superluminal group velocity in CRLH transmission line metamaterials," in *Proc. of Canadian ANTEM/URSI*, Montréal, Canada, July 2006, pp. 377-379.

D.3 Patents

1. CALOZ, Christophe; NGUYEN Van-Hoang, GUPTA Shulabh, and ABIELMONA Samer, "Tunable delay system and corresponding method," Pub. No.: WO/2008/116289, International Application No.: PCT/CA2008/000516, Publication Date: 02.10.2008, International Filing Date: 18.03.2008.
2. FRIGON Jean-Francois; CALOZ Christophe; ABIELMONA Samer, and NGUYEN Van-Hoang, "System and method for power angular spectrum parameters estimation in a wireless communication system using antennas with reconfigurable radiation patterns," DIV-342 VAL-607

D.4 Trade-show

1. H. V. Nguyen, S. Abielmona, C. Caloz, J-F. Frigon, T. Martinuzzo, and D. Leconte, "Metamaterials smart antenna MIMO system for wireless local area networks," presented at *The World Best Technologies Showcase*, Arlington, TX, USA, March 25-27, 2008.

D.5 Awards

1. **Honorable Mention** award for the paper presented at the *IEEE AP-S International Symposium*, San Diego, CA, USA, July 2008.
2. **The Canadian URSI Young Scientist** award for the best paper presented at the *URSI International Symposium on Signals, Systems, and Electronics (ISSSE)*, Montréal, QC, Canada, August 2007.
3. **Outstanding Achievement** award from the MTT-S High Power Microwave Components Committee at the *IEEE International Microwave Symposium (IMS)*, San Francisco, CA, USA, June 2006.